University of Aarhus
Faculty of Science

Experiments with Cold Trapped Molecular Ions

(PhD thesis)

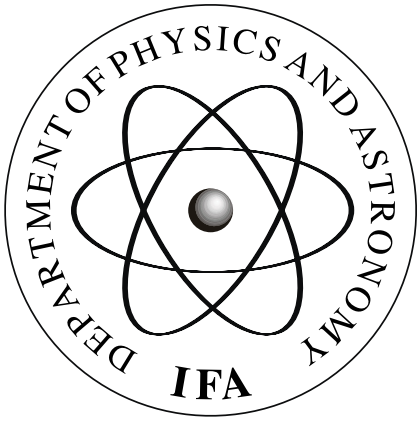

Author: Klaus Højbjerre
Supervisor: Prof. Michael Drewsen
Aarhus, September 2009

This thesis is submitted to the Faculty of Science at the University of Aarhus, Denmark, in order to fulfill the requirements for obtaining the PhD degree in Physics.
The studies have been carried out under the supervision of Professor Michael Drewsen in the Ion Trap Group at the Department of Physics and Astronomy, University of Aarhus, from January 2006 to August 2009.

Klaus Højbjerre
Experiments with Cold Trapped Molecular Ions
University of Aarhus, 2009

Electronically available at `http://www.phys.au.dk/iontrap`.

This thesis is typeset in Palatino, 10 pt, with ConTEXt

Acknowledgements

First and foremost I would like thank my supervisor Prof. Michael Drewsen for guiding me in my 4 year long journey into the interesting world of cold molecular physics. It has been hard work at times, but the results have always been in proportion with the effort, mainly because of the realistic and well-planned goals. When we handed in my PhD application to the faculty, I did definitely not expect that every single research goal would be reached, and to top it off, reached according to the timeline! But I am very happy to once again print this small list of objectives, now with checkmarks instead of bullets:

✓ Experiments with aniline.
✓ Experiments with Mg^+ and hydrogen gasses.
✓ Rotational cooling of MgH^+ ions.

However, even with good guidance and realistic goals, I would never have reached these results without the help from my colleagues in the laboratory, especially my faithful post-docs Anders Mortensen and Peter F. Staanum, as well as my fellow students, Anders K. Hansen and Peter Skyt. I dare not count how many night hours we have spent together in the laboratory, but they have been very much enlightened by the great spirits of these guys. I have also benefited greatly from the visits from David Offenberg and Roland Wester.

I would also like to express my gratitude to the rest of the people in the Ion Trap Group for making the office and the laboratory hours more pleasurable. It is, however, with mixed feelings that I at the same time resign from my appointment as Coffee Boss par Excellence in our office. It has been a pleasure to serve you, but I also feel relieved from a big responsibility. May the Krups ProAroma continue to serve you well.

Writing a thesis in approximately two months, while simultaneously working on the latest and greatest experiments in the laboratory, surely introduce quite a few typos, errors and inconsistencies to the text. Luckily, many of these are now corrected thanks to the last-minute proofreading by Joan Marler and Anne I. S. Holm. Your hard work is greatly appreciated, not only by me, but surely also by the dear readers of this thesis. Any remaining errors are certainly due to my last-second corrections.

Finally, I would like to thank my family and friends. Not only have they been very supportive, but also very tolerant with me, when the lab work took my time and energy, and the cell phone was blocked for days and weeks.

List of publications

I. K. Højbjerre, P. Staanum, D. Offenberg, J. L. Sørensen, A. Mortensen and M. Drewsen, *Experiments with single cold molecular ions*, Non-Neutral Plasma Physics Conference VI, AIP Conference Proceedings **862**, pp. 299-304 (2006)

II. K. Højbjerre, D. Offenberg, C. Z. Bisgaard, H. Stapelfeldt, P. Staanum, A. Mortensen and M. Drewsen, *Consecutive photodissociation of a single complex molecular ion*, Physical Review A **77**, 030702(R) (2008)

III. P. F. Staanum, K. Højbjerre, R. Wester and M. Drewsen, *Probing isotope effects in chemical reactions using single ions*, Physical Review Letters **100**, 243003 (2008)

IV. K. Højbjerre, A. K. Hansen, P. S. Skyt, P. F. Staanum and M. Drewsen, *Rotational state resolved photodissociation spectroscopy of translationally and vibrationally cold MgH+ ions: toward rotational cooling of molecular ions*, New Journal of Physics **11**, 055026 (2009)

V. P. F. Staanum, K. Højbjerre, and M. Drewsen *Chapter 10: Sympathetically-Cooled Single Ion Mass Spectrometry* to appear in Practical Aspects of Trapped Ion Mass Spectrometry, Vol. V: Applications of Ion Trapping Devices CRC Press, Taylor & Francis Group, New York (2009)

VI. P. F. Staanum, K. Højbjerre, P. S. Skyt, A. K. Hansen and M. Drewsen, *Rotational laser cooling of vibrationally and translationally cold molecular ions*, Submitted for publication

Contents

Chapter 1

Introduction

Doppler laser cooling of atomic neutral and ionic species has during the last two decades opened a wealth of new research areas and enabled extremely detailed investigations of atomic physics phenomena. The obvious next step is to cool molecules to open up both similar and completely new areas within molecular physics and chemistry. In fact, the detailed control and active manipulation of the internal as well as external degrees of freedom of molecules would be of great value for the advance of several research fields. Most fundamentally, unprecedented high precision spectroscopic data can be obtained for comparison with quantum chemistry models, for accurate measurements of natural constants and for metrology purposes [1, 2, 3, 4]. Advances in the control and manipulation of molecules may as well open new quantum information processing implementations [5]. In chemistry, state-prepared molecular targets can also lead to refined reaction studies, which includes unimolecular reactions with coherent light fields [6, 7] or quantum-state selected bimolecular reactions [8, 9]. Finally, the option of having a dense ensemble of identically prepared molecules enables the realization of new collective phenomena, such as Bose-Einstein condensation of molecules [10, 11].

However, as opposed to atoms, the lack of closed transitions in most molecules generally prevents the application of Doppler laser cooling, even though some schemes exist [12, 13]. Instead, many new approaches to prepare cold neutral or ionic molecules have been developed in the past decade. For neutrals the advances have, in particular, been relying on developments within the following approaches: Photoassociation of laser-cooled atoms [14, 15, 16, 17, 18], buffer-gas cooling of molecules held in magnetic traps [19], deceleration [20], filtering [21] and trapping [22, 23, 24, 25] of molecules by electrostatic fields, Feshbach resonance generated molecules in degenerate quantum gasses [10, 11], and deceleration of molecules by intense laser pulses [26]. Most recently, molecules produced by Feshbach resonances have been brought to the vibrational ground state of electronic molecular potentials by the additional use of stimulated Raman adiabatic passage schemes [27, 28, 29, 30]. Also recently, photoassociated molecules have been formed directly in the rovibrational ground state [31] or transferred to the vibrational ground state through shaped fs-laser pulses [18].

For molecular ions, several techniques have also been developed and refined. The technique of He buffer gas ion cooling [32] has been extended to molecular anions [33], and cryogenic cooling together with efficient shielding of the entire ion trap has brought molecular ions to temperatures below 10 K [32, 34]. Much progress has been achieved with molecular ions which are sympathetically cooled

into Coulomb crystals through the Coulomb interaction with laser-cooled atomic ions [35, 36, 37, 38, 39, 40, 41]. Most recently, the combination of cold neutral and ionic molecular techniques has made progress in studying cold reactions [42, 43].

Trapped molecular ions offer some very attractive features. Most obviously, the long storage time ease the experimental complications in many types of experiments and enable studies with very long observation times. Secondly, because experiments typically takes place under Ultra High Vacuum (UHV) conditions, internal coherences of the molecular ion is not destroyed by collisions. Additionally, the crystallization of the molecular ions also preserves the coherence, since the long inter-ion distances prevents efficient coupling of the internal degrees of freedom. Furthermore, it is possible to work with just a single molecular ion localized within ≈ 1 μm at a time. Localization and long storage times make trapped molecular ions ideal for experiments with focused laser beams, since the position uncertainty is easily within the waist of the laser beam. At the same time, a single molecular ion is in many cases the ideal target, as ensemble averaging is avoided, especially if some kind of quantum state preparation is applied, e.g. laser cooling of the internal degrees of freedom [44, 45], state preparation by projection measurements [46] or production of the ion in a specific rovibrational state through REMPI [47].

This work pushes forward the work of cold trapped molecular ions on two fronts. First we work with a single molecular ion and investigate non-destructive techniques for high precision identification of single molecular ions, which enables consecutive measurements to be done on the *same* ion. This technique allows for unprecedented tracking of reaction processes. On the other hand we demonstrate new techniques for even greater cooling of ensembles of ions. As opposed to other techniques, the scheme discussed is relatively simple to implement and additionally leaves the rotationally cooled ion well localized for use for further experimentation. The possibility of applying the rotational cooling technique to a single ion is promising for future more fundamental studies.

The layout of the thesis is as follows: In **chapter 2** the general experimental setup is described. That is, a brief tour of the vacuum chamber, a short description of the linear Paul trap, the 1+1 Resonance-Enhanced Multi Photon Ionization (REMPI) scheme for ion loading, the Doppler laser cooling scheme and the imaging system. The ion identification technique, which we have named Sympathetically Cooled Single Ion Mass Spectrometry (SCSI-MS), will be presented and carefully analyzed in **chapter 3**. It is based on the resonant excitation of a motional mode of two-ion crystals in the harmonic trapping potential. **Chapter 4** applies this technique to the study of photofragmentations of aniline ($C_6H_5NH_2^+$). This

demonstrates how one can work with even relatively complex ions, and that it is feasible to study consecutive reactions with a single ion and in this way gain information on individual photofragmentation pathways. In particular we observed the following 3-step photo-dissociation process with a single ion: $C_6H_5NH_2^+ \rightarrow C_5H_6^+ \rightarrow C_5H_5^+ \rightarrow C_3H_3^+$ using this technique again. Measurement of the branching ratio in the reaction $Mg^+ + HD \rightarrow MgH^+ (MgD^+) + D (H)$ is presented in **chapter 5**. This experiment illustrates another strength of working with a single ion at a time; the pure target and high detection efficiency means that only a few hundred measurements are enough to claim a branching ratio of more than 5 in favor of MgD^+ formation over MgH^+ formation. In **chapter 6** the focus is shifted to many ion Coulomb crystals. A 15-fold increase of the rotational ground state population of MgH^+ ions is achieved with the application of just a single laser. Finally, **chapter 7** is devoted to a brief summary.

Chapter 2

Equipment and Methods

The aim of this chapter is to give a brief introduction to the basic experimental equipment and methods utilized throughout the rest of this thesis. Since most of the setup was built prior to this work, detailed descriptions are omitted, but can be found in the references.

In short, our setup consist of a linear Paul trap (**section 2.2**) mounted inside a vacuum chamber (**section 2.1**). The trap is loaded with either Mg^+ or Ca^+ ions by crossing a skimmed atomic beam with a photoionizing laser beam at the center of the trap (**section 2.3**). The trapped ions are then Doppler laser cooled to a few mK (**section 2.4**), where they crystallize and form a Coulomb crystal. The fluorescent light from the laser cooled atomic ions are imaged onto an camera system consisting of an image intensifier and a CCD camera (**section 2.5**). Examples of recorded images can be seen in for example **figure 3.3** and **figure 6.7**. Finally, in **section 2.6** we give a very short introduction to trapped and sympathetically cooled molecular ions.

2.1 Vacuum chamber and attachments

Figure 2.1 shows a picture of the vacuum chamber seen from the outside. A typical base pressure of 4×10^{-10} mbar is maintained by a titanium sublimation pump and a Laybold IZ 270 triode ion getter pump located beneath the chamber table. The chamber pressure is monitored with a AML UHV Bayard-Alpert ion gauge or, alternatively, with a PC controlled Spectra Satellite LM502 rest gas analyzer with a mass range from 1 to 100 u and a resolution of 1 u. Gas can be leaked into the chamber via a leak valve located beneath the table. Together with the ion gauge, the leak valve allows us to control the pressure of the leaked-in gas with a precision better than 1×10^{-10} mbar. Two small gas containers with attached Pirani gauges in front of the leak valve are used as temporary reservoirs for gas and also enable us to prepare rough mixtures of gasses.

On one of the flanges a liquid nitrogen container, which allows us to cool down part of the chamber, is mounted. This improves the base pressure of the chamber further, as observed in the rotational cooling experiments described in **chapter 6**, but the pressure change is not measurable with the ion gauge.

The inside of the vacuum chamber can be seen in **figure 2.2** and most of the internal equipment will be described in the following sections .

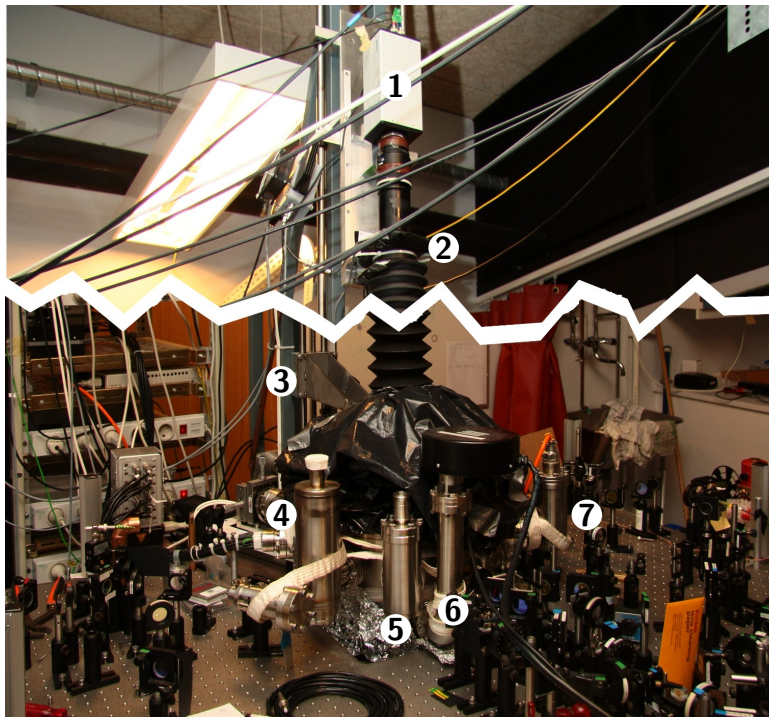

Figure 2.1 Picture of the vacuum chamber as seen from the outside. Seen in this picture is the (1) CCD camera to monitor the fluorescence from the laser-cooled ions via a (3) lenssystem and an (2) image-intensifier through a window in a top-flange of the vacuum chamber. The distance between the lens system and the image-intensifier is $\approx$ 1.5 m. Also seen is (4) a liquid nitrogen container, (5) the electron gun, (6) the rest-gas analyzer and (7) the ion gauge. Beneath the table is a leak valve controlled inlet for the admission of various gasses into the ion-trap region.

2.2 The linear Paul trap

The type of ion trap used in the experiments discussed in this thesis is a so-called linear RF (Paul) ion trap [48, 49]. A schematic diagram of this ion trap is shown in **figure 2.3** and a photograph of the ion trap is shown in **figure 2.4**. Like standard quadrupole mass filters, the ion trap consists of four electrodes with an RF voltage of the same phase applied to diagonally-opposed electrodes, but with a phase difference of 180° between the two sets of opposite electrodes. This arrangement leads to a near-ideal two-dimensional quadrupole field in the plane perpendicular to the direction defined by the electrodes (that is, the z-direction).

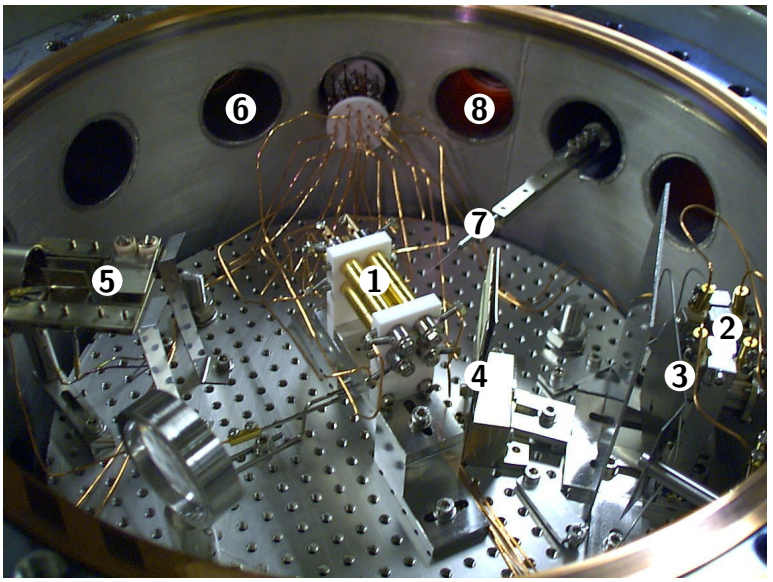

Figure 2.2 Picture of the linear RF ion trap inside the cylindrical vacuum chamber used in the experiments. The inner diameter of the chamber is 30 cm. Essential components inside the chamber are marked by numbers. (1) The linear RF ion trap. (2) The magnesium and calcium ovens, which are the sources for the atomic beams passing through the center of the ion trap. (3) Oven shutter. (4) Skimmer plates, used to collimate the effusive beams from the ovens in order to avoid contamination of the ion-trap electrodes. (5) Electron gun including deflection plates installed to make an electron beam cross the atomic beams in the center of the ion trap for ion production. (6) One of two sets of oppositely-positioned window openings for sending in laser beams for laser cooling of the ions along the main ion-trap axis (the z-axis) and along an axis perpendicular to the z-axis. (7) A piece of optical fiber with a diameter of 125 μm, which can be translated into the ion-trap center for calibration of the magnification of the lens system used to image the fluorescence of the laser-cooled ions. (8) One of two opposed window openings that permit a laser beam to cross the atomic beams nearly at right angles in the ion-trap center for producing ions by photoionization.

To achieve axial confinement, each electrode is divided into three parts and a positive DC voltage, U, is applied to the eight end-cap electrodes. The DC voltage, however, leads to a radial defocusing force, but by appropriate choices of U, the RF peak-to-peak voltage, V, and the RF frequency, Ω, both axial and radial confinement can be obtained simultaneously for the given ion-trap dimensions [50, 51]. In the following subsection a brief quantitative description is given, but for an in-depth discussion of ion traps, the reader is directed to other resources, for example Ref. [51].

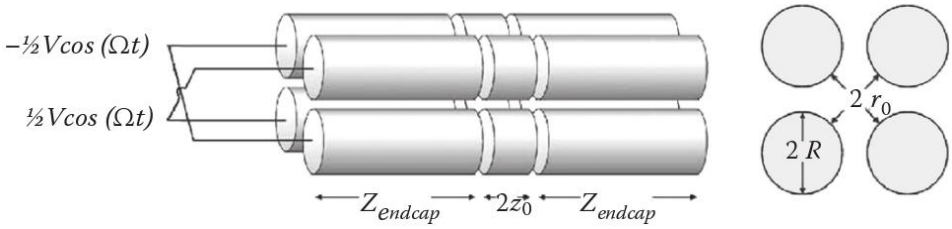

Figure 2.3 Sketch of a linear Paul trap. The trap consists of four parallel rods, each subdivided into three pieces. Particles are trapped radially by an oscillating E-field applied in phase on diagonally opposite rods and out of phase to nearest-neighbour rods. Along the trap axis, z, particles are confined by a static potential applied to the eight end pieces of the rods.

2.2.1 Theory of the linear Paul trap

The potential along the z-axis is given by

$$\Phi_z(z) = \eta U \frac{z^2}{z_0^2}, \tag{2.1}$$

where η is a geometrical constant defined by the electrode configuration, U is the static potential applied to the eight end caps and $2z_0$ is the length of the center piece as defined in **figure 2.3**. While this DC voltage leads to static confinement along the z-axis, it gives rise to a defocusing force in the radial plane, as required by Laplace's law ($\nabla^2\Phi = 0$). The potential in the radial plane is thus made up of contributions from both the static DC potential and the RF potential:

$$\Phi_{x,y}(x, y, t) = -\frac{\eta U}{2}\frac{x^2 + y^2}{z_0^2} - \frac{V}{2}\frac{x^2 - y^2}{r_0^2}\cos(\Omega t). \tag{2.2}$$

Here V is the peak-to-peak amplitude of the RF voltage, Ω is the RF-frequency and $2r_0$ is the distance between two diagonal rods (see **figure 2.3**).

From **equation (2.1)**, it is clear that the motion of a single particle along the z-axis is that of a single harmonic oscillator. The case of two particles will be treated in **chapter 3**, while the many ion case is discussed in for example Ref. [52].

Motion in the radial plane is somewhat more complicated. The equation of motion of a single particle is given by:

$$\frac{\partial^2 u}{d\tau^2} + [a_r - 2q_u\cos(2\tau)]u = 0, \qquad u = x, y, \tag{2.3}$$

where we have introduced the dimensionless parameters

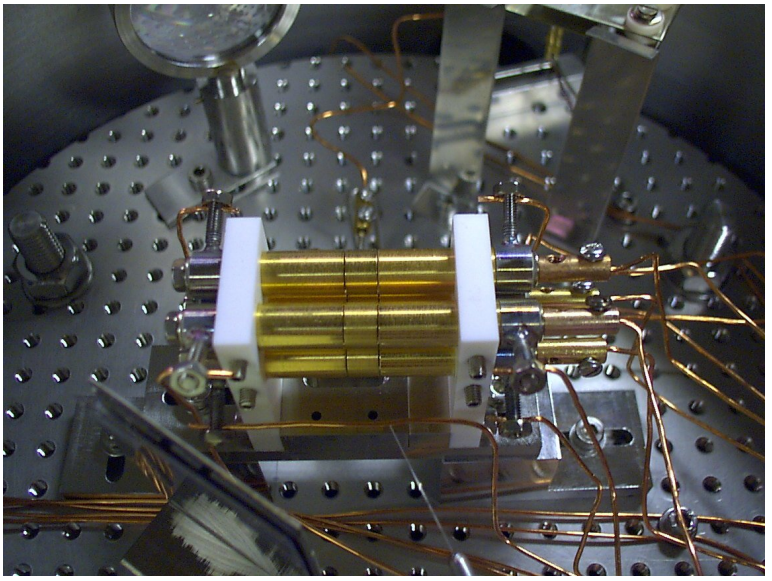

Figure 2.4 Picture of the actual ion trap used. As a scale, the center part of the electrode structure ($2z_0$) is 5.4 mmlong.

$$\tau = \frac{\Omega t}{2}, \qquad a_r = -4\frac{ne\eta U}{m\Omega^2 z_0^2}, \qquad q_x = -q_y = 2\frac{neV}{m\Omega^2 r_0^2} \tag{2.4}$$

Here m is the mass of the ion and n is the number of elementary charges, e, on the ion. **Equation 2.3** can be recognized as the so-called Mathieu equations [53, 51]. For stable single-ion trajectories to exist, the parameters a_r and q_r have to lie within certain stability regions [50]. In general, this motion is complex, but when $q_r < 0.4$, a single ion not too far from the trap center will experience an effective harmonic potential,

$$\phi(z, r) = m(\omega_z^2 z^2 + \omega_r^2 r^2) \tag{2.5}$$

where ω_z and ω_r are the oscillatory frequencies along the z-axis and in the radial plane, respectively. They are given by

$$\omega_z = \sqrt{\frac{2ne\eta Ui}{mz_0^2}} \tag{2.6}$$

$$\omega_r = \frac{1}{2}\Omega\sqrt{\frac{q_r^2}{2} + a_r} = \sqrt{\frac{n^2e^2V^2}{2m^2\Omega^2 r_0^4} - \frac{ne\eta U}{mz_0^2}} \tag{2.7}$$

From **equation (2.5)** through (**2.7**), it is seen that that the radial potential depends on the mass of the trapped particle, while the axial potential is independent thereof. This results in a radial separation of ions with different mass, a feature we will utilize in **chapter 6** when we estimate the number of trapped ions.

To arrive at **equation (2.5)**, a fast oscillating force at the RF frequency, which will induce radial ion motion, was neglected. It can, however, be shown that the amplitude of this fast *micromotion* will be much smaller than the distance of the ion to the z-axis, when $q_r < 0.4$ [54]. In the experiments to be presented in **chapter 3**, **4** and **5**, two ions are aligned on the z-axis and the rapid micromotion can hence be neglected. In **chapter 6**, we work with larger Coulomb crystals (see **figure 6.7**), but the micromotion is still limited and does not influence our experiment.

2.2.2 Our realization of a Paul trap

A picture of our ion trap can be seen in **figure 2.4**. The dimensions of the trap are chosen such that we achieve a nearly perfect radial quadrupole RF field [55] and a near-harmonic DC field over a few millimeters. The parameters are as follows: $r_0 = 3.50$ mm, $z_0 = 2.70$ mm, $z_{\text{endcap}} = 20.00$ mm, and $R = 4.00$ mm. Numerical simulations show that these choices of ion-trap dimensions result in $\eta = 0.248$. The peak-to-peak amplitude, V, of the RF field is typically of a few hundred volts and is coupled resonantly with the ion-trap electrodes at a radial frequency $\Omega = 2\pi \times 3.88$ MHz. Together with a typical DC voltage of about 1 V, a potential well with a depth of ≈ 1 eV is created (see **equation (2.5)**). Since this energy is many orders of magnitude higher than the thermal energy of the cooled ions and the thermal energy of the background gas, the storage time of the ions can be hours or more at a typical vacuum of $\approx 10^{-10}$ mbar.

2.3 Loading of atomic ions

To create atomic ions inside the trap, a skimmed atomic beam originating from an effusive oven is crossed with a photoionizing laser beam at the center of the ion trap. The photoionization technique is a resonance-enhanced two photon process, which is advantageous compared to the more usual electron impact ionization technique; Not only is it element selective, but also isotope selective [56, 57]. Furthermore, this can be carried out using low laser powers and low atomic beam fluxes because of the efficiency of the process. Therefore, the ovens can be operated at a relatively low temperature and the pressure in the vacuum chamber

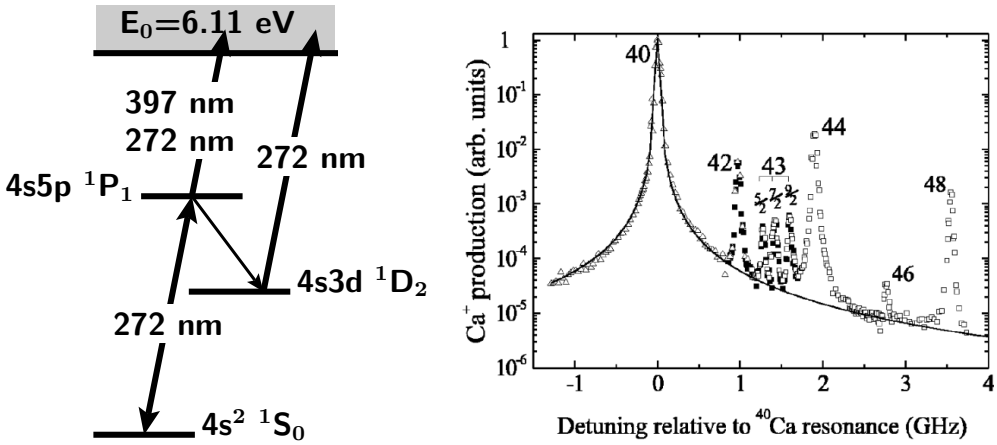

Figure 2.5 (a) Reduced energy level diagram for $^{40}Ca^{+}$ with ionisation relevant levels. An absorption of a 272 nm photon excites the atom to the $4p5p\,^1P_1$ state from which it can either decay back to the ground state, decay to $4s3d\,^1D_0$ metastable state or ionise through absorption of another photon. Likewise, an absorption of a 272 nm photon from the $4s3d\,^1D_0$ state leads to ionisation. (b) Photo ionisation spectrum for Ca^{+} as a function of ionisation laser frequency demonstrating the ability to load only the isototpe of interest [57].

rise less than 10^{-10} mbar above the base pressure of ca 4×10^{-10} mbar during ion-loading. Additionally a crucial advantage of photoionization over electron impact ionization is that charging of insulating parts near the ion-trapping zone is kept at a minimum. As we will see in **section 3.5.4**, the SCSI-MS mass measurement technique is very sensitive to charging of the ion-trap surroundings and even with the photoionization technique we have to take care to avoid stray light and reflections from the ionization beam that causes a similar charging.

2.3.1 Photoionization of calcium

Ionization of Ca atoms is accomplished by a single UV light source at 272 nm as sketched in **figure 2.5** (a). First the atom is excited on the $4s^2\,^1S_0 \rightarrow 4s5p\,^1P_1$ transition. With a lifetime of the $4s5p\,^1P_1$ state of 17-60 ns [58] the atom can decay either into the ground state or into the $4s3d\,^1D_2$ state [59], which in turn has a lifetime of 18 ms [60]. Absorption of a second photon from either the $4s5p\,^1P_1$ or the $4s3d\,^1D_2$ state, now leads to ionization. This scheme is isotope selective due to the isotope shift on the first transition. Measurements of the photonization rate versus the frequency of the 272 nm laser can be seen in **figure 2.5** (b). This clear show that the technique indeed is isotope-selective.

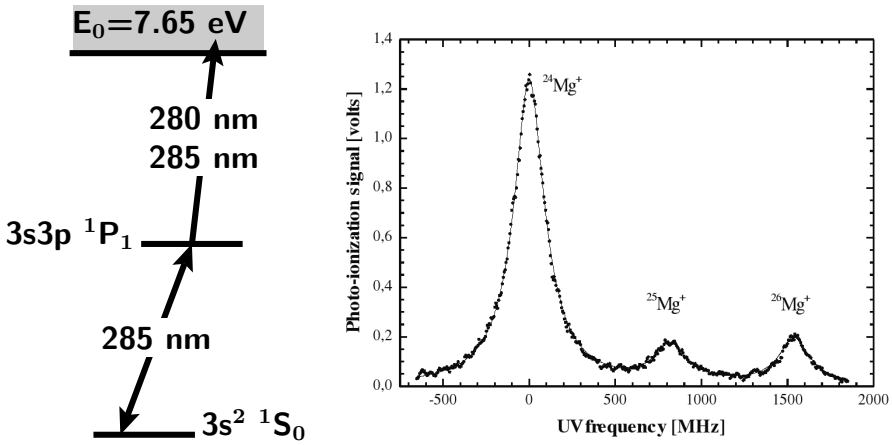

Figure 2.6 (a) Relevant energy levels for $^{24}Mg^+$ ionisation. First the atom absorbs a 285 nm photon, which excites it to the $3s3p\,^1P_1$ state. A subsequent absorption of either another 285 nm photon or a 280 nm photon from the laser cooling beam results in ionisation. (b) Photo ionisation spectrum for Mg^+ as a function of the detuning of the ionisation laser frequency relative to the $^{24}Mg^+$ [65].

The laser system for Ca ionization is composed of a Koheras Boostik distributed feedback (DFB) fiber laser and two consecutive frequency doubling steps [61, 62]. The first doubling step from 1088 nm to 544 nm is performed by a $LiNbO_3$ crystal mounted inside a home-made oven and placed in a bow-tie cavity. The second doubling step is performed by a BBO crystal placed in another bow-tie cavity locked by a Hänsch-Couillaud locking scheme [63].

2.3.2 Photoionization of magnesium

Mg atoms are resonantly ionized through the $3s^2\,^1S_0 \rightarrow 3s3s\,^1P_1$ transition at 285 nm as sketched in **figure 2.6** (a). From the $3s3s\,^1P_1$ state, the atom can be ionized by absorption of a second 285 nm photon, or a 280 nm photon from the laser cooling beam. In **figure 2.6** (b) the isotope selectiveness of the technique is demonstrated.

The laser system for magnesium ionisation consists of a single mode, tunable, cw ring dye laser using either Pyrromethene 556 or Rhodamine 6g dye and pumped by an Ar^+ laser. The output at 570 nm from the dye laser is then frequency doubled by a 5 mm long BBO crystal placed in an external bow-tie cavity [64] similar to the one used for the magnesium experiments.

2.4 Cooling of the atomic ions

Only a single laser beam propagating in a direction different from the three major axes of motion is needed when you Doppler laser-cool [66] a trapped particle in an harmonic potential well characterized by three different oscillation frequencies. We do, however, use two or three beams in our experiments, as sketched in e.g. **figure 3.1**. Two counter-propagating beams are always present along the z-axis, to balance the cooling force along this axis. This is especially relevant in the experiments with two-species Coulomb crystals (as presented in **chapter 6**), to avoid pushing all the laser-cooled ions down in one end of the crystal, but it also plays a role in the SCSI-MS technique, where such an asymmetry would lead to a shift in the trapping frequency (see **section 3.5.1**). When we do experiments with only a few ions aligned on the z-axis, an additional beam is used perpendicular to the trap axis, so that the cooling along the z-axis is decoupled from the cooling in the radial plane. In experiments with larger Coulomb crystal, this radial beam is not necessary as the Coulomb interaction between the ions couple the motion along different axes. In fact, if not very carefully aligned, a radial cooling beam tends to spin the crystal around the trap axis.

With these two cooling configurations, the laser-cooled ion(s) readily reach a temperature of ≈ 10 mK. At this temperature, the ions are localized to ≈ 1 μm or less, as seen in e.g. **figure 3.3**.

2.4.1 Cooling of Ca^+

A reduced energy level diagram for calcium is presented in **figure 2.7** (a). The ion is cooled on the $4s\ ^2S_{1/2} \leftrightarrow 4p\ ^2P_{1/2}$ transition by two or three 397 nm laser beams with typical intensities of around 0.1 W/cm^2 in each beam. To avoid optical pumping into the $3d\ ^2D_{3/2}$ level, a single 866 nm repumping beam is sent in along the trap axis.

The 397 nm light is provided by a frequency doubled Coherent 899 Titanium:Sapphire (Ti:Sa) laser, pumped by a Coherent Verdi V8 laser. The frequency doubling from 794 nm to 397 nm is done by a 12 mm long LBO crystal in a bow-tie cavity locked using a Hänsch-Couillaud lock [63]. The re-pump laser is a home-build diode laser, locked to a temperature stabilized reference cavity using a Pound-Drever-Hall locking scheme [67].

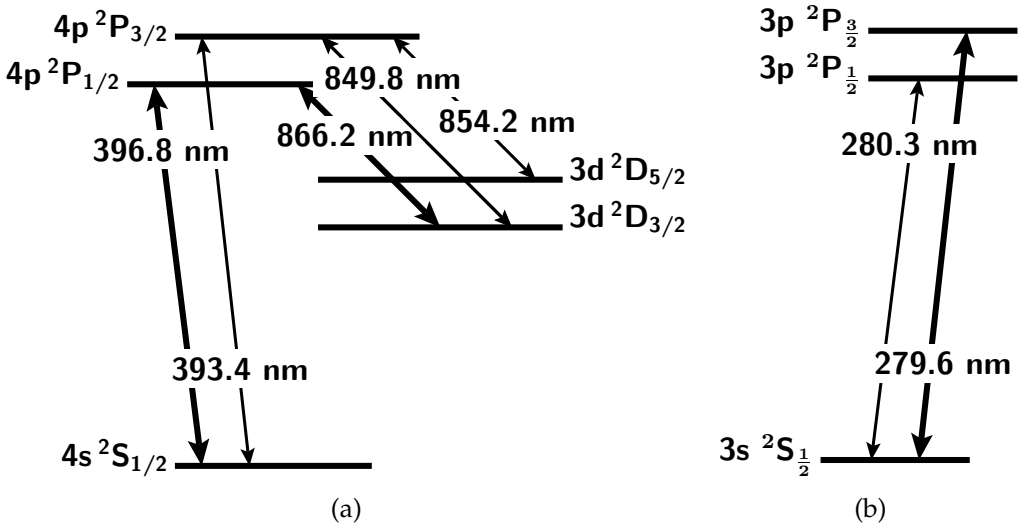

Figure 2.7 Reduced energy level diagrams of Ca^+ and Mg^+ with cooling transitions indicated by fat arrows. (a) Ca^+ ions are are laser cooled on the $4s\ ^2S_{1/2} \leftrightarrow 4p\ ^2P_{1/2}$ transition near 397 nm. An additional laser near 866 nm is needed to avoid optical pumping into the $3d\ ^2D_{3/2}$ level. (b) Mg^+ ions are lasercooled on the $3s\ ^2S_{1/2} \leftrightarrow 3p\ ^2P_{3/2}$ transition near 280 nm.

2.4.2 Cooling of Mg^+

$^{24}Mg^+$ and $^{26}Mg^+$ ions are laser-cooled on the $3s\ ^2S_{1/2} \leftrightarrow 3p\ ^2P_{3/2}$ transition (saturation intensity of $\approx$ 2.5 mW/mm^2). From the $3p\ ^2P_{3/2}$ state, the only allowed decay route is directly back into the ground state $3s\ ^2S_{1/2}$, as sketched in **figure 2.7** (b). We use linearly polarized light, but circularly would be just as fine as long as we utilize the $3p\ ^2P_{3/2}$ state. $^{25}Mg^+$ is slightly more complicated due to hyperfine splitting of both levels and would need a second repumping laser to avoid optical pumping into other hyperfine levels.

The laser light is produced by frequency doubling the output of an Ar^+ pumped single mode ring dye laser running on Pyrromethene 556 dye at 560 nm. The doubling unit is described in detail in Ref. [68].

2.5 Fluorescence Detection

Images of the laser-cooled ions are recorded by imaging fluorescence onto the surface of an image intensifier that is connected to a CCD camera via a relay lens of magnification of $\times 1$ or $\times \frac{1}{2}$. The magnification of the lens system that collects the

light is typically ×10, but this can be varied according to experimental needs. The total magnification for the experiments in **chapter 6** is only ×4, while the magnification in the few ion experiments (**chapter 3–5**) is as high as ×15.

The total photon detection efficiency of the imaging system is about 10^{-4} – 10^{-3} and we thus detect 10^3 – 10^4 photons per second. To determine positions of the ions, typically a few hundred detected photons are needed and the camera integration time has to be of the order of 100 ms. Discussion about the detection efficiency and resolution with respect to the precision of our experiments are postponed to **section 3.5.6**.

Examples of fluorescence images are presented in **figure 3.3** (a) for the case of two atomic ions in the ion trap, in **figure 3.3** (b) for an atomic ion together with an unknown and non-fluorescing ion and in **figure 6.7** for one and two-component crystals with approximately 3000 ions.

2.6 Trapping and cooling of molecular ions

Finally, a few words on molecular ions. The first task is to load the molecular ions into the trap. Here we basically have four different methods at our disposal, each with their own pros and cons, but all of them relying on the admittance of gas into the chamber. The simplest method is to leak in gas and wait for a reaction between a molecule and an already loaded and laser-cooled atomic ion. This method is used both in **chapter 5** and **6**, as well as in previous experiments [69, 70]. The drawback is of course the limited number of molecules accessible with this technique, since the product ion has to contain the laser cooled atomic ion and the reaction cross section has to be of a certain size. At the cost of an additional laser, it is also possible to photoionize molecules in the gas directly in the trapping region. This method can be applied to a wealth of molecules and shares many of the advantages of photoionization of atomic ions, i.e. it is an efficient load-on-demand technique, that only charge the insulating parts around the trap minimally. In **chapter 4** this method is used to load aniline ions ($C_6H_5NH_2^+$). If a complex molecular ion is already present in the trap, photodissociation is also a viable way of preparing fragment ions of interest (also demonstrated in **chapter 4**). Lastly, it is possible to ionize molecules by electron impact. This is, however, a rather brute way of loading ions without much control over which and how many ions are loaded, and this method was never used in this work.

When one or more molecular ions have been loaded into the trap, they are sympathetically cooled [71] to temperatures below 100 mK through the Coulomb interaction with co-trapped laser-cooled atomic ions. This happens on timescales

ranging from milliseconds if the ions are of roughly the same mass, up to several seconds when the molecular ion is much heavier than the atomic ion.

As already mentioned, the CCD camera records the emitted light from the laser-cooling process of the atomic ions. Since the molecular ions do not emit light, they are "invisible" in the images, but their presence is evident from the spatial configuration of the atomic ions. In the single ion case, the atomic ion is displaced from the center of the trap, as seen in **figure 3.3**, **4.2** and **5.1**, and in the many-ion Coulomb crystal case, ions are separated radially due to the mass dependence of **equation (2.7)**, see **figure 6.7**.

Chapter 3

Measuring the mass of a single ion

Since the first mass spectrometry methods was introduced by Thompson, Aston and Dempster nearly a century ago [72], it has proved itself a valuable tool throughout the fields of physics, chemistry and, recently, biology. Admittedly, many different methods have been developed since that time for different applications [73]. This chapter is devoted to a new mass measuring method recently demonstrated in our laboratory [37]. The main advantages of this mass measurement technique is the relatively high precision on single ions and the non-destructiveness, which implies that the measured ion can be used for further experiments.

In short, we measure the mass of a single trapped and cold atomic or molecular ion by resonantly exciting a motional mode of two-ion system in a harmonic trapping potential. The advantages of such single ion measurements are manifold. First of all, the single ion case avoids all the difficulties of ensemble averaging and provides a very "clean" experiment. Secondly, since the ion is trapped and cooled, it is spatially localized to within ≈ 1 μm. This renders it possible to manipulate the ion with focused laser beams. Third, the measurements are carried out under ultra-high vacuum conditions, such that no collisions perturb the internal state of the molecular ion. In a sense, a single trapped, cold and unperturbed molecular ion makes the ideal target for a wealth of investigations.

The chapter is organized as follows. In **section 3.1** we will compare our new technique to other already established techniques. We discuss the additions to the experimental apparatus needed for this technique in **section 3.2**. To test the precision of our technique, some measurement on atomic ions have been made. They are presented in **section 3.4**, while the accuracy of our technique and possibilities for improving it are discussed in **section 3.5**. Results on molecular ions are postponed to later chapters (**4** and **5**).

3.1 Single ion mass measurements

In this section we will first take a brief look at existing mass spectrometer techniques which have the ability to measure masses of single ions. After this, we will introduce our mass measurement technique and discuss some of the pros and cons over other techniques.

3.1.1 Common single-ion mass spectrometry techniques

Detection of a single ion is in general fairly easy and can be achieved with almost 100% efficiency with an electron multiplier detector, if the particle is accelerated to an energy of a few eV. Several traditional mass spectrometers, such as the quadrupole mass filter (QMF) [74, 75] and the time-of-flight (TOF) instrument [74, 76], utilize this feature to gain single ion sensitivity. The detection mechanism is, however, destructive.

A non-destructive single ion mass measurement can be achieved with the more recent technique of Fourier Transform Ion Cyclotron Resonance (FT-ICR) mass spectrometry [77]. Here the cyclotron frequency of the induced image charge motion is measured in pick-up plates. From this frequency, the ion mass can be obtained with a formidable accuracy. Compared to the relative mass resolution of QMF and TOF mass spectrometers around $\frac{\Delta m}{m} = 10^{-2} - 10^{-6}$, the FT-ICR technique reaches an impressive resolution of $\frac{\Delta m}{m} = 10^{-11}$ [78], where m is the mass of interest and Δm the uncertainty with which it can be determined. The ability to make spatial and time resolved measurements are however limited.

This imply that QMF and TOF mass spectrometers are usually applied in fast dynamic experiments where the mass of the particles of interest may change due to reactions or photofragmentation, while FT-ICR is applied most often in "static" high precision measurements and slower dynamics situations.

3.1.2 The SCSI-MS technique

In our technique, an unknown (atomic or molecular) ion is trapped together with a laser-cooled atomic ion. Through the Coulomb interaction, the unknown ion is sympathetically cooled down to a temperature of a few mK. This results in a crystallization of the two-ion system, which can be observed by imaging the fluorescence from the laser-cooled ion onto a CCD camera. The fluorescence from the laser-cooled ion appears as a spot displaced a certain distance from the center of the trap [see e.g. **figure 3.3** (a)]. The mass measurement relies on the determination of the resonant excitation frequency of one of the two oscillatory modes of this trapped and crystallized linear two-ions system [79, 80]. These two modes will be named the center-of-mass (COM) mode and the breathing (BR) mode throughout this thesis. In the COM mode, the ions move with the same phase, while in the BR mode, the motions of the ions are out of phase. From the measured frequency, the mass of the unknown ion can be determined from a simple relation between the frequency and the relative masses of the two ions. In the following we will

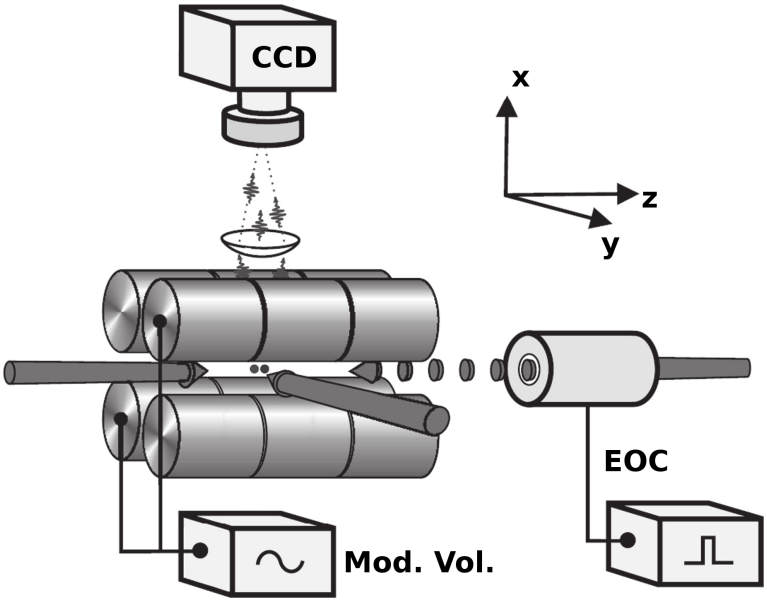

Figure 3.1 Sketch of the SCSI-MS technique. Shown in the figure are the linear RF ion-trap electrodes, the cooling laser beams and the CCD camera used to monitor the fluorescence from the laser-cooled atomic ion. An image-intensifier-based shutter that can be gated phase-locked to a periodic driving force is installed in front of the camera. A driving force, for excitation of the ion motion along the z-axis, is applied either in the form of a sinusoidally-varying voltage applied to the end-cap electrodes of the ion trap or through modulation of the scattering force on the atomic ion by using an electro-optical chopper (EOC) for intensity modulation.

refer to our technique as Sympathetically Cooled Single Ion Mass Spectrometry (SCSI-MS).

In **figure 3.1** a sketch of the SCSI-MS setup is presented. The two-ion system is aligned along the trap's main axis, which we will refer to as the z-axis from now on. The motion of the two ions can be excited either by a sinusoidally-varying electric field along the z-axis, which is achieved by adding a modulation voltage to some of the end-cap electrodes of the trap, or by modulating the cooling intensity of at least one of the cooling laser beams propagating along the z-axis; this intensity modulation causes a periodically-varying scattering force on the laser cooled atomic ion. If we, for the moment, ignore the damping exerted by the cooling lasers, the resonance frequency is most easily determined as the modulation frequency at which the ion motion amplitude is largest. If the integration

time of the camera is much longer than the period of the oscillation, this is oberseved as a "smearing" of the fluorescence spot [see **figure 3.3** (b)]. With this method one can easily get a mass resolution below 10^{-2} and with optimized parameters, a mass resolution around 10^{-4} is reached. Additionally, it is possible to monitor the phase of the ion motion relative to the modulation by gating the camera such that only light emitted at a certain phase of the motion is detected. In this case, a relative mass resolution around 10^{-4} is also achieved.

After the mass measurement has been performed, both the laser cooled atomic ion and the unknown ion are again translationally cold and well-localized. This renders the SCSI-MS technique highly relevant to a wealth of future experiments (see **section 3.6**).

3.1.3 Advantages and disadvantages of the SCSI-MS technique

In contrast to QMF and TOF mass spectrometer techniques mentioned above, SCSI-MS offers a non-destructive mass measurment while maintaining the high spatial and temporal resolution. However, whereas the relative mass resolution of $\approx 10^{-4}$ can compete well with that of QMF and TOF mass spectrometry, it will probably never be able to challenge that of FT-ICR mass spectrometry. Yet, our new technique is still highly relevant. Where FT-ICR spectrometers rely on a cryogenically cooled superconducting solenoid obstructing direct access to the ions, the SCSI-MS technique is centered around the simple and open Paul trap structure, that easily integrates laser and molecular beams. Furthermore, commersialization could be possible in the future through the ongoing effort to build micro-traps (see for example Ref. [81]).

Currently, the SCSI-MS technique is limited in the range of masses that can be accessed. To achieve stable operating conditions of the two-ion system in the Paul trap, the mass of the unknown ion should be within the range of $\approx (0.3 - 3)m_1$, where m_1 is the mass of the laser-cooled atomic ion. At the present time, only Mg^+ and Ca^+ ions can be trapped and laser-cooled in our laboratory, but with the implementation of systems for cooling other ions, all singly-charged ions within the range of 1 to $\approx$ 600 u should be measurable. The mass range could also be increased when a general procedure to align two ions along the trap axis of a Penning trap becomes available. Axial alignment of two laser-cooled Mg^+ ions has already been demonstrated in a Penning trap [82]. Another possible way to increase the mass range could be to work with higher-charge states.

Most mass spectrometers measure the charge-to-mass ratio, but since the equilibrium positions of the two ions depend on the charge, both the mass and the charge are actually measured independently with SCSI-MS.

Also note that, in contrast to standard mass measurement techniques, a strong Coulomb interaction between the ions is essential, rather than being problematical. The non-linear nature of the Coulomb interaction can, however, lead to unwanted systematic errors in the mass measurement, as discussed in **section 3.5.2**.

3.2 Experimental realization

Most of the experimental arrangement was already presented in **chapter 2**, but two things remain: inducing and detecting the ion motion.

3.2.1 Inducing driven motion of the ions

To determine the common mode resonance frequency, the motion of the two-ion system is excited by applying a periodic driving force. This can either be achieved by applying a sinusoidally-varying voltage to some of the end-cap electrodes of the ion trap or by modulating the radiation pressure force. This can be done by chopping the intensity of a cooling laser beam propagating along the z-axis with an electro-optic chopper (EOC) (see **figure 3.1**). Both methods are utilized in our laboratory and test mass measurement experiments have shown that, at least at the level of $\frac{\Delta m}{m} \approx 10^{-3}$, the two methods do not lead to any systematic differences.

In both cases, the frequency sweeps are controlled from a home-built programmable frequency synthesizer. It provides a sinusoidal modulation voltage output used when exciting the ion motion via the electric force and a TTL output that controls the electro-optic chopper. The synthesizer is able to step through a series of frequencies and, thus, able to perform a scan across the expected resonance while delivering a trigger signal to the camera to ensure a well-defined frequency during the acquisition of a single image. In addition, the synthesizer outputs a short gating pulse with a variable phase delay that can be used to gate the image intensifier when we do phase measurements (see **section 3.2.2.2**). The size of the frequency steps, the time between each step, and the modulation amplitude are adjustable and provide flexibility for the tailoring of scans. Furthermore, the synthesizer can hold up to 10 predefined scans in its memory, which together with an option to loop when reaching the end of the last scan, permits repeated frequency scans of relevant masses with minimum down time. For convenience,

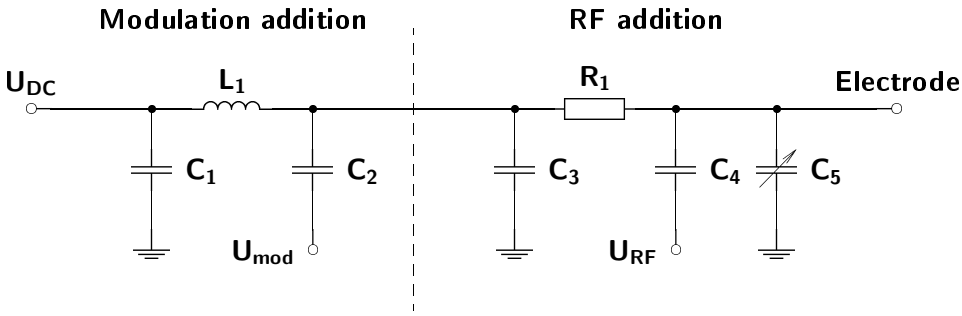

Figure 3.2 Electrical diagram showing how the modulation voltage is added to the electrode trapping voltages.

settings can be uploaded to the synthesizer from a small LabView program via a serial port (RS232) interface.

3.2.1.1 Electrical forces

To achieve a sinusoidally-varying driving force along the z-axis, the analog output from the frequency synthesizer is added as a modulation voltage to two or four end-cap electrodes of the ion trap (see **figure 3.1**). The COM mode can be excited by applying a time-varying homogeneous electric field along the z-axis. This field can be achieved by modulating the voltage applied to two diagonally-opposed end-cap electrodes at one end of the ion trap. In order to excite the BR mode, a time-varying electric field that has a gradient along the z-axis is needed. This situation can be realized by applying a common modulation voltage simultaneously to diagonal sets of end-cap electrodes at both ends of the ion trap.

Three potentials are combined in order to achieve the desired degree of control of the electrode potential; these potentials are (1) a constant DC potential for axial trapping, (2) a modulation potential of $\approx$ 100 kHz for COM and BR mode excitation, and (3) an RF potential of $\approx$ 4 MHz for ion trapping in the radial plane. As indicated in the diagram shown in **figure 3.2**, the modulation voltage is added to the DC voltage before it is combined with the RF voltage and led ultimately to the ion trap. The L_1, C_1 filter suppresses the modulation voltage on the DC end; the R_1, C_3 filter ensures a strong suppression of RF voltage at the DC end while allowing a fraction of the modulation voltage to pass the other way. The adjustable capacitor, C_5, is used for fine-tuning the RF voltage on the electrode.

3.2.1.2 Radiation pressure forces

Besides cooling of the atomic ion, the radiation pressure force can also be used to exert a periodic force on the atomic ion if the intensity of one or both laser-cooling beams propagating along the z-axis is modulated. The intensity modulation is achieved by directing the laser cooling beam through an electro-optic modulator (EOM) followed by a linear polarizer. By appropriate adjustment of the polarization of the laser beam entering the EOM and the orientation of the polarizer, the two optical elements can together act as an EOC when the correct voltages are applied to the EOM. In contrast to the electric driving force, the radiation pressure force only acts on the laser cooled atomic ion and the same setup can be used to excite both the COM and the BR mode without any changes to the apparatus.

3.2.2 Detection of the motion of the ions

The detection of the ion motion is done by the image intensifier together with the CCD camera. The image intesifier can be opperated in either normal mode or in gated mode, where the gating signal is delivered from the frequency synthesizer described in **section 3.2.1**. In normal mode operation, only the amplitude of the ion motion is recorded. Thus we will use the term "amplitude detection". In gated mode, the relative phase between the ion motion and the driving force is detected as well, and we will denote it as "phase detection" throughout the rest of this work.

3.2.2.1 Amplitude detection

The image intensifier is always active in the amplitude method. With typical exposure times of $\approx$ 100 ms and ion resonance frequencies around 100 kHz, the motion of the ions are integrated over 10^4 oscillation periods. Examples of images of a laser cooled $^{40}Ca^+$ ion and an "invisible" $^{24}Mg^+$ ion can be seen in **figure 3.3**. In (a), the frequency of the driving force is far from the resonance frequencies, $\omega_\pm$ and the ions are well localized in their equilibrium positions (see **equation (3.2)**). In (b), on the other hand, the frequency is close to the COM frequency, and the smearing of the fluorescence as compared to (a), clearly shows that the ions are excited motionally.
As mentioned in **section 3.2.1**, the frequency synthesizer delivers a trigger signal to the camera, ensuring a well-defined frequency in each image. Each image is analyzed automatically in a simple Matlab script in the following way: First the ion

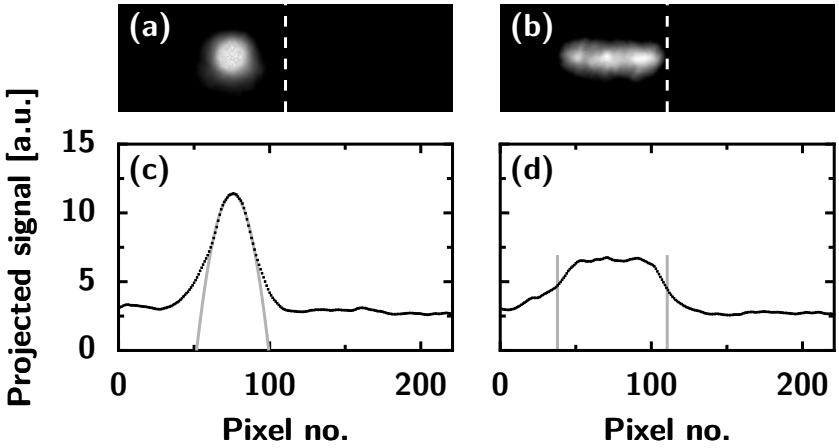

Figure 3.3 (a) and (b) Images of a laser-cooled $^{40}Ca^{+}$ ion, co-trapped with sympathetically cooled $^{24}Mg^{+}$ ion. In (a) the frequency of the modulation force is far from the resonance frequencies, $\omega_{\pm}$, while in (b), the frequency is near the COM mode resonance frequency of 62.5 kHz. An exposure time of 100 ms was used in both images. (c) and (d) The fluorescence intensity signal projected onto the z-axis. In (d) the FWHM is indicated with vertical grey lines. In (c) a fitted parabola used for robust position determination is shown.

Figure 3.4 (Opposite) The position-resolved ion fluorescence for two $^{40}Ca^{+}$ ions along the ion-trap axis as a function of the drive frequency of the modulation voltage. Each gray scale contour plot is composed of axial projections of the ion fluorescence intensity in images recorded during the frequency scans (step size: (a,c) 25 Hz/image, (b,d) 100 Hz/image). (a) and (c) show an excitation of the COM mode with the image intensifier in normal and gated modes, respectively, while (b) and (d) show an excitation of the breathing mode (BR) also with the image intensifier in normal and gated modes, respectively. The dark lines in the fluorescence track in (a) and (c) are due to shelving of the $^{40}Ca^{+}$ ion in the non-fluorescing $3d^{2}D_{5/2}$ state [83]. (e and f): Amplitude of the ion motion as a function of the drive frequency. The amplitude is found from (a and b), respectively, as the difference between the HWHM of the fluorescence signal at a given drive frequency and the HWHM of the non-excited ion (that is, at a far-off resonant drive frequency). (g and h): In-phase amplitude of the ion motion as a function of the drive frequency. The in-phase amplitude is found from (c and d) as the center of the upper ion fluorescence track.

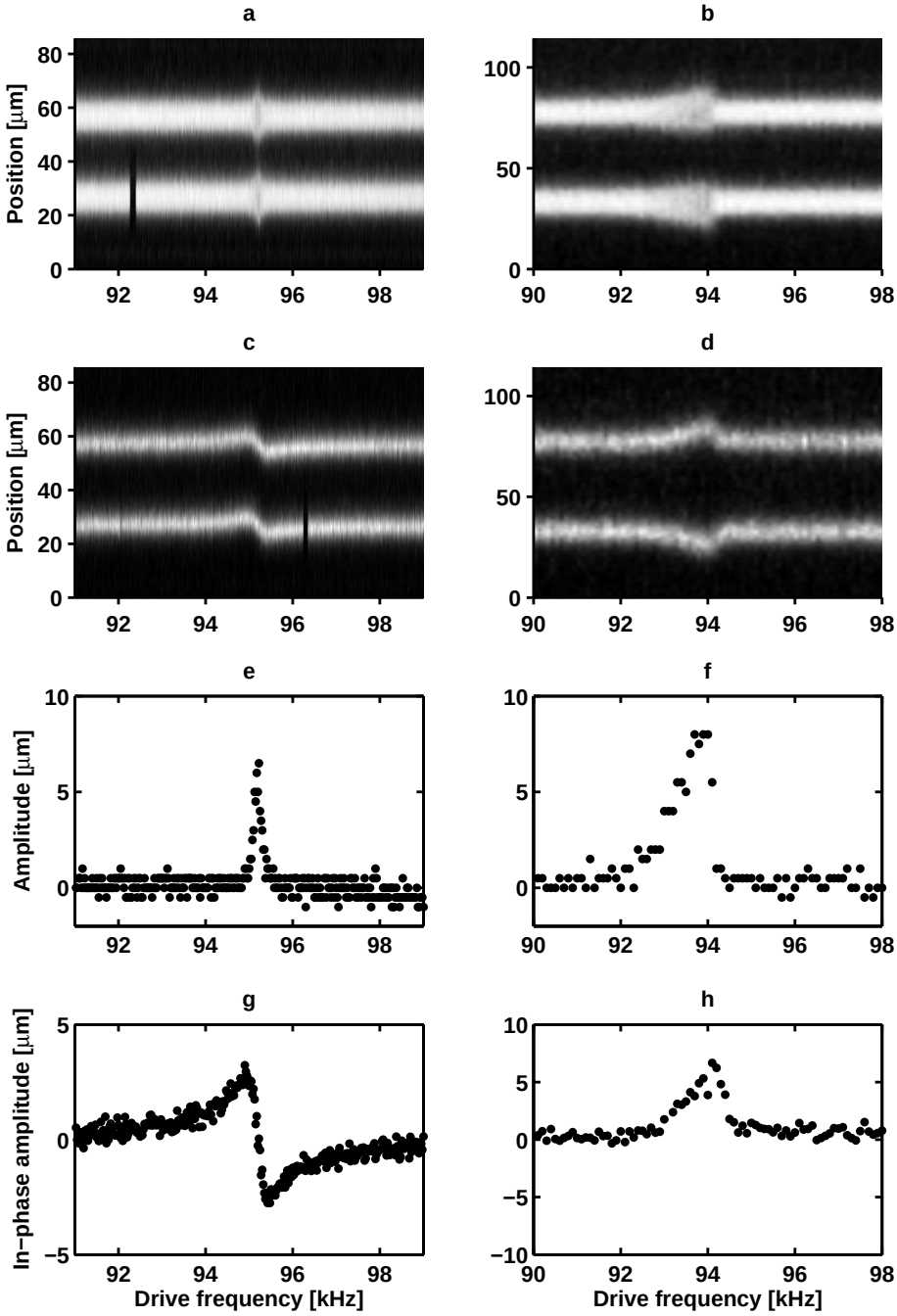
a
b
c
d
e
f
g
h
Position [μm]
Amplitude [μm]
In−phase amplitude [μm]
Drive frequency [kHz]
Drive frequency [kHz]

fluorescence intensity is projected onto the z-axis, as seen in **figure 3.3** (d). Then the FWHM is found by a threshold analysis, as indicated by the grey lines. Finally the amplitude of the ion motion is determined as half the difference between the FWHM of the fluorescence signal at a given drive frequency and the FWHM of the non-excited ion. In this way the frequency-dependent amplitude can be plotted as seen in in **figure 3.4** (e).

Another way of visualizing the data are by stacking together the projected fluorescence signals to form a contour plot, see e.g. **figure 3.4** (a) and (b) where the frequency is scanned across the COM and BR mode frequencies for two $^{40}Ca^{+}$ ions, respectively. The gap in the lower trace in (a) is due to temporary shelving of the $^{40}Ca^{+}$ ion in the $3d\,^2D_{5/2}$ state.

For many purposes (see e.g. **chapter 4** and **5**) it is sufficient simply to determine the modulation frequency where the amplitude is maximal, which for small damping forces and ions of similar mass, occurs very close to the resonance frequency. The cooling rate coefficient γ is typically such that $\frac{\gamma}{\omega_{\pm}}$ is $\approx 10^{-3} - 10^{-2}$, which leads to a relative error in the measurement of $\omega_{\pm}$ smaller than 10^{-4}. A quick max-amplitude estimate will give an accuracy of $\approx 10^{-2}$.

As we will see in the following sections, however, more precise determinations of the normal frequencies are also possible with the amplitude detection method. This is achieved by fitting an expression for the amplitude of the laser-cooled ion as a function of the drive frequency (see **equation (3.9)** for identical ions and **equation (3.11)** for non-identical ions).

3.2.2.2 Phase detection

In the phase detection method, the image intensifier is gated such that the camera only integrates light emitted in a short time interval at a certain phase with respect to the driving force. Hence it is the amplitude of the component of the ion motion which is in-phase with the driving force that is recorded. This in-phase amplitude of the COM mode has a characteristic dispersive profile, as observed in **figure 3.4** (c) and (g), and features a sharp zero-crossing near or at ω_{+}.

When the laser light is modulated, the voltage pulse for the gating signal can be overlapped temporally with the light pulse by detecting the latter with a photo diode. The adjustment of the detection phase is slightly more difficult when using the electrode excitation driving force, because the circuit used to couple the driving voltage to the electrodes leads to a frequency-dependent phase shift of the signal originating from the frequency synthesizer.

Again, the analysis of the recorded images is done automatically by a MatLab script. The value of interest is the z-coordinate of the ion, which can be found with good accuracy as the maximum of a parabola fitted to the projected fluorescence intensities close to the center of the ion position [see e.g. **figure 3.3** (c)].

3.3 Theory of the driven motion of a two-ion system

Now, lets turn to the theory behind the driven motion of the two-ion system. As we saw in **section 2.2**, the potential energy of a single particle close to the center of the trap is well described by a harmonic potential. Extending this result to two singly-charged ions aligned along the z-axis, we can write the one-dimensonal potential as:

$$\phi(z_1, z_2) = \frac{1}{2}\kappa z_1^2 + \frac{1}{2}\kappa z_2^2 + \frac{e^2}{4\pi\epsilon_0|z_2 - z_1|} \tag{3.1}$$

where z_1 and z_2 are the positions of the two ions, respectively, κ is a spring constant, and ϵ_0 is the permittivity of vacuum. By differentiation the equilibrium positions of the ions when cooled to low temperatures are easily found to be $z_2 = -z_1 = \frac{\Delta z}{2}$ for $(z_2 > z_1)$, with

$$\Delta z = \left(\frac{e^2}{2\pi\epsilon_0\kappa}\right)^{1/3} \tag{3.2}$$

being the equilibrium ion distance.

Now, the strong Coulomb interaction between the ions couples the motion of these, which gives rise to two axial normal motional modes. Expressing the spring constant κ in terms of the single ion oscillation frequency of the ions

$$\kappa = m_i\omega_i^2 \qquad (i = 1, 2), \tag{3.3}$$

the eigenfrequencies of these two modes can be found to be [80]

$$\omega_\pm^2 = \left(1 + \frac{1}{\mu} \mp \sqrt{1 - \frac{1}{\mu} + \frac{1}{\mu^2}}\right)\omega_1^2, \tag{3.4}$$

where $\mu = \frac{m_2}{m_1}$. The solutions ω_+ and ω_- correspond to the mode with eigenvectors where the ions move in phase (COM mode) and out of phase (BR mode), respectively, with mass-dependent amplitudes. These eigenvectors are given by

$$\boldsymbol{q}_{\pm} = N_{\pm}\left(\frac{1-\mu \mp \sqrt{1-\mu+\mu^2}}{\sqrt{\mu}}, \frac{1}{\sqrt{\mu}}\right), \tag{3.5}$$

where $N_{\pm}$ is a normalisation constant.

The SCSI-MS technique relies on the mass dependence of the oscillation frequency of the two normal modes expressed in **equation (3.4)**. By measuring either ω_+ or ω_- as well as ω_1 (the oscillation frequency of the known laser-cooled ion species), the mass ratio μ and, hence, the mass m_2 of an unknown ion species can be determined. Alternatively, from a measurement of the ratio between ω_+ and ω_-, **equation (3.4)** gives rise to an equation with solutions μ and $\frac{1}{\mu}$. In this case, μ can be determined without measurement of ω_1, provided that it is known that either $\omega_1 > \omega_+$ or $\omega_1 < \omega_+$.

In **section 3.2.1**, we already described how we try to determine ω_1, ω_+ , and ω_- by resonant excitation of the ion motion through the application of a periodic driving force. The situation is complicated, however, by the always present damping force caused by the laser-cooling of one (or both) of the ions. Taking this into account, the equations of motion read

$$\ddot{z}_1 - \frac{F_{\text{Dopp},1}(\dot{z}_1)}{m_1} + \omega_1^2 z_1 = -\frac{e^2}{4\pi\epsilon_0 m_1 (z_2 - z_1)^2} + \frac{F_{\text{drive},1}}{m_1}\cos(\omega t) \tag{3.6}$$

and

$$\ddot{z}_2 - \frac{F_{\text{Dopp},2}(\dot{z}_2)}{m_2} + \omega_2^2 z_2 = -\frac{e^2}{4\pi\epsilon_0 m_2 (z_2 - z_1)^2} + \frac{F_{\text{drive},2}}{m_2}\cos(\omega t) \tag{3.7}$$

where $F_{\text{Dopp},i}$ denotes the Doppler cooling force applied to ion i and $F_{\text{drive},i}$ is the driving force applied to ion i. If the ions are identical, they are both subjected to cooling and $F_{\text{Dopp},1} = F_{\text{Dopp},2}$. For different ions, we assume that only ion 1 is laser-cooled and $F_{\text{Dopp},2} = 0$. Similarily, for excitation via laser intensity modulation, we have either $F_{\text{drive},1} = F_{\text{drive},2}$ for identical ions or $F_{\text{drive},2} = 0$ for different ions. Using end-cap electrode excitation, we choose $F_{\text{drive},1} = F_{\text{drive},2}$ for COM mode excitation and $F_{\text{drive},1} = -F_{\text{drive},2}$ for BR mode excitation.

Assuming small ion velocities, the Doppler cooling force can be approximated by a viscous damping force that is proportional to velocity, $F_{\text{Dopp},i} = -m_i\gamma_i z_i$, where γ_i is a constant that depends on the laser wavelength, intensity, detuning, and the ion mass [66]. The validity of this approximation will be discussed in **section 3.5.1**, but in many cases it is a good one.

To uncouple **equation (3.6)** and **(3.7)**, we assume small velocities and small excursions from the equilibrium positions. In this case the identical-ion-system

can be described in terms of normal mode coordinates $z_+ = \frac{z_2+z_1}{2}$ and $z_- = \frac{z_2-z_1-\Delta z}{2}$ for the COM and the BR mode, respectively, by the uncoupled equations of motion

$$\ddot{z_\pm} + \gamma\dot{z}_\pm + \omega_\pm^2 z_\pm = \frac{F_\pm}{m_1}\cos(\omega t) \tag{3.8}$$

where $F_\pm = (F_{\text{drive},2} \pm F_{\text{drive},1})/2$. Each of these equations of motion is that of a classical driven, damped harmonic oscillator with the solution leading to

$$\begin{aligned} z_1(\omega, t) &= \frac{F_\pm}{\sqrt{2}m_1\sqrt{(\omega^2-\omega_\pm^2)^2+\gamma^2\omega^2}}\cos(\omega t+\phi) - \frac{\Delta z}{2} \\ &\equiv z_0(\omega)\cos(\omega t+\phi) - \frac{\Delta z}{2} \end{aligned} \tag{3.9}$$

where

$$\cos(\phi) = \frac{\omega_\pm^2-\omega^2}{\sqrt{(\omega^2-\omega_\pm^2)^2+\gamma^2\omega^2}} \tag{3.10}$$

For ions with different masses, the solution of the equation of motion for the "detector" ion (ion 1) is much more complex [84] and reads as

$$\begin{aligned} z_1(\omega,t) = \frac{F_{\text{drive},2}}{\kappa}\Bigg[&\cos(\omega t+\phi)(2\omega_2^2-\omega^2) \\ &\times\sqrt{\frac{\left[(2\omega_1^2-\omega^2)+\frac{F_{\text{drive},1}}{F_{\text{drive},2}}\omega_1^2\right]^2+\gamma^2\omega^2}{\left[\omega^4-2(\omega_1^2+\omega_2^2)\omega^2+3\omega_1^2\omega_2^2\right]^2+\gamma^2(2\omega_2^2-\omega^2)^2\omega^2}} \\ &-\cos(\omega t)\Bigg] - \frac{\Delta z}{2} \end{aligned} \tag{3.11}$$

where

$$\begin{aligned} \cos(\phi) = \frac{[(2\omega_1^2-\omega^2)F_{\text{drive},2}+\omega_1^2F_{\text{drive},1}][\omega^4-2(\omega_1^2+\omega_2^2)\omega^2+3\omega_1^2\omega_2^2]}{|\omega^4-2(\omega_1^2+\omega_2^2)\omega^2+3\omega_1^2\omega_2^2+i\gamma(2\omega_2^2-\omega^2)\omega^2|}\cdots \\ \cdots\frac{+F_{\text{drive},2}\gamma^2(2\omega_2^2-\omega^2)\omega^2}{\times|(2\omega_1^2-\omega^2)F_{\text{drive},2}+\omega_1^2F_{\text{drive},1}+i\gamma\omega F_{\text{drive},2}|} \end{aligned} \tag{3.12}$$

with $\omega_i \quad (i = 1, 2)$ defined through $\kappa = m_i\omega_i^2$.

Near ω_+ and ω_- the amplitude of the laser cooled ion motion is enhanced. The maximal amplitude is shifted a bit by γ, which also approximately sets the width of the resonance. As for identical ions, the in-phase amplitude shows a dispersive profile with a zero-crossing at ω_+ and ω_- when only the laser-cooled ion is subjected to a driving force (excitation by laser modulation). For the electrode excitation method, where both ions are driven, the zero-crossing is offset from ω_+ or ω_- by an amount that, for $\frac{\gamma}{\omega_\pm} \ll 1$ is of the order of $(\frac{\gamma}{\omega_\pm})^2$. This can intuitively be explained by the perturbance of the phase of the laser cooled ion motion by the driven motion of the non-cooled ion. In contrast, when only one ion is driven, the other ion is "pulled" or "pushed" into phase with the driven ion.

While the amplitude and the in-phase signals for the COM mode are well described by this basic theory, the first order expansion of the Coulomb interaction is not precise enough for the BR mode and a strong asymmetry is observed (see **section 3.4** below). This asymmetry is discussed in **section 3.5.2**.

3.4 Experimental results

We have performed a series of experiments with atomic ions to test the accuracy of the SCSI-MS technique. They involve either two laser-cooled $^{40}Ca^+$ ions or one laser-cooled $^{40}Ca^+$ ion trapped together with another Ca^+ isotope or a Mg^+ ion. Experiments with single molecular ions are postponed to separate chapters; see **chapter 4** for experiments that demonstrate trapping and sympathetic cooling of single more complex ions, namely aniline ions, together with a study of their consecutive photofragmentation and **chapter 5** for a study of the reaction $Mg^+ + HD \rightarrow MgD^+ (MgH^+) + H(D)$, in which we observe a strong isotope effect.

3.4.1 Two calcium ions

When deriving **equation (3.8)** for identical ions, we did not expand the Coulomb interaction term. Thus the solution in **equation (3.9)** is valid for arbitrary amplitudes, and ω_+ can be determined accurately from a fit to the data. This was verified by recording the amplitude as a function of the drive frequency for a range of different driving forces. All of the amplitudes could be fitted to **equation (3.9)** and, as shown in **figure 3.5**, the center frequencies near 95.625 kHz are identical within 20 Hz, thus showing good agreement with the basic theory.

In contrast, **equation (3.8)** for the BR mode is correct only for small amplitudes. As shown in **figure 3.6**, even at moderate amplitudes a significant asymmetry of the amplitude profile is evident. As we discuss in more detail in **section 3.5.2**,

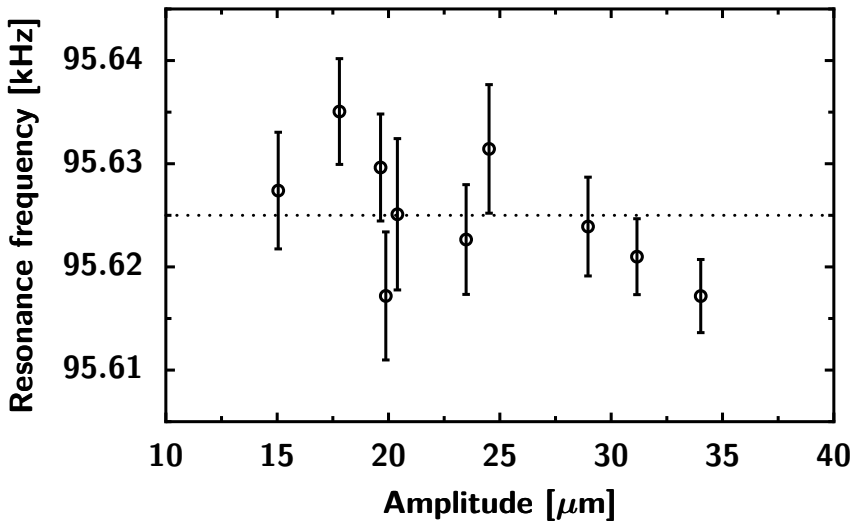

Figure 3.5 Measured oscillation frequency for the COM mode of two laser-cooled $^{40}Ca^{+}$ ions at different amplitudes. The dotted line indicates the mean value of 95.625 kHz.

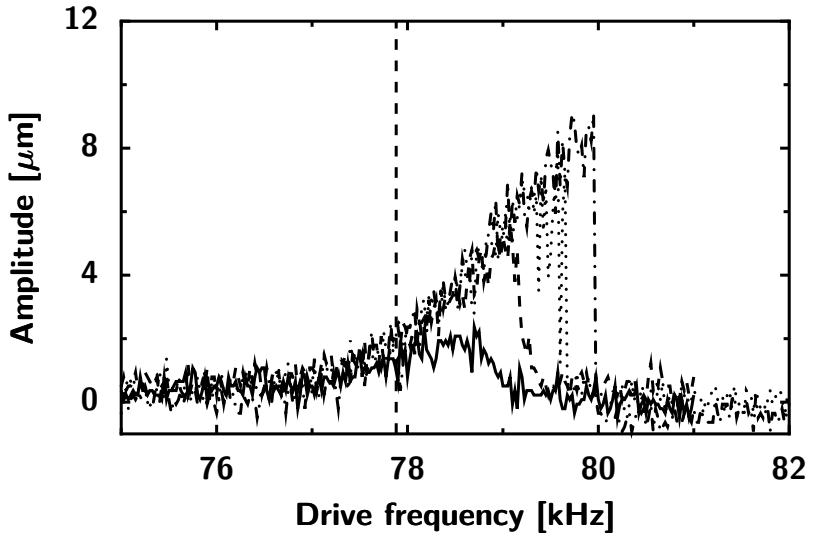

Figure 3.6 Amplitude vs. drive frequency for the BR mode of two laser-cooled $^{40}Ca^{+}$ ions at different driving forces. The vertical line indicates the expected BR resonance frequency assuming no non-linear frequency pulling.

the shape of the amplitude profile is caused by a non-linear response ("frequency-pulling" [85]) because the oscillation frequency is increasing with the amplitude.

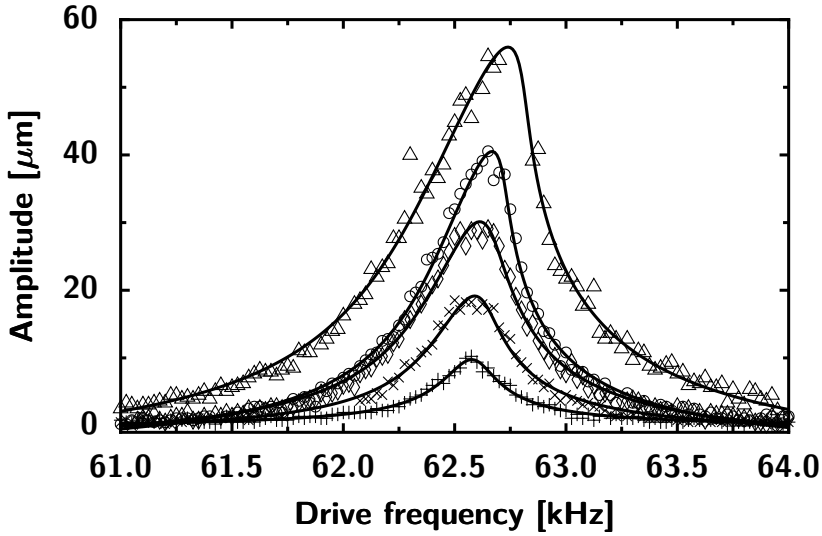

Figure 3.7 Amplitude vs. drive frequency for the COM mode of one laser-cooled $^{40}Ca^{+}$ ion and one $^{24}Mg^{+}$ ion at different driving forces. The solid lines indicate fits to a model similar to that developed by Evoy et al. [86]. The fits yield the same resonance frequency for all of the five scans.

While frequency-pulling is an interesting non-linear phenomenon, in the present context it leads, unfortunately, to difficulties in making an accurate determination of the "true" BR mode frequency, that is, the eigenfrequency at small amplitudes. The expected BR mode frequency in the above measurements, as indicated by the dashed line in **figure 3.6**, is almost 1 kHz away from what we would naively guess from the data.

3.4.2 One calcium and one magnesium ion

In the case of two non-identical ions, the COM mode frequency is also amplitude dependent. To investigate this effect, the amplitude was recorded as a function of drive frequency for one laser-cooled $^{40}Ca^{+}$ ion and one $^{24}Mg^{+}$ ion. As shown in **figure 3.7**, we only observe a significant asymmetry of the amplitude profile at large amplitudes. The small asymmetry observed at low amplitudes can be explained by the slightly asymmetric shape of the amplitude predicted by **equation (3.11)**; such an asymmetry is predicted also by **equation (3.9)** where it can be recognized as being due to the damping coefficient γ. The BR mode motion for two non-identical ions shows an asymmetry similar to that shown in **figure 3.6**

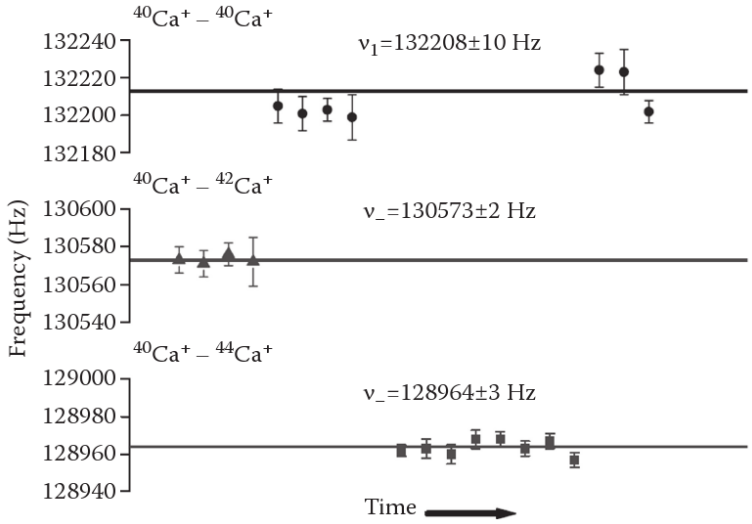

Figure 3.8 Reproduced from Ref. [37]. Measured oscillation frequencies for three combinations of Ca^+ isotopes. The stated resonance frequencies are the statistical averages of the respective data points [37]. The horizontal position of the data points reflects the time order of the experiments.

for two identical ions. Figures **3.4** through **3.7** indicate that the "true" COM mode frequency can be determined more easily and more accurately than the "true" BR mode frequency. While this statement is generally correct, there may occasionally be good reasons to make use of the BR mode as is discussed further in **section 3.5** [86].

3.4.3 Precision mass measurements of calcium isotopes

Although not part of this PhD work, a few precision mass measurements of calcium isotopes performed in this group are presented here for completeness [37]. The masses of the calcium isotopes $^{42}Ca^+$ and $^{44}Ca^+$ were measured with reference to the mass of the $^{40}Ca^+$ ion; one of the isotopes was trapped together with a $^{40}Ca^+$ ion and the COM resonance frequency was determined by the phase-detection method. As a reference, the COM frequency for two $^{40}Ca^+$ ions was determined also by the phase-detection method. The experimental oscillation frequencies from a series of measurements are presented in **figure 3.8**. Using **equation (3.4)**, mass ratios of $\mu_{40/42} = 0.9526(3)$ and $\mu_{40/44} = 0.9095(3)$ can be deduced from the results. Within the uncertainties of 3×10^{-4} these results are in agreement with the expected values of $\mu_{40/42} = 0.952441$ and $\mu_{40/44} = 0.909174$ [87].

3.5 Accuracy of the SCSI-MS technique

In this section, we will discuss various effects that limit the accuracy of the SCSI-MS technique.

3.5.1 Laser-cooling force

A main ingredient in the SCSI-MS technique, is Doppler laser-cooling which serves several purposes. First, it acts as a damping force that cools the atomic ion directly, and the unknown atomic or molecular ion indirectly through the Coulomb interaction in the two-ion system. Secondly, the fluorescence photons are used in the detection process. Third, as described in **section 3.2.1.2**, it can be used to induce the common motion of the ions by modulating the intensity.

It does, however, also introduce some complications. To understand the broadening and shift of resonances, we approximated the Doppler cooling force by a frictional force characterized by a friction (or cooling) rate Γ in **section 3.3**. This approximation is only valid when the velocity of the cooled ion is much smaller than the absolute value of the detuning of the laser cooling light, $|\delta|$, divided by the wavenumber, $k = \frac{2\pi}{\lambda}$, of the light driving the cooling transition [66].

Typical excitation amplitudes in our experiments are around 10 μm, which for resonance frequencies $\omega_{\pm} \approx 2\pi \times 100$ kHz, lead to a ion velocity of ≈ 6 m/s. In the experiments of **section 3.4.2** with a laser cooled $^{40}Ca^{+}$ ion and a $^{24}Mg^{+}$ ion, the needed cooling rate, γ, along the z-axis was as low as $2\pi \times 100$ Hz when applying a strong radial cooling. To achieve this, the cooling laser was detuned approximately 10 transition linewidths away from resonance, that is $\delta \approx -10\Gamma$, where Γ is the cooling transition linewidth. Such a detuning can readily be applied and using the above relation we get a maximum velocity of $v_{\max} \approx 80$ m/s. Since this is much greater than the ion velocity, the frictional force approximation can be met readily.

For the results presented in **section 3.4.1**, however, the laser detuning was only 1-2 Γ, and so the frictional force approximation was fulfilled over only a part of the ion trajectory. But since the γ dependence of the amplitude is weak for $\gamma \ll \omega_z$, the measured oscillation frequency was essentially independent of the maximum amplitudes. Using a larger laser detuning, we expect the relative shift in the resonance frequencies due to the non-linear friction force to be smaller than 10^{-5}.

Yet another laser-cooling related effect exists for measurements with non-identical ions. An intensity imbalance of the counter propagating beams will

cause a constant force, which will push the laser-cooled ion away from its equilibrium position. Furthermore, such an imbalance will shift the mass-dependent trap frequency used in **equation (3.3)** [84]. If we (very conservatively) assume a 10% intensity imbalance, the relative frequency shift is at most 1×10^{-5} for the COM mode motion of a $^{40}Ca^{+}$ ion trapped together with an ion that is up to three times lighter or heavier and typical parameter of $\omega_1 = 2\pi \times 100$ kHz, $\gamma = 2\pi \times 100$ Hz, $\delta = -\Gamma$. For the BR mode, the shift is much higher but less than 4×10^{-4}. By minimizing the difference between the resonance frequencies for the two possible ion configurations (that is, with the laser-cooled ion located either to the left or to the right of the ion-trap center), the intensity imbalance effect can probably be reduced to a level of $< 10^{-6}$.

3.5.2 Non-linearity in the Coulomb interaction

In **section 3.3**, we assumed the oscillation amplitude to be small compared to the inter-ion equilibrium distance, such that the Coulomb interaction was well-described by a second order expansion. This was needed to arrive at the solutions in **equation (3.4)** and (**3.9**), but is obviously not always valid. In fact, for large changes in the ion–ion distance, additional terms in the Coulomb expansion are needed. They lead to an anharmonic interaction and cause the amplitude-dependent oscillation frequency behavior seen in **figure 3.6**.

In the simplest case, namely the COM mode excitation of identical ions, the ions move in the same direction and with the same amplitude, corresponding to a normalized eigenvector of $(1, 1)/2$ [79, 80] [see **equation (3.5)**]. Thus, the ion–ion distance is always equal to the equilibrium distance and the Coulomb interaction energy is then just a constant term in the potential and does not give rise to an amplitude-dependent oscillation frequency. Indeed, **figure 3.5** above shows that the oscillation frequency is independent of amplitude. For the BR mode, however, the ions move in opposite directions, corresponding to an eigenvector of $(1, -1)/2$, and the inter-ion separation is in general different from the equilibrium distance. Hence, the higher-order terms of the Coulomb expansion causes an amplitude dependent shift of the oscillation frequency, when the amplitudes amounts to a significant fraction of the equilibrium distance, as seen in **figure 3.6**.

In the case of different ions, the two coordinates of the eigenvector of the COM mode generally have a different magnitude. Thus, even for COM mode excitation, the inter-ion distance changes and higher-order terms of the Coulomb interaction give rise to amplitude-dependent shifts of the oscillation frequency. The mass dependence of the eigenvectors is given by **equation (3.5)**. In **figure 3.9**

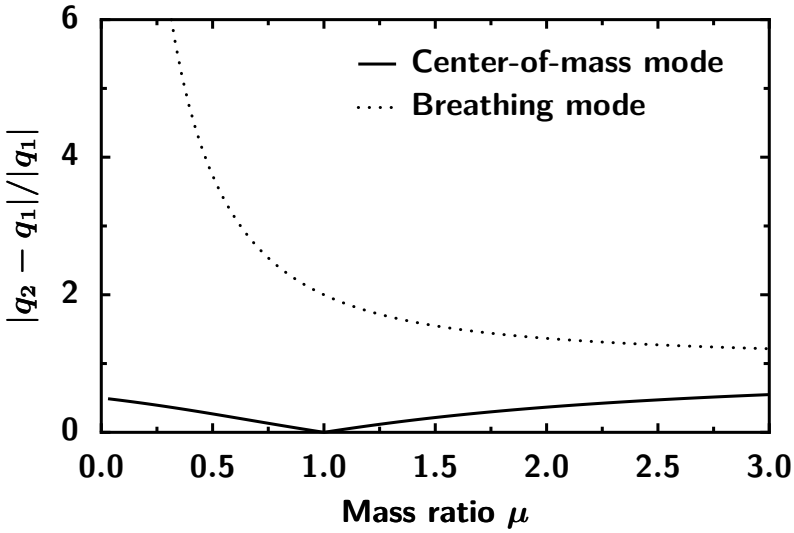

Figure 3.9 The ratio between the difference of the eigenvector coordinates and the amplitude of coordinate 1 for the laser-cooled ion as a function of mass ratio, μ. The larger relative difference for the breathing mode leads to a larger amplitude dependence of the oscillation frequency.

we plot the change in ion distance relative to the amplitude of observed laser-cooled ion as a function of the mass ratio μ for both the COM and BR modes, that is, we plot the quantity $|q_2 - q_1|/|q_1|$. Obviously, the change in ion distance is much smaller for the COM mode than for the BR mode and, consequently, the COM mode oscillation frequency is much less amplitude dependent than the BR mode frequency is. In the identical ion limit of $\mu \to 1$, the amplitude dependence vanishes completely for the COM mode.

Turning to real world numbers, the equilibrium distance, Δz, equals 26.0 μm for two $^{40}Ca^+$ ions in a harmonic potential with $\omega_z = 2\pi \times 100$ kHz, while typically applied amplitudes in the experiments described in **section 3.4** are about 5 μm. This implies that in our case, it is necessary to consider higher-order terms for the BR mode and, in some cases, also for the COM mode for two different ions. This effect could be reduced, but not eliminated, if much smaller amplitudes could be detected by using a state-of-the-art imaging system with almost diffraction-limited resolution of ≈ 1 μm; however, the cost of additional experimental complexity must be considered, since lenses will have to be mounted inside the vacuum chamber [88].

Because the resonance frequency depends non-linearly on the amplitude, the frequency dependence of the driven ion motion becomes non-linear. This effect

is seen most clearly in **figure 3.4** (b) and (d) and in **figure 3.6**. Following the amplitude from the low-frequency side in **figure 3.6**, the amplitude continues to rise even after the "true" small-amplitude resonance frequency has been passed. This behavior is an example of *frequency pulling* where the effective resonance frequency gets shifted to higher values due to the increased amplitude. Jumps between large and small amplitudes appear around the point where the drive frequency is so far from the small-amplitude resonance frequency that the driving force is able, only marginally, to sustain non-linear oscillations (see e.g. the dotted line in **figure 3.6**).

In **figure 3.6**, the small-amplitude BR mode resonance frequency is indicated by a dashed line. It is found on the low frequency side of the resonance structure and a "trained eye" may be able to estimate this frequency within ≈ 1 kHz from a series of scans with varied driving force, such as are presented in **figure 3.6**. For the COM mode excitation of systems of two different ions, such non-linear effects at 5 μm amplitude are not seen; only for very large amplitudes the effect of an amplitude-dependent oscillation frequency can be observed, as shown in **figure 3.7**.

To sum up, the BR mode oscillation frequency is strongly perturbed by higher-order terms in the Coulomb interaction at practically applied amplitudes of $\approx$ 5 μm, while the shift of the COM mode frequency is much smaller. Although the amplitude dependent shift in the BR mode excitation prevents very accurate mass measurements, a measurement of this frequency can be useful in some situations, as we will discuss further in **section 3.5.7**. For excitations of the COM mode with amplitudes around 5 μm, the relative shift in resonance frequency is typically 10^{-4} or less, and for ions of almost the same mass, the shift is particularly small.

3.5.3 Ion trap imperfections

Another assumption made in **section 3.3** was the perfect harmonic trapping potential. Unfortunately reality often deviates from the ideal case, so in this section we will take a look at various unavoidable effects that compromise this assumption. First, we consider higher order terms in the trapping potential due to non-ideal electrode shapes or small misalignment of the electrodes. Second, we take a look at imperfections in the trapping fields, e.g. when the ions move slightly off-axis or difficulties in controlling the electrode voltages. Finally, the effect of residual magnetic fields is discussed.

3.5.3.1 Anharmonicity

In reality, a harmonic term alone is not enough to describe the trapping field. Odd terms (z, z^3, etc.) arise when the symmetry of the trap is broken. This could be caused by small misalignments and imperfections of the electrodes, by surrounding conductive or dielectric elements or by contact potentials [89] due to deposited material on the electrodes. Higher order even terms (z^4, z^6, etc.) arise from non-ideally shaped electrodes, which are chosen for practical reasons.

The linear term, z, does not change the oscillation frequency, but only the ion equilibrium positions. Higher order terms, however, will change the oscillation frequency. To estimate the n*th* order effect, we integrate the equations of motion for two particles in a trapping potential of $\frac{1}{2}m\omega_{\pm}^2 z^2\left[1+\left(\frac{z}{z_0}\right)^{n-2}\right]$. The oscillation period is then determined from a Fourier transform of the trajectories. This has been done for $n = 3$ and $n = 4$, with z_0 set to half the length of the center electrodes (2.7 mm) and, for both cases, the relative oscillation frequency shift is less than 10^{-5} for amplitudes up to 5 μm and less than 10^{-4} for amplitudes up to 20 μm. Furthermore, the choice of z_0 is a worst-case scenario; higher order terms are significantly smaller and for appropriately chosen length of the center electrodes, the 4*th* order term disappears completely [84]. Thus, we expect anharmonic effects to cause a relative shift in oscillation frequency less than 10^{-5}.

Experimentally, this is supported by the results from **section 3.4.1**, where the COM mode of two $^{40}Ca^+$ was excited. Because the ions are identical, the nonlinearity of the Coulomb interaction does not alter the oscillation frequency, so an amplitude dependent shift must be attributed to either the laser cooling, as discussed in **section 3.5.1**, or the anharmonicity. In the mentioned experiment, the measured COM frequencies around 95.625 kHz differed by less than 20 Hz at amplitudes between 15 and 35 μm. Thus, we can ignore anharmonic effects, at least at the level of 2×10^{-4}. Anharmonicity of the trap should also give rise to frequency-pulling effects, but this was not observed.

3.5.3.2 Trapping field imperfections

So far, we have assumed that everything takes place along the z-axis and hence treated the motion of the ions in one dimension only. In reality, the trapping potential is harmonic in all three dimensions, $\frac{1}{2}m(\omega_x^2 + \omega_y^2 + \omega_z^2)$, and thus causes a total of six normal modes in the case of two ions [90]. Besides the already described COM and BR modes along the z-axis, there are also two purely radial modes and two mixed modes, that involve both radial and axial motion. At small

amplitudes, the modes are normal and can be treated separately. However, the trapping potential could contain terms which couple the axial and radial coordinates, e.g. xz or yz, leading to a change in the axial frequencies when the two ions are not confined to the z-axis. The ions are aligned on the z-axis by choosing trapping voltages such that $\omega_{x,y} > \omega_z$, but the finite ion temperature of ≈ 5 mK, is enough to move the ions up to 1 μm off-axis. The situation is worsen by radial heating of off-axis ions caused by micromotion, which can be transfered into the axial motion by coupling terms as well as mode mixing.

Another unwanted effect is spurious RF fields, that can lead to an additional confining potential along the ion-trap axis (for example, due to slightly different RF amplitudes on the 12 electrodes). The RF voltages can be matched to within one percent, by adjusting the individual capacitive loads of the electrodes (see **figure 3.2**), such that micromotion along the z-axis is minimal. In this case, $q_z = \frac{2neV}{m\Omega^2 z_0^2} \approx 0.004$ for a trapped $^{40}Ca^+$ ion with typically applied voltages of 400 V at $\Omega = 2\pi \times 4$ MHz. The corresponding secular frequency is $\omega_z^{\mathrm{RF}} = \frac{\Omega q_z}{\sqrt{8}} \approx 2\pi \times 6$ kHz which should be added in quadrature to the DC induced axial trap frequency to obtain the total axial trap frequency. Thus the relative shift is about 2×10^{-4} for axial frequencies around $2\pi \times 100$ kHz, where we normally operate. This small change of axial frequency will directly influence a mass measurement through **equation (3.4)**, but for ions with masses close to the laser-cooled ion mass, the relative error is correspondingly small, e.g. $\approx 10^{-4}$.

The last effect to be considered here, is drift of the DC voltage supply. Since the axial frequency depends directly on the end-cap voltage, U, through equations (**2.6**) and (**2.5**), the stability is obviously very important. From the data presented in **figure 3.11**, where the axial frequency was measured continuously for 15 minutes, we see a relative drift below 10^{-4} for our home-made DC supply. This slow drift is non-critical for many experiments, since a reference measurement can typically be made within a short time interval before or after the mass measurement.

3.5.3.3 Residual magnetic fields

Besides coupling terms in the trapping potential, residual magnetic fields with a component in the radial plane, will also couple the radial and axial motions of the ions. To estimate the effect of the cyclotron motion of the ion resonance frequencies, we consider the simple single ion situation. The equations of motions are:

$$\ddot{z} + \omega_z^2 z - \omega_c \dot{r} = 0 \tag{3.13}$$

$$\ddot{r} + \omega_r^2 r - \omega_c \dot{z} = 0 \tag{3.14}$$

with ω_z and ω_r being the axial and radial ion-trap oscillation frequencies, respectively, and with ω_c being the cyclotron frequency. If the cyclotron frequency is smaller than both the axial and radial trap frequencies, as well as the difference between these frequencies, that is, $\omega_c < \omega_z$ and $\omega_c < \omega_r$ and $\omega_c < |\omega_z - \omega_r|$, then the modified axial frequency ω_z' is given by

$$\omega_z' \approx \omega_z + \frac{1}{2}\frac{\omega_c^2}{\omega_z} \tag{3.15}$$

If for example the magnetic field of the Earth is not compensated for, the magnetic field of ≈ 1 G, leads to a cyclotron frequency of $\approx 2\pi \times 100$ Hz. Compared to the trap frequencies of $\approx 2\pi \times 100$ kHz, this causes relative frequency shifts of only 10^{-6}. Similar results can be found for $\omega_\pm$. In practice, the amplitude of the residual magnetic field can easily be reduced to 0.1 G, causing relative shifts less than 10^{-8}.

3.5.4 Ion loading

Loading of atomic ions into the trap may introduce two undesirable effects, namely contamination of the ion-trap electrodes by neutral atoms from the effusive atomic beam (see **section 2.3**) causing contact potentials [89] and charging of insulating parts close to the ion-trapping region through photoelectron emission due to stray UV light. We have investigated these effects by a series of single Ca^+ ion oscillation frequency measurements, where the UV beam and the atomic beam was blocked and unblocked by mechanical shutters respectively. The results can be seen in **figure 3.10**. In (left), the UV photoionization beam is permanently blocked while the atomic beam is blocked (white background) and unblocked (grey background), but no evidence of a systematic effect due to the atomic beam flux is observed. In (right), however, where the UV photoionization beam is blocked and unblocked while keeping the atomic beam blocked, a drastic effect is seen. After a rapid initial rise of the ion resonance frequency of more than a 100 Hz, the charging effect seems to reach a steady state after some time. The "problematic" UV light is probably either weak reflections from the exit window (in spite of its anti-reflection coating at 272 nm) or weak halo-like structures surrounding the main ionization beam. When the source is identified, its effect can probably be reduced dramatically by proper beam shaping and positioning.

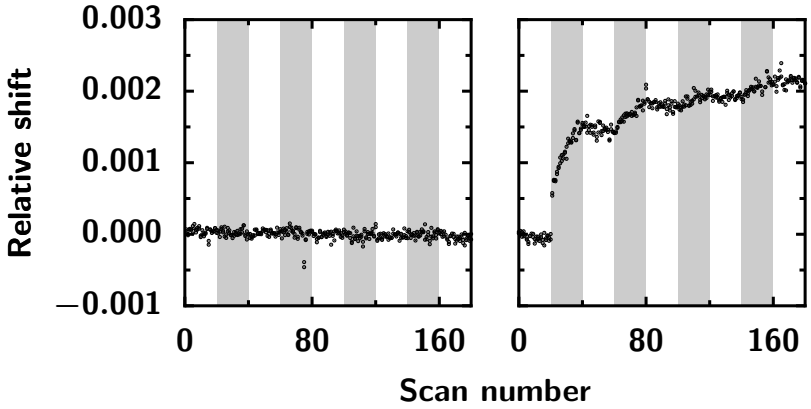

Figure 3.10 Relative shift of the measured ion-trap frequency in a series of scans for a single $^{40}Ca^{+}$ ion. For each scan, the shift is defined as $\omega/\omega_0 - 1$, where ω is the trap frequency measured in the scan and $\omega_0 = 2\pi \times 95.51kHz$ is the frequency measured in the first scan of part (left). (left) A series of scans where the neutral calcium beam is blocked (white background columns) and unblocked (gray background columns) sequentially. (right) Trap frequency measurements where the UV photoionization beam is blocked (white background columns) and unblocked (gray background columns) sequentially. The change of trap frequency when the UV beam is "on" is most likely due to charging of insulating parts near the ion-trap region.

This charging effect is not limited to calcium, but will most likely also be observed for other ions that could be used in SCSI-MS technique. Photoionization of berylium, magnesium and mercury requires UV light at 235, 285 and 185 nm, respectively, while laser cooling of said ions involve UV light at 313, 280 and 194 nm. In the special case of calcium, photoionization could be realized by two lasers at the wavelengths 423 nm and 390 nm [91], which would probably reduce the problem significantly. A more general, but also more complex, solution would be to use an ion-trap with multiple tapping zones, e.g. a "loading" zone and an "experimental" zone [92].

3.5.5 Background gas

Background gas is present at all times, either just residual gas or reactant gas used in reaction studies. This gas manifests itself by ion-neutral collisions between the cold atomic and molecular ions, which in some cases leaves the ions with sufficient kinetic energy to move away from ion-trap axis. In the recorded images, this is observed as a sudden disappearance of fluorescence. The trap depth is, however, ≈ 1 eV deep and the ion is typically not expelled from the pseudo-potential,

but rather re-aligned once again on the z-axis due to the continuous laser-cooling; i.e. the fluorescence resumes after some time.

The frequency of these events depends of course on the gas pressure. In our setup we operate with a base pressure of $\approx 10^{-10}$ mbar, which only causes collisions once in several minutes. In reaction studies, where we typically apply a gas pressure of up to $10^{-9} - 10^{-8}$ mbar to get convenient reaction rates, this occurs more often, but frequency scans are still possible in spite of these ion-heating events. At much higher pressure, however, the analysis of the recorded images becomes unfeasible due to the amount of images with "hot" ions.

It can also be speculated whether close or distant collisions may introduce an additional damping effect, shifting the resonance frequency. This does not seem to be the case, since no shift has been observed when measuring the oscillation frequency of two $^{40}Ca^+$ ions at pressures up to 10 times higher than the base pressure.

Finally, we have investigated a more indirect effect from the introduction of reactant gas, namely contact potentials caused by contamination of ion-trap electrodes. Leaking in O_2 gas at pressure of $\approx 10^{-7}$ mbar for a few minutes caused the COM mode frequency of two $^{40}Ca^+$ ions to shift at the level of 1×10^{-4}. Between the measurements, however, new ions were loaded, so this shift may as well be attributed to the loading procedure described in **section 3.5.4**.

3.5.6 Photon detection

In the following two subsections, we will discuss the limitations imposed by the imaging system. First we take a look at the spatial resolution, which is important because we want to monitor small motional energy excitations. After that, the achievable signal-to-noise ratio is analyzed with a view to estimating the uncertainty on the frequency determination.

3.5.6.1 Spatial resolution

The total resolution of our setup is limited by the spatial resolution of the imaging system itself (see **section 2.5**) as well as the finite ion temperature that results in the ions moving around. These ion excursions scale as ω_z^{-1} for a fixed temperature and from a simple experimental point of view, ω_z should be chosen such that the thermal excursions of the ion are roughly the same size as the spot size resolution of the imaging system. In this way, better image resolution allows for a higher trap frequency and thus a more precise oscillation frequency measurement, since

the resonance is narrower. However, for a particular experimental arrangement, the effect of the non-linearity in the Coulomb interaction (see **section 3.5.2**) must be taken into account when choosing ω_z.

The ion displacements of a $^{40}Ca^+$ ion is less than 2 μm at a temperature of 5 mK and an ion-trap frequency of $2\pi \times 100$ kHz, while the spot size resolution of our imaging system is about 3 μm HWHM.

3.5.6.2 Scattering rate and collection efficiency

The resonance frequencies are determined from projections of the pixel values onto the z-axis as seen in **figure 3.3**. A set of these projections taken at different drive frequencies is visualized as grey scale contour plots in **figure 3.4** (a to d). These z-projected pixel values are the signal, S, we analyze and they are directly related to the number of collected photons, which is proportional to the photon scattering rate, the collection efficiency and the CCD exposure time, which we denote T_{exp}. The precision at which the resonance frequencies can be determined are limited by the signal-to-noise ratio, S/N, that is, the signal divided by the standard deviation. To determine ω_+ with a precision of $\Delta\omega$, the uncertainty of the measured amplitude must be less than the variation of the amplitude over the frequency interval $\Delta\omega$, as plotted in **figure 3.4** (e to h). In both the phase and the amplitude method, the uncertainty on the amplitude, A, is of the order of $A/(S/N)$, but since the phase method features a drastic zero-crossing, this requirement is more easily met, than for the amplitude method.

In a bit more detail, the variation of the amplitude over $\Delta\omega$ in the phase method is given by $\Delta\omega$ times the slope of the signal, which is given by $\approx A_0/\gamma$, where A_0 is the maximal amplitude and γ is the damping due to the Doppler cooling. Hence $\Delta\omega \approx \gamma/(S_g/N_g) \propto T_{\text{exp}}^{-1}$, where the subscript '$g$' indicates the signal-to-noise ratio when the image intensifier is gated. Likewise for the amplitude method, where the variation of the amplitude over $\Delta\omega$ is given by $\Delta\omega^2$ times the curvature, $\approx A_0/\gamma^2$, from which it follows that $\Delta\omega \approx \gamma/\sqrt{S/N} \propto T_{\text{exp}}^{-1/2}$.

The running average and the corresponding statistical uncertainty for a series of measurements of the COM mode frequency for two $^{40}Ca^+$ ions are shown in **figure 3.11** (a) and (b) for the amplitude method and the phase method respectively. The statistical uncertainty of ≈ 2 Hz is in reasonable agreement with the above estimates of $\Delta\omega$. The limiting value is reached with fewer phase-method measurements than amplitude-method measurements, but in approximately the same measurement time, since the amplitude method scans are approximately five times faster than the phase method scans.

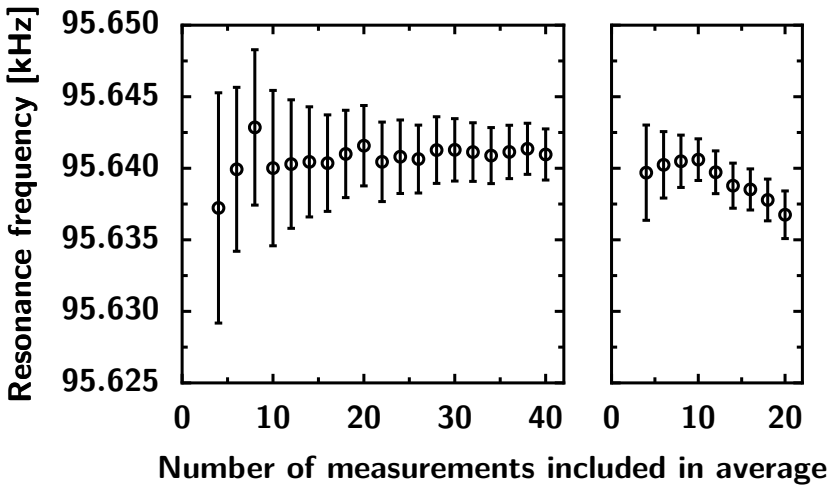

Figure 3.11 Running average and statistical uncertainties of the COM mode frequency for two $^{40}Ca^{+}$ ions obtained with the amplitude method (left) and with the phase method (right). For the amplitude method, the CCD exposure time was 100 ms and $S/N \approx 17$, while for the phase method the exposure time was 500 ms and $S_g/N_g \approx 6$. γ is $2\pi \times 113$ Hz in both cases, yielding $\Delta\omega \approx 2\pi \times 27$ Hz for the amplitude method and $\Delta\omega$ is $\approx 2\pi \times 19$ Hz for the phase method. These values are in reasonable agreement with the statistical uncertainty of about $2\pi \times 7$ Hz for both methods. The total measurement times for the amplitude measurements and the phase measurements were 13 minutes and 23 minutes, respectively.

While deriving the estimates of $\Delta\omega$, we tacitly assumed that the width of the resonance was given by γ alone, which is indeed the case in our experiment.. If, however, the inverse exposure time is of the order of γ or smaller, the width of the resonance has an additional contribution. In the extreme case of $\gamma \ll 1/T_{\mathrm{exp}}$, it is found that $\Delta\omega \propto T_{\mathrm{exp}}^{-3/2}$ for the amplitude method and $\Delta\omega \propto T_{\mathrm{exp}}^{-2}$ for the phase method.

3.5.7 Reference measurements

As described in **section 3.3**, the mass of an unknown ion can be determined from measurements of either the COM mode frequency and a reference frequency ω_1, or from measurements of both the COM mode frequency, ω_+, and the BR mode frequency, ω_-, by using **equation (3.4)**. Which set of frequencies to use depends on the specific use of the SCSI-MS technique, as well as the uncertainty on the mass derived from the frequency measurements.

In **chapter 5** we describe a reaction experiment where two laser-cooled ions are trapped and one of them reacts to form an unknown molecular ion. In this

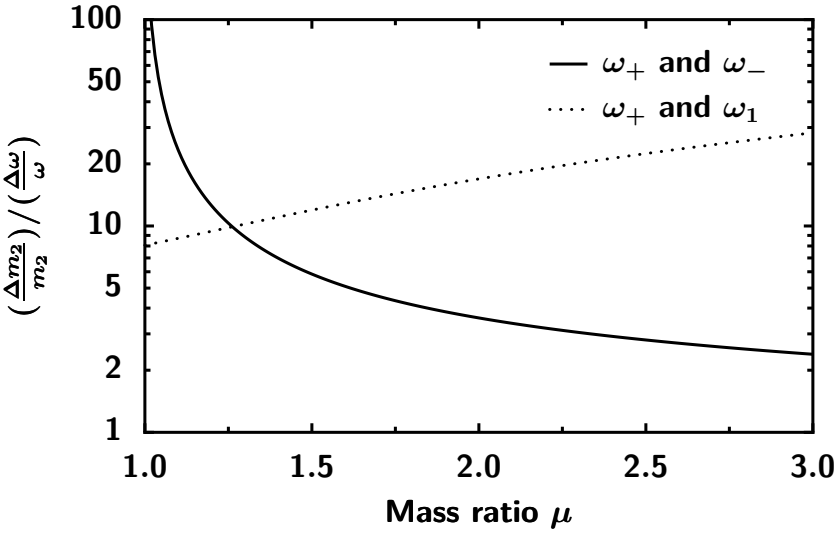

Figure 3.12 The ratio between the relative uncertainty on the unknown ion mass and the relative uncertainty of the frequency measurement ($\Delta\omega/\omega = \Delta\omega_1/\omega_1 = \Delta\omega_+/\omega_+ = \Delta\omega_-/\omega_-$) as a function of mass ratio μ. The two curves represent only COM mode measurements (One reference measurement of ω_1 and one measurement of ω_+) and combined COM and BR mode measurements, respectively.

case a reference measurement of ω_1 can be made sequentially again and again with the two laser-cooled ions until a reaction occurs. Because ω_1 is measured shortly before ω_+, a slow drift in ω_1 due to for example a changing DC voltage, has negligible influence. Similarly, in experiments where a single laser-cooled ion is trapped and a second unknown ion is loaded, e.g. a fragment of a complex molecular ion as in **chapter 4** [40] or a super-heavy ion species [93, 94, 95], a reference measurement of ω_1 can be made with the single ion prior to the loading event.

Slow drift of the DC voltage could become an issue in longer reaction sequences as, for example in bi-molecular reactions as described in Ref. [96], or photoreactions as described in **chapter 4**, or a combination thereof, where it would compromise the mass measurements for the different reaction steps. If the drift is linear, it can of course be corrected by measuring the reference frequency both before and after the reaction sequence, provided that the necessary loading of a reference ion after the reaction sequence does not give rise to significant shifts of the ion-trap frequency.

The problem of DC drift can be completely eliminated by measuring the COM and BR mode frequencies, since these can always be measured within a

short time interval. However, the uncertainty in the BR mode frequency determination due to the strong amplitude dependence cause a reduced precision on the mass measurement. In combination, the two measurements should enable accurate mass measurements over long time scales even in the presence of a small drift of the ion-trap frequency.

Another advantage of the self-referenced measurement of ω_+ and ω_- over the mass determination from ω_1 and ω_+, is that it is unaffected by any additional potential induced by a RF field along the ion trap axis as described in **section 3.5.3.2**.

The uncertainties on the measured frequencies, either ω_1 and ω_+ or ω_+ and ω_-, translate to an uncertainty on the mass m_2 of the unknown ion determined from **equation (3.4)**. The relative uncertainty depends on the chosen reference measurement as well as the mass ratio μ, as shown in **figure 3.12**. For a mass ratio larger than 1.25, it appears to be advantageous to determine the mass from ω_+ and ω_-, however, the difficulties in making a precise determination of ω_- are sufficiently severe that a mass measurement based on ω_1 and ω_+ is generally preferable, provided that error sources, which are more severe for mass measurements based on ω_1 and ω_+, for example, drift of the ion-trap frequency and RF-induced secular potentials, are sufficiently small.

3.5.8 Choice of parameters

In light of the previous subsections, we here summarise the choices that has to be made when using SCSI-MS.

To reduce the amplitude dependent frequency shift as much as possible, it is advantageous to measure small amplitudes for both the COM mode and the BR mode. The cooling force along the z-axis should be kept weak, such that the broadening due to the damping term is small. At the same time, a strong radial cooling force is beneficial, since it keeps the ions cold and aligned, while ensuring a good signal-to-noise ratio in the images. In the optimal setup, the detunings of the axial and radial cooling beams should be independent, but as we have seen, individual control of the beam intensities at a fixed detuning can be a satisfactory compromise.

The frequency of the ion trap plays several roles. On one hand a high relative precision ($\omega_\pm/\Delta\omega$) and a small ion spot width requires a large ion-trap frequency; on the other hand amplitude-dependent frequency shifts are reduced for a large equilibrium ion distance, that is, for a small trap frequency. With our relatively poor image resolution of ≈ 3 μm FWHM, a trap frequencies of $\omega_\pm \approx 2\pi\times 100$ kHz

and $\gamma \approx 2\pi \times 100$ Hz is a convenient set of parameters that enables accurate mass determination at the level of 10^{-4}.

Both the amplitude method and the phase method has advantages and disadvantages. As discussed in **section 3.5.6**, the phase method enables more accurate frequency determinations due to the sharp zero crossing, but at the cost of increased measurement time. The amplitude method is much faster, but the profile of the amplitude is not so sharp. With the present error sources at the 10^{-4} level, the amplitude method is superior due to the shorter measurement time, but ultimately the phase method would be the most accurate.

3.6 Conclusion

In this chapter, we have presented a mass spectrometric technique that relies on the measurement of the normal mode frequencies of strongly-coupled two-ion systems. The strongly-coupled regime is reached by sympathetic cooling of the ion of interest (the unknown ion) through the Coulomb interaction with a simultaneously-trapped and laser-cooled atomic ion.

Even without optimizing our current setup for SCSI-MS, we have obtained a relative mass resolution of $\approx 10^{-4}$ (see **section 3.4**). Based on the discussion in **section 3.5** of the various effects that can limit the mass resolution, there seems to be room for improvement in the measurement accuracy by a factor of 10-100 and, hence, mass measurement with an accuracy of $\frac{\Delta m}{m} \approx 10^{-5} - 10^{-6}$ should be within reach. In this respect, the main error sources to be minimized are charging effects during loading of ions (**section 3.5.4**) and imperfections in the RF-field configuration (see **section 3.5.3.2**). By a modest optimization of our current experimental arrangement, we expect to be able to achieve a relative mass measurement accuracy of $< 10^{-4}$, and thus be able to discriminate between various mass doublets (for example, $^{24}MgH^+$ and $^{25}Mg^+$).

The technique is inherently a single ion mass spectrometric technique, utilizing a non-destructive detection step. This latter feature of the SCSI-MS technique is suitable particularly for monitoring mass changes by, for example, either photofragmentation, as we will see in **chapter 4**, or multiple-step reactions. The single ion aspect of such studies enables one not only to obtain an ensemble-averaged result, but presents the opportunity for comparing individual ion "histories". In particular, in experiments that involve complex molecular ions with complex internal structures, such individual ion "histories" may be essential for the identification of important processes.

As mentioned briefly also in **section 3.5.7**, the SCSI-MS technique may possibly find applications in the studies involving exotic ions, such as super- heavy element ions [93] or rare isotope elements, because the technique can lead to quantitative results using only a relative small number of ions as is illustrated in **chapter 5**.

Chapter 4

Consecutive photodissociation of a single complex molecular ion

Photodissociation of molecules is a process of utmost importance. In nature it plays and important role for the physics and chemistry of, e.g., planetary atmospheres [97] and interstellar clouds [98].

In the laboratory photodissociation is a versatile tool which is used to probe molecular structure and dynamics [99], but also as a pathway to create otherwise not easily accessible neutral molecules [100, 101] in the gas phase, as well as, some specific molecular anions [102] and various positively charged radicals [103]

Charged photofragments can generally both be identified and counted by the use of different types of mass spectrometers ranging from time-of-flight (TOF) [74, 76], quadrupole [74, 75] to cyclotrons [77, 104]. If, however, the molecular ion disintegrate inso smaller fragments through a series of consecutive dissociation steps when exposed to light, the individual steps in the photodissociation chains are difficult to identify with the use of the above mass spectrometers, since experiments typically involve larger ensembels of ions [105, 106]. This problem is non-existent if it is possible to work with a single ion at a time and determine its composition in a non-destructive measurement.

4.1 Application of SCSI-MS to consecutive photodissociations

In **chapter 3**, we saw how a single molecular ion trapped and sympathetically cooled by a laser-cooled atomic ion, could be identified by exciting the center-of-mass (COM) mode of the two-ion system. Since the SCSI-MS technique is non-destructive, it can be applied repeatedly to follow changes in the molecular ion mass, thus allowing detailed studies of the time evolution of light-induced consecutive fragmentation at time scales from milliseconds up to several hours. The temporal accuracy is currently limited to 0.1 s by the fluorescence light collection efficiency of the imaging lens system, but the technique can rather simply be improved to become an order of magnitude faster. Another interesting feature of live monitoring of the molecular ion mass is that it facilitates a viable way of probabilistically preparing a wealth of single molecular ions through consecutive fragmentations, by simply blocking the dissociation light when the desired fragment is produced.

In this chapter we use the aniline ion as our guinea pig and show how the sequential breakage into lighter fragments caused by irradiation of a combination of CW light at 397 nm and nanosecond pulsed light at 294 nm, can be monitored

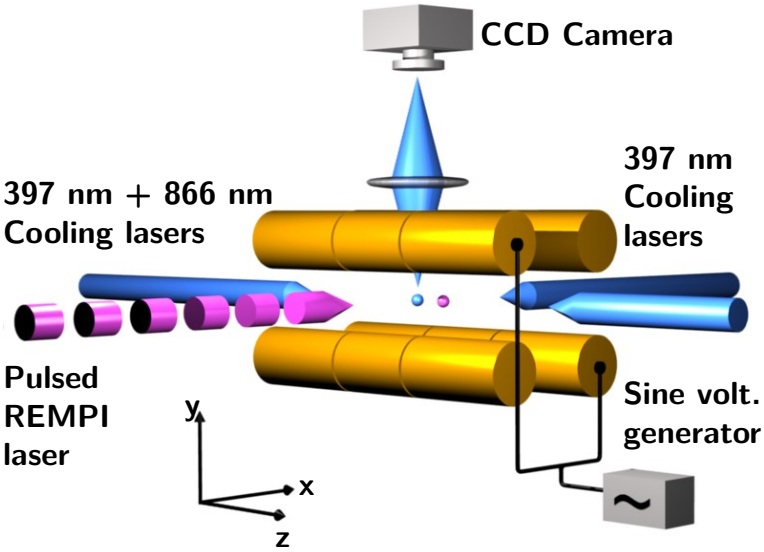

Figure 4.1 Sketch of the experimental setup. Seen in the sketch is the linear Paul trap, three cooling laser beams, a pulsed REMPI beam, the CCD camera and the modulation voltage generator.

non-destructively on time scales up to several minutes. Among the variety of ions produced and identified, the lightest species, robust against further photodissociation, is found to be c-$C_3H_3^+$ (cyclopropenylium).

4.2 Experimental procedure

Apart from a pulsed UV laser beam crossing the center of the trapping region orthogonal to the trap axis (see **figure 4.1**), the experimental setup was already described in **chapter 2** and **3**. This pulsed laser is used for resonance-enhanced two-photon ionization (R2PI) of aniline via the $S_0 \rightarrow S_1\, 0_0^0$ transition near 294 nm [107]. The pulsed UV laser beam (20 Hz repetition rate, 5 ns FWHM pulse length, peak intensity of 10^7 W/cm^2) is generated by frequency doubling of the output from a Nd:YAG[1] pumped Lambda Physik Scanmate 2 dye laser by an external KDP crystal. After traveling $\approx$ 30 m to the trap, the laser beam is focused to a spot size of $\approx$ 100 μm in the center of the trap. Since the laser is only used for loading of single ions, the pointing stability is not problem.

[1] Spectra Phsics, Quanta Ray Pro 270-20

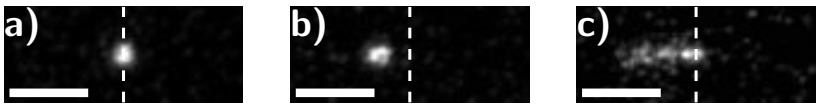

Figure 4.2 CCD images of a laser-cooled $^{40}Ca^+$ ion. (a) A single $^{40}Ca^+$ ion is trapped. (b) One $^{40}Ca^+$ ion and one non-fluorescing molecular ion. Notice the displacement of the $^{40}Ca^+$ ion due to the Coulomb interaction between the two trapped ions. (c) As (b), but with the center-of-mass mode of the two-ion system resonantly excited. The fluorescence from the $^{40}Ca^+$ ion appears axially smeared out due to the long CCD exposure time. The white scale bar in all three images corresponds to 25 μm.

The experiment proceeds as follows. First a single $^{40}Ca^+$ ion is loaded into the trap and laser-cooled as described in **section 2.3** and **2.4** [see **figure 4.2** (a)]. Next, a gas of aniline is leaked into the vacuum chamber at a pressure of $\approx 10^{-9}$ mbar which is about an order of magnitude higher than the background pressure in the trap region. Then a single aniline ion is produced through resonance-enhanced two-photon ionization (R2PI) via the $S_0 \rightarrow S_1\, 0_0^0$ transition by applying the pulsed laser.

After $\approx$ 10 s of sympathetic cooling, the non-fluorescing molecular ion becomes part of a two-ion Coulomb crystal. Due to a larger mass difference between the laser-cooled atomic ion and the sympathetically cooled molecular ion, this cooling period is considerably longer than the tens of milliseconds required to cool the MgH^+ and MgD^+ ions in **chapter 5**. That indeed a single ion is loaded is observed indirectly through the change in the position of the fluorescing $^{40}Ca^+$ ion in the camera images [see **figure 4.2** (b)]. At this stage, the 294 nm photoionizing laser is shut off, but the cooling laser beams remain present. A repeated series of non-destructive mass-scans is initiated around the masses expected to be produced in photodissociation of the positively charged aniline ion by the pulsed ionization light (294 nm) or the continuously present cooling light (397 nm). In **figure 4.2** (c), one clearly observes how the resonantly excited motion of the two-ion system results in an axial smearing of the fluorescence from the $^{40}Ca^+$ ion on the CCD camera when it is exposed for 100 ms. As discussed in detail in **chapter 3**, the mass of the non-fluorescent ion can now be deduced from the measured resonance frequency.

4.3 Photodissociation of aniline and its fragments

As mentioned in the previous section, aniline ions are produced through a R2PI process, a technique which has previously been applied successfully to aniline using light in the same wavelength range as here [108, 109, 110]. However, due

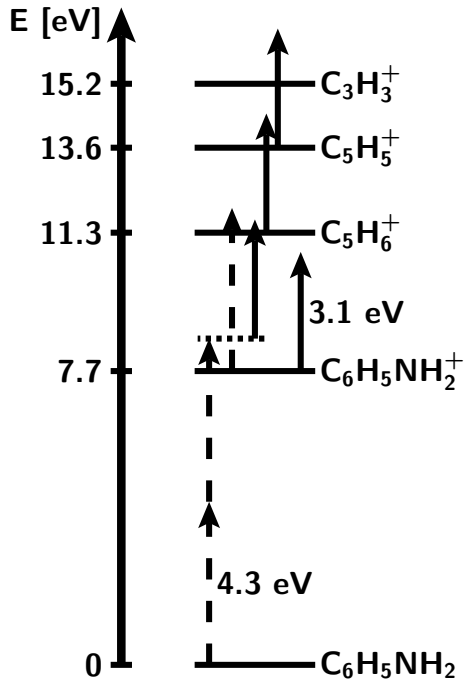

Figure 4.3 Energy level scheme with indication of the ground state energies of several relevant molecular ions relative to the ground state of neutral aniline. The dashed (solid) arrows indicate some of the photodissociation paths observed in the experiments due to the presence of light at 294 nm (397 nm). The lengths of the arrows correspond to photon energies.

to the relatively long period between when an aniline ion is formed until it is sympathetically cooled and "detected" in our images, the ion is actually exposed to ≈ 200 pulses after the formation. In **figure 4.3** the ground state energies of the most abundant photofragments in the experiments are plotted together with the indication of possible single (two) photon dissociation (ionization) processes and it is evident that these addiational pulses of 294 nm laser light (dashed arrows) can lead to formation of a $C_5H_6^+$ or a lighter mass ion through dissociation even when the $C_6H_5NH_2^+$ ion is formed in the vibrational ground state.

From previously reported photoionization experiments we expect that the probability of photofragmentation should be a few percent per pulse with the ≈ 10^7 W/cm^2 peak intensity of the 294 nm pulses [110, 111]. Furthermore, the $C_6H_5NH_2^+$ ion is not necessarily left in the vibrational ground state when produced through R2PI using light at 294 nm. Indeed, supplementing measurements

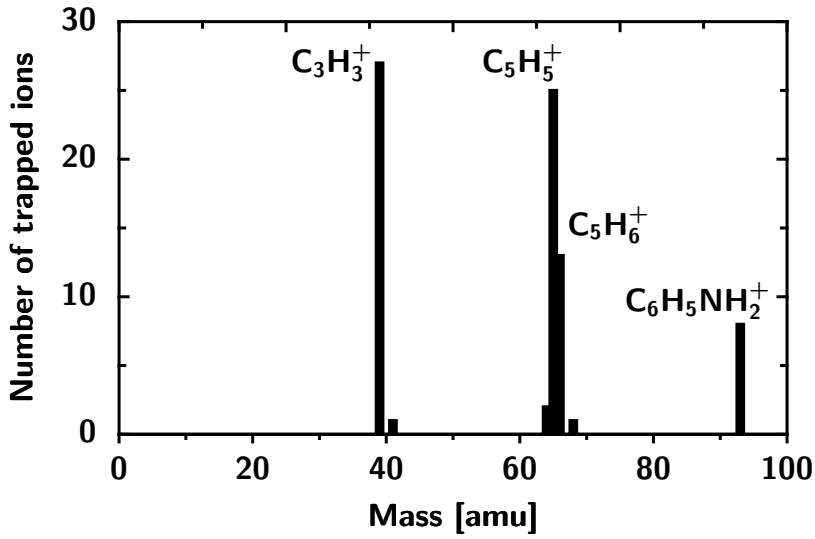

Figure 4.4 Molecular ion mass spectrum. The height of the bars indicates how often a specific ion mass was detected in a series of experiments.

of the R2PI process, employing photoelectron spectroscopy and a supersonic molecular beam, showed that with the same pulsed laser tuned to 294 nm, more than 60% of the ions will be produced in a vibrational state from where formation of a $C_5H_6^+$ ion is energetically allowed through absorption of a single 397 nm photon [112]. For a room temperature aniline gas as used in the present trap experiments, the fraction of vibrationally excited $C_6H_5NH_2^+$ ions may be even higher. A $C_6H_5NH_2^+$ ion formed in the ground state can, however, not be dissociated by a single 397 nm photon.

4.3.1 Aniline massspectrum

In **figure 4.4**, a plot of the frequency at which a specific molecular ion mass has been detected during a series of 77 "loading" experiments. In view of the previous discussion of the dissociation channels, the very low amount of $C_6H_5NH_2^+$ ions in this mass spectrum compared to previous experiments [108, 109, 110], is hardly surprising. As discussed above, most $C_6H_5NH_2^+$ ions are simply dissociatied by absorption of a photon from either the 397 nm beams or from the 294 nm beam before the latter is turned off.

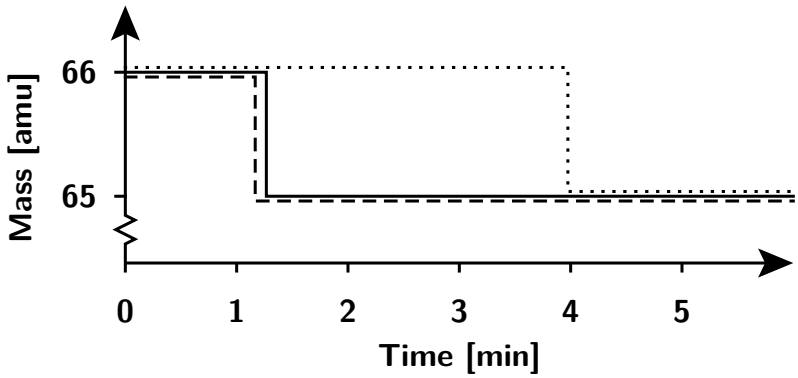

Figure 4.5 Three recorded time sequences of the photodissociation of $C_5H_6^+$ by a single 397 nm photon.

4.3.2 Consecutive photofragmentations

After the initial loading, and possible dissociation, we keep scanning across different mass resonances repeatedly. At this stage only the 397 nm light is present, but as is evident from **figure 4.3**, dissociation of vibrational excited $C_6H_5NH_2^+$, $C_5H_6^+$ and $C_5H_5^+$ is energetically allowed by absorption of a single photon. In **figure 4.5** examples of observed single-step photodissoiation of $C_5H_6^+$ are presented, but consecutive photofragmentations are also possible. For example in **figure 4.6**, an event where the three ions $C_5H_6^+$, $C_5H_5^+$ and $C_3H_3^+$ were consecutively produced from the parent aniline ion is presented. Sometimes a $C_3H_3^+$ ion was detected directly after a $C_5H_6^+$ ion, but it may be that in such experiments, a $C_5H_5^+$ was formed but not detected before further dissociation. Yet in other experiments single $C_5H_6^+$ or $C_5H_5^+$ ions have been observed to be rather stable against photodissociation by 397 nm light (lifetime: > 100 s). In some rare cases we do observe a single $C_6H_5NH_2^+$ ion surviving not only the initial ionization and sympathetic cooling phase (≈ 10 s) but also a very long time interval (> 100 s) with the 397 nm CW light present.

4.3.3 Determination of the $C_3H_3^+$ structure

The most stable photofragment ion produced is the $C_3H_3^+$ ion which was never observed to photodissociate due to the 397 nm light over timescales of ≈ 1000 s. The $C_3H_3^+$ ion is known to exist in two possible low-energy isomers: The ground state cyclic molecule, cyclopropenylium, and a much more reactive and slightly excited linear molecule, propagylium [113]. In order to determine if the structure

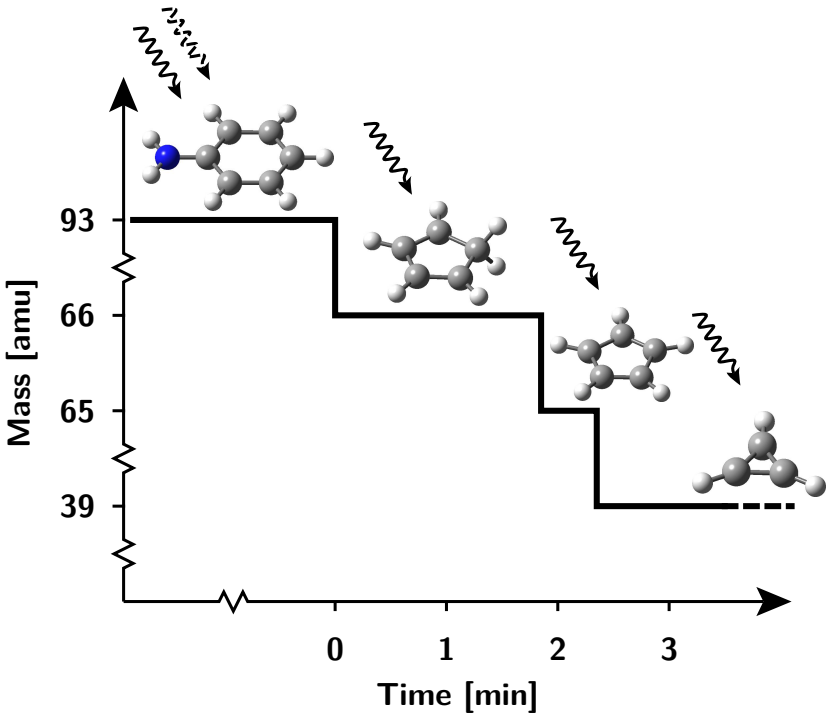

Figure 4.6 A consecutive photodissociation sequence observed in an experiment. The dashed (solid) wriggly arrows represent 294 nm (397 nm) photons responsible for the fragmentations.

of $C_3H_3^+$ is either "linear" or cyclic, we performed a series of experiments where the $C_3H_3^+$ ions were exposed to $C_2D_2^+$ molecules at a partial pressure of $\approx 1.3 \times 10^{-8}$ mbar.

$$\begin{aligned} C_3H_3^+ + C_2D_2 &\rightarrow C_3H_2D^+ + C_2HD \qquad (a) \\ &\rightarrow C_3HD_2^+ + C_2H_2 \qquad (b) \end{aligned}$$

The "linear" configuration has a high cross section for substitution reactions leading to the formation of $C_3H_2D^+$ or $C_3HD_2^+$ [114]. Since none of these ions were detected in a total reaction time of $\approx$ 5000 s distributed over 10 trials, we conclude that essentially only the cyclic c-$C_3H_3^+$ ions are formed.

4.4 Conclusion

In conclusion, we have seen that from a vapor of neutral aniline, any of the ions $C_6H_5NH_2^+$, $C_5H_6^+$, $C_5H_5^+$ and c-$C_3H_3^+$ can be prepared in a probabilistic but certain way. These ions could serve as a starting point for reaction studies of relevance to for example astrochemistry [115, 116] and soot production [117]. In both cases $C_3H_3^+$ is a step towards the production of bigger carbon chains.

A wealth of different ions could be prepared in a similar fashion, and because of the open experimental arrangement, many different light sources could be implemented, e.g., lasers, free electron lasers and synchrotron radiation. To circumvent the problem of photofragmentation by the laser cooling light, one would either have to spatially address only the atomic coolant ion by, e.g., introducing a single tightly focused cooling laser beam propagating at a 45 $^\circ$ angle with respect to the trap axis or alternatively apply a laser cooling scheme involving only red and infrared light as recently demonstrated [118].

We have also demonstrated how the non-destructiveness of the SCSI-MS technique allow us to study very slow photofragmentation processes under continuous light exposure and to investigate step-wise photodissociation of molecular ions when exposed to a series of laser pulses. Complementary, one could imagine how the SCSI-MS technique could be used to monitor the build-up of complex molecules through consecutive reaction processes.

Chapter 5

Probing Isotope Effects in Chemical Reactions Using Single Ions

The outcome of chemical reactions is often influenced by isotope effects. This is clearly observed in the chemical composition of interstellar clouds [119], as well as in laboratory experiments. Already when the first chemical lasers were developed, isotope effects was studied in order to understand the population inversion mechanism and to identify the laser transitions [120, 121]. In that case it was substitution reactions of the type F + HD and Cl + HD that was studied. These studies together with studies of the F + D_2 reaction strongly stimulated the whole field of reactive scattering [122]. Especially the resonance effects observed in the F + H_2 reaction and isotopic analogs [123] have been subject to numerous experimental and theoretical studies finally resulting in a much improved understanding of this benchmark reaction [122, 124].

In another series of experiments, reactions between a beam of ground state atomic ions and H_2, HD and D_2 have been studied. Strong isotope effects have been observed and, e.g., in reactions between alkaline earth ions (X^+) and HD, it was found that XD^+ formation is preferred for some alkaline earth ions, while XH^+ formation is preferred for others [125, 126].

Within the last few years, new techniques have emerged for ion-neutral reaction studies, e.g., of cold reactive collisions [42], single ion reactions [37] as well as reaction dynamics by applying crossed molecular beam imaging [34]. These techniques open up new possibilities in the field of ion-neutral reactive scattering.

5.1 Reaction between Mg^+ ions and molecular hydrogen

In this chapter, we investigate isotope effects in reactions of single $^{26}Mg^+$ ions with the isotopologues of molecular hydrogen, a model system for ion–neutral reactions. More precisely, we consider reactions at thermal energies with Mg^+ in the $3p\,^2P_{3/2}$ excited state (excitation energy of 4.4 eV). Because of the simple internal structure of the reaction partners, the studied reactions represent a simple test case for reaction dynamics on an excited potential-energy surface.

To probe the outcome of the reaction, we use the SCSI-MS technique described in **chapter 3**. With an efficiency of almost 100% in detecting reaction events, only about 250 reactions is needed to determine the branching ratio between the reactions

$$\begin{aligned} Mg^+(3p\,^2P_{3/2}) + HD &\rightarrow MgD^+ + H \qquad (a) \\ &\rightarrow MgH^+ + D \qquad (b) \end{aligned}$$

which was found to be larger than 5 in favor of MgD^+ formation.

From further 70 experiments involving other molecular hydrogen isotopologues,

$$\begin{aligned} Mg^+(3p\,^2P_{3/2}) + H_2 &\rightarrow MgH^+ + H \qquad (c) \\ Mg^+(3p\,^2P_{3/2}) + D_2 &\rightarrow MgD^+ + D \qquad (d) \end{aligned}$$

the probability of forming a molecular ion from an intermediate reaction complex (MgH_2^+, $MgHD^+$ or MgD_2^+) have been found to be equally likely.

5.2 Experimental procedure

Throughout the experiment HD, H_2 or D_2 gas is leaked into the trap chamber such that a steady-state pressure of about 1.3×10^{-9} mbar is reached. Two $^{26}Mg^+$ ions are loaded into the trap and laser cooled as described in **section 2.4**. Reactions between $^{26}Mg^+$ ions in the $3s$ ground state and thermally excited hydrogen molecules is not energetically allowed, so reactions exclusively take place with $^{26}Mg^+$ ions exited to the $3p\,^2P_{3/2}$ state in the laser cooling process [35]. The reaction product stays trapped, since the acquired kinetic energy is much lower than the trap depth of about 1 eV. Within tens of milliseconds, the formed molecular ion is sympathetically cooled through the Coulomb interaction with the remaining laser cooled $^{26}Mg^+$ ion and a two-ion Coulomb crystal is formed. Although the molecular ion does not emit light, its presence is evident from the fact that the remaining laser cooled $^{26}Mg^+$ ion is located at one of the two initial $^{26}Mg^+$ ion positions (see **figure 5.1**). As described in detail in **chapter 3**, the mass of the molecular ion species can now be determined by applying the SCSI-MS technique. In this study we excite the center-of-mass (COM) mode of the cold two ion system, but since we do not need the high precision of **chapter 3** to differ between mass 26, 27 and 28, we do not trace out the complete amplitude versus drive frequency graph. As is evident from **figure 5.1**, the excitation is easily observed by the eye, as a smearing out of the fluorescence light from the $^{26}Mg^+$ ion, when the parameters are chosen wisely (modulation voltage, laser cooling friction, exposure time, etc.) The smearing along the z-axis is due to the long exposure time (100 ms) compared to the COM mode oscillation period (typically 10 μs).

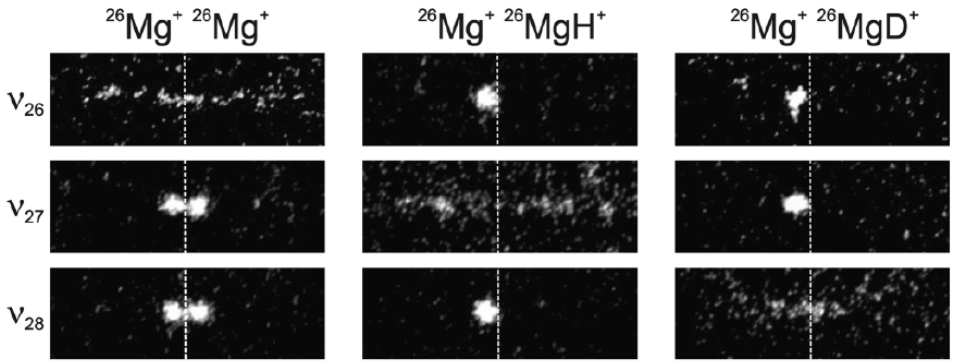

Figure 5.1 CCD images of two-ion Coulomb crystals with modulation applied at ν_{26}, ν_{27}, and ν_{28} for identification of $^{26}MgH^+$ and $^{26}MgD^+$ ions. The dashed vertical lines indicate the position of the trap center along the z-axis.

To allow for small drifts during the experiment, the frequency synthesizer described in **section 3.2.1** steps through a 100 Hz narrow frequency interval around ν_m, where ν_m is the COM mode eigenfrequency for on $^{26}Mg^+$ and one singly charged ion of mass m, and at each step a CCD image is recorded. Such images are shown in **figure 5.1** for one $^{26}Mg^+$ ion trapped simultaneously with another $^{26}Mg^+$ ion, a $^{26}MgH^+$ ion and a $^{26}MgD^+$ ion while modulation frequencies of ν_{26}, ν_{27} and ν_{28} are applied successively. Modulation frequencies around ν_{28}, ν_{27}, ν_{26}, ν_{25} and ν_{24} are applied repeatedly from the moment where two $^{26}Mg^+$ ions are loaded until one $^{26}Mg^+$ ion has reacted and the molecular ion identified. The scan around ν_{26} ensures that everything is calibrated, while the scans around ν_{24} and ν_{25} check for charge exchange collisions as in Ref. [57] for calcium. Production of $^{24}Mg^+$ ions through charge exchange collisions was only observed in two cases out of more than 400 measurements, but even so, we chose to work with the less abundant $^{26}Mg^+$ ion two avoid any confusion in distinguishing $^{24}MgH^+$ and $^{24}MgD^+$ ions from $^{25}Mg^+$ and $^{26}Mg^+$ ions. The $Mg^+ + H_2/HD/D_2$ reaction rate is less than one per minute at the applied molecular gas pressure (1.3×10^{-9} mbar), which means that the above identification procedure can in general be applied before both of the initially loaded atomic ions have reacted. After a reaction product has been identified the trap is emptied, two new $^{26}Mg^+$ ions are loaded and the experiment repeated.

5.3 Two-step model of the reaction process

Because of an unavoidable background pressure of H_2 in our vacuum chamber, it is not possible to study reaction $(a)/(b)$ and (d) alone. To take this background pressure into account and understand quantitatively the branching ratio between reactions (a) and (b), as well as the molecule formation probability between reactions (a) + (b), (c) and (d), we model the reactions as two-step processes. In the first step the neutral molecule is assumed to be captured by the $^{26}Mg^+$ ion at long range to form a $MgHD^+$, MgH_2^+ or MgD_2^+ collision complex and, in the second step, a stable MgH^+or MgD^+ion is formed from this complex at short range.

The capture cross-section for the first step is for the present collision energies well approximated by the Langevin capture cross section $\sigma = (e/2\epsilon_0)\sqrt{\alpha/(\mu v^2)}$ [127], where α is the polarizability of the neutral molecule, μ is the reduced mass, and v is the relative velocity in the center-of-mass system. Since the polarizability of HD, H_2 and D_2 is equal within 1% [128], in our model we assume α to be identical for HD, H_2 and D_2. Because of the low ion oscillation frequencies in the trap, the reduced masses are not significantly different from the free-free reaction cases. The two-step model is valid since the capture range in the first step is of the order of $(\sigma/\pi)^{1/2} \approx 6$ Å which is much larger than the extension of the hydrogen molecule and the Mg^+ ion as well as the de Broglie wavelength relevant for the reaction. If the probability for molecule formation in the second step is denoted by η, the molecular ion formation rate is then given by

$$\Gamma = p_{\mathrm{exc}} n v \sigma \eta \tag{5.1}$$

where p_{exc} is the $^{26}Mg^+$ excitation probability and n is the neutral molecule density. Using that density is proportional to pressure, P, we find that

$$\Gamma = K\frac{P\eta}{\sqrt{\mu}}, \tag{5.2}$$

where $K = \frac{p_{\mathrm{exc}} e\sqrt{\alpha}}{2\epsilon_0 kT}$ is just a proportionality constant equal for reactions (a), (b), (c) and (d). Thus we get

$$\begin{aligned}\frac{N_{MgD^+}}{N_{MgH^+}} = \frac{\Gamma_{MgD^+}}{\Gamma_{MgH^+}} &= \frac{KP_{HD}\eta^{HD}_{MgD^+}/\sqrt{\mu_{HD}}}{KP_{H_2}\eta^{H_2}_{MgH^+}/\sqrt{\mu_{H_2}} + KP_{HD}\eta^{HD}_{MgH^+}/\sqrt{\mu_{HD}}} \\ &= \frac{(\eta^{HD}_{MgD^+}/\eta^{H_2}_{MgH^+})(P_{HD}/P_{H_2})}{\sqrt{\mu_{HD}/\mu_{H_2}} + (\eta^{HD}_{MgH^+}/\eta^{H_2}_{MgH^+})(P_{HD}/P_{H_2})}\end{aligned} \tag{5.3}$$

for reactions with HD and H_2 molecules, and

$$\frac{N_{MgD^+}}{N_{MgH^+}} = \frac{\Gamma_{MgD^+}}{\Gamma_{MgH^+}} = \frac{KP_{D_2}\eta^{D_2}_{MgD^+}/\sqrt{\mu_{D_2}}}{KP_{H_2}\eta^{H_2}_{MgH^+}/\sqrt{\mu_{H_2}}} = \frac{P_{D_2}}{P_{H_2}}\frac{\eta^{D_2}_{MgD^+}}{\eta^{H_2}_{MgH^+}}\sqrt{\frac{\mu_{H_2}}{\mu_{D_2}}} \tag{5.4}$$

for reaction with D_2 and H_2 molecules. Here $\eta^{M'}_{M^+}$ is the efficiency of M^+ (MgH^+or MgD^+) formation after reaction with M' (HD, H_2 or D_2). **Equation 5.3** approaches the branching ratio $\eta^{HD}_{MgD^+}/\eta^{HD}_{MgH^+}$ for large values of P_{HD}/P_{H_2}, i.e., when the vast majority of MgH^+ molecules are produced from reactions with HD rather than H_2. Both expressions are independent of p_{exc} and of the *absolute* partial pressures, which greatly reduces systematic errors. The relative partial pressures are measured with a rest gas analyzer and for all values of the ratios P_{HD}/P_{H_2} and P_{D_2}/P_{H_2} we estimate its systematic uncertainty to be less than 25%.

5.3.1 Reactions with HD

To determine both $\eta^{HD}_{MgD^+}/\eta^{H_2}_{MgH^+}$ and $\eta^{HD}_{MgH^+}/\eta^{H_2}_{MgH^+}$ we measure the number of $^{26}MgD^+$ ions, N_{MgD^+}, and $^{26}MgH^+$ ions, N_{MgH^+}, formed at four different ratios of the partial pressure of HD and H_2, P_{HD}/P_{H_2}. The obtained results are presented in **figure 5.2** and show an increase of MgD^+formation with increased HD pressure.

Fitting **equation (5.3)** to the data results in $\eta^{HD}_{MgD^+}/\eta^{H_2}_{MgH^+} = 0.73 \pm 0.17$ and $\eta^{HD}_{MgH^+}/\eta^{H_2}_{MgH^+} = 0.06^{+0.10}_{-0.06}$. From these parameters the branching ratio $\eta^{HD}_{MgD^+}/\eta^{HD}_{MgH^+}$ can be determined. Taking the statistical uncertainties into account, we find that the branching ratio is unbound from above and has a lower limit of 5, thus demonstrating a dramatic intramolecular isotope effect. In addition, the $(\eta^{HD}_{MgD^+}+\eta^{HD}_{MgH^+})/\eta^{H_2}_{MgH^+}$ ratio is consistent with unity which indicates that the probability of forming a molecular ion is equally large from either of the two complexes MgH_2^+ or $MgHD^+$.

5.3.2 Reactions with H_2 and D_2

In a second series of measurements we studied reactions between $^{26}Mg^+$ and a mixture of 43 ± 2% H_2 and 57 ± 2% D_2 gas. We observed the production of 40 MgH^+ ions and 25 MgD^+ ions which yields a ratio of 2.1 ± 0.6 between the MgH^+ and MgD^+ reaction rate coefficients. Using **equation (5.4)** it follows that $\eta^{H_2}_{MgH^+}/\eta^{D_2}_{MgD^+} = 1.5 \pm 0.4$.

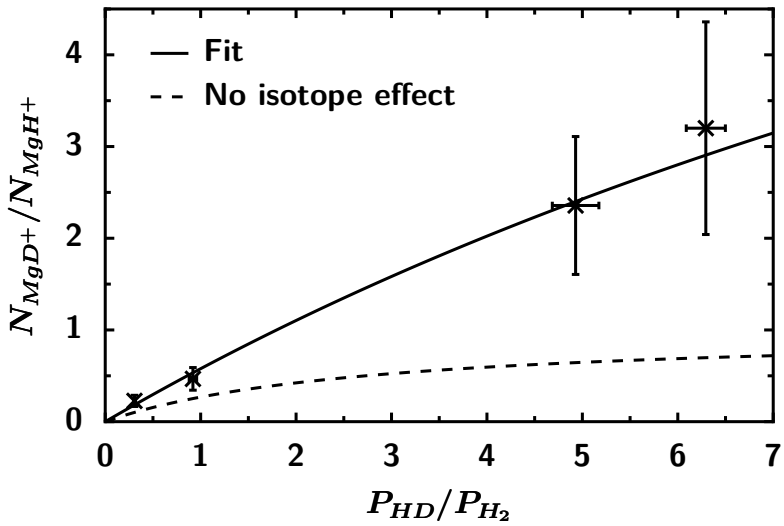

Figure 5.2 The ratio between the number of formed $^{26}MgD^+$ and $^{26}MgH^+$ ions vs the relative pressure of HD and H_2. From left to right the data points correspond to N_{MgD^+} = 17, 21, 33, and 32 and N_{MgH^+} = 75, 45, 14, and 10. The error bars represent statistical uncertainties. A fit of **equation (5.3)** to the data results in $\eta^{HD}_{MgD^+}/\eta^{H_2}_{MgH^+} = 0.73 \pm 0.17$ and $\eta^{HD}_{MgH^+}/\eta^{H_2}_{MgH^+} = 0.06^{+0.10}_{-0.06}$ (solid line). The dashed line represents **equation (5.3)** in the absence of isotope effects, i.e., with $\eta^{HD}_{MgD^+}/\eta^{H_2}_{MgH^+} = \eta^{HD}_{MgH^+}/\eta^{H_2}_{MgH^+} = 0.5$.

5.3.3 Substitution reactions

Substitution reactions between a $^{26}MgH^+$ or $^{26}MgD^+$ ion and a H_2, HD or D_2 molecule could potentially give rise to a systematic error. Such reactions were, however, only observed on two occasions (one $MgH^+ + D_2 \rightarrow MgD^+ + HD$, one $MgD^+ + H_2 \rightarrow MgH^+ + HD$) in a period of more than 20 minutes and hence they do not give rise to systematic errors on the results presented here.

5.4 Discussion

The most striking of the above results is the strong intramolecular isotope effect in reactions (*a*) and (*b*). This finding cannot be explained by a simple statistical model based on an assumption of an equal probability for populating energetically accessible states of $^{26}MgH^+$ and $^{26}MgD^+$. This assumption only gives rise to $\eta^{HD}_{MgD^+}/\eta^{HD}_{MgH^+} \approx 2$ [R. Wester, private communication] and basically reflects the

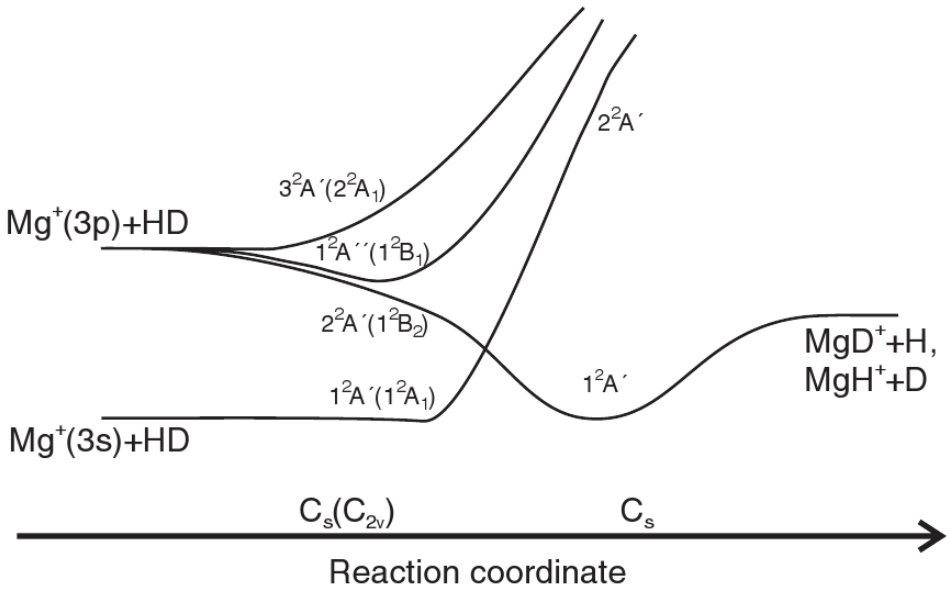

Figure 5.3 Sketch of relevant potential surfaces in C_s symmetry for the Mg^+ + HD reaction proceeding by insertion of Mg^+ into the HD bond on the $2\,^2A'$ potential surface, followed by Mg^+–D or Mg^+–H bond formation. On the left-hand side the C_{2v} symmetry labels in parentheses are valid for the analogous reaction with H_2 or D_2 [130, 131].

smaller level spacing in the MgD^+rovibrational levels (see e.g. Ref. [129, section III 2 (g)]). Therefore we attribute the observed isotope effect to a dynamical mechanism. In the ion beam experiments of Ref. [125] a similar isotope effect has been observed in reactions between *ground state* Mg^+ ions and HD molecules at center-of-mass energies up to 11 eV.

In **figure 5.3** we sketch the potential surfaces involved in the reaction. The analogous potential surfaces for MgD_2^+ was explored in a photofragmentation study [132], where MgD^+ ion formation was observed when a laser was red detuned with respect to the atomic $3\,^2S_{1/2}$–$3\,^2P_J$ transition, (corresponding to the transition from the Mg^+(3s) + D_2 asymptote to the red of the Mg^+(3p) + D_2 asymptote in **figure 5.3**). From the observed MgD^+ spectrum it was argued that MgD^+ is formed by direct and fast reactions on the $1\,^2B_2$ surface in C_{2v} geometry through a bondstretch mechanism as well as from the $1\,^2B_1$ state, possibly through a coupling to the $1\,^2B_2$ state. On the $1\,^2B_2$ potential surface the Mg^+ ion becomes inserted in the D_2 bond such that the D-D bond is stretched and eventually broken and a Mg -D bond is formed [132, 130]. Furthermore, no dissociation into Mg^+(3s)

+ D_2 was observed in that study. In our two-step model this corresponds to the values of $\eta^{H_2}_{MgH^+}$, $\eta^{D_2}_{MgD^+}$ and $(\eta^{HD}_{MgD^+} + \eta^{HD}_{MgH^+})$ being close to unity, which indeed is in good agreement with the Mg + H_2 reaction rate measured in a previous study [35, 69].

The above mentioned photofragmentation study indicate that the Mg^++ HD reaction discussed in this chapter proceeds via the $2\,^2A_0$ surface through a bond-stretch mechanism that eventually favors the formation of MgD^+. However, a full understanding of the transition from a $MgHD^+$ complex to a potential surface favoring the MgD^+ + H asymptote rather than the MgH^+ + D asymptote requires a detailed theoretical study. Here it might be necessary to consider the details of the conical intersection which arises from the crossing of the $1\,^2A_0$ and $2\,^2A_0$ potential surfaces, since non-adiabatic couplings at the conical intersection could give rise to a preference of the MgD^+ channel over the MgH^+ channel. Our results suggest that the observed isotope effect arise through a dynamic mechanism in the exit channel of the reaction. The same mechanism could be responsible for the isotope effect observed in reactions with ground state Mg^+ ions in Ref. [125] where it was suggested that thermodynamic threshold effects in the entrance channel could lead to a preference of MgD^+ production. The distribution over rovibrational levels in the formed molecular ion has not been investigated in the present study and it may contribute further information on dynamical effects in the exit channel, as found in studies of the analogous reactions between excited state neutral Mg [133, 134] as well as Na [135] and HD.

5.5 Conlusion

In the reactions between Mg^+ in the $3p\,^2P_{3/2}$ excited state and HD molecules at thermal energies it was found that the formation of MgD^+ was more than 5 times more likely than the formation of MgH^+. Furthermore, reactions with H_2 and D_2 showed that the molecular ion formation efficiencies after capture of a HD, H_2, or D_2 molecule are equal within statistical uncertainties and consistent with unity. This agrees well with previous experiments on photofragmentation of MgD_2^+ [132].

In conclusion, we have demonstrated that the branching ratios and relative reactions rates in ion-neutral reactions can be determined by observing only a feq hundred single reactions. Studies of exootic or rare reactions, e.g., chemistry of superheavy elements, would benefit greatly from this low number of needed reactions [93, 94, 95].

This experiments also demonstrate the prospects for similar single molecular ion studies using, e.g., state prepared molecular ions [44, 45], more complex molecular ions [39, 40], or molecular ions of astrophysical relevance [136, 33].

Chapter 6

Rotational cooling of molecular ions

The versatility of sympathetic cooling of molecular ions has been demonstrated in the previous chapter. However, due to the long distances between ions in a Coulomb crystal, sympathetic cooling does not alter the internal degrees of freedom [137]. While several schemes to achieve ground state cooling exists, in this chapter we demonstrate one which is relatively simple to implement, leaves the cold molecular ions well localized and has the potential to work on a single molecular ion. With MgH^+ as our favourite test molecular ion, we show how an almost 15-fold increase in the rotational ground state population can be obtained through a simple optical pumping scheme [44, 45]. The resulting ground state population of $37 \pm 2\%$ is equivalent to that of a thermal distribution at 21 ± 2 K, which implies that cold molecular ion experiments can now be performed at cryogenic temperatures in room temperature experimental setups.

The chapter is organized as follows. In **section 6.1**, the basics of the rotational cooling scheme will be presented including a description of the light source to be applied for the cooling of MgH^+. Next, in **section 6.2**, the basic experimental procedure is presented. To probe the population in different rotational states, the molecular ions are state selectively dissociated in either a one- or two-color 1+1 Resonance Enhanced Multi-Photon Dissociation (REMPD) scheme. Results from the one color dissociation scheme is presented in **section 6.3**, which is immediately followed by the results from the two color scheme in **section 6.4**. Finally, in **section 6.5**, the results presented are summed up.

6.1 Rotational cooling of molecular ions

As already mentioned, the typical storage time of trapped molecular ions is hours. Hence, internal equilibrium with the blackbody radiation (BBR) field can easily be reached for polar molecular ions. Because of the large spacing between the vibrational energy levels in light diatomic molecular ions, almost all of the population will be in the vibrational ground state at room temperature. For example for MgH^+ ions, more than 99.9% of the population is in the vibrational ground state. However, the spacing between rotational levels are much smaller, and the 300 K BBR field populates a significant number of rotational states. Even for a light diatomic molecular ion such as MgH^+, with a large rotational constant of $B = 9$ K for low lying vibrational levels in the electronic ground state, more than ten rotational levels is populated by more than a few percent (see e.g. the grey bars in **figure 6.2** (a)). This is thus the starting point for further cooling.

Before discussing the cooling scheme that we have implemented, lets take a short look at some of the alternatives. A well known method is that of buffer gas cooling with Helium, which can significantly reduce the rotational temperature [32]. However, this is achieved at the cost of an increased translational temperature, due to collisions with the buffer gas. In principle this could be circumvented by laser-cooling the neutral buffer gas, but charge-exchange processes will likely neutralize the molecular ions as observed in the case of MgH^+–Rb [138]. Buffer gas cooling is also ruled out, if the research objective relies on long term internal state coherences of the cold molecular ions.

Another well known and general way of reducing the rotational temperature is to alter the blackbody radiation field by cryogenic cooling as well as efficient shielding of the entire ion trap. In this way internal temperatures below 10 K can be reached [32, 34], however, optical access to the trapped ions is limited by the shielding. Furthermore, a significant part of the population of heavier molecular ions like CaO^+ or BaO^+ [37, 139] would still remain in higher rotational states.

Cooling by optical techniques seems less straightforward due to the many, unevenly spaced rotational states. Nevertheless, rotational cooling by optical pumping can be obtained, as first proposed by Bahns *et al* in [12], by chirping the frequency of a laser through specific P-branch transition frequencies. More recently, vibrational cooling by a spectrally shaped fs-laser pulse was demonstrated [18]. The same method can in principle be applied for rotational cooling if the ground rotational state can be spectrally resolved by the spectral shaping device and vibrational heating avoided.

The cooling scheme that we have implemented, was proposed by Vogelius *et al* [44, 45, 46]. Here optical pumping to the rotational ground state is obtained by driving only a single or two dipole allowed transitions while *taking advantage* of the blackbody radiation field to redistribute population among the rotational levels. Numerical simulations show that starting from an initial thermal distribution at 300 K more than 70% of the population can be cooled to the ground state for MgH^+ ions (using the so-called Raman scheme), and for ArH^+ even about 90% can be obtained (using the so-called direct scheme based on dipole allowed transitions within the $X\,^1\Sigma^+$ ground state potential). The generality of this optical pumping technique was demonstrated in [45] by extending the scheme from $^1\Sigma$ electronic ground states, as for MgH^+ and ArH^+, to molecules having a $^2\Sigma$, $^3\Sigma$ or $^2\Pi$ ground state. From an experimental point of view the proposed scheme is attractive since it requires only a few commercially available laser sources. In the following a particularly simple scheme which requires just a single infrared cw laser source is discussed.

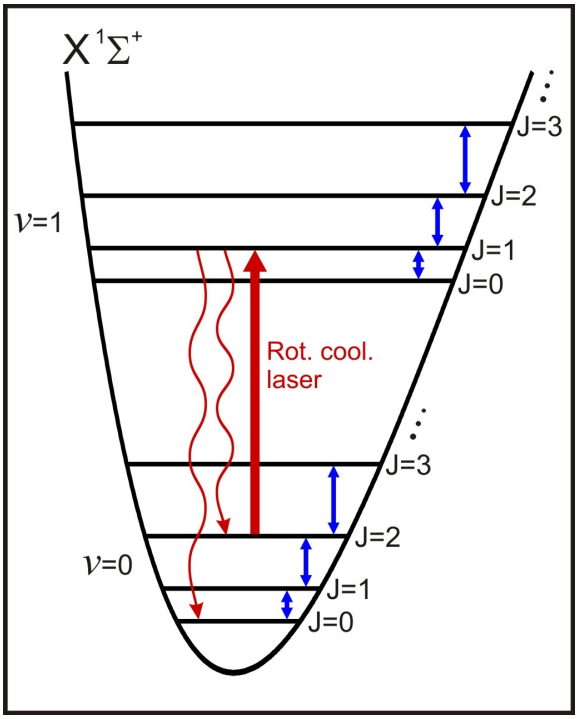

Figure 6.1 Simplified scheme for rotational cooling of MgH^+. A laser drives the $|v = 0, J = 2\rangle - |v = 1, J = 1\rangle$ transition which leads to optical pumping towards the $|v = 0, J = 0\rangle$ state. In combination with blackbody radiation driven transitions, rotational cooling is obtained.

6.1.1 Simplified scheme for cooling of MgH^+

As a first implementation of this technique, we focus on an experimentally simple case involving only a single infrared cw laser. This laser optically pumps population from $|v = 0, J = 2\rangle$ to $|v = 0, J = 0\rangle$ via the $|v = 1, J = 1\rangle$ state, as sketched in **figure 6.1**. Together with the BBR field, which simultanously redistributes the population between the rotational levels, the optimal pumping not only empties $|v = 0, J = 2\rangle$, but also higher lying levels.

In the following two subsections, we will first take a look at a theoretical model of the cooling scheme and then give a description of the experimental cooling laser setup.

6.1.1.1 Numerical modelling of the cooling scheme

We model the population dynamics by propagating a set of coupled rate equations, each describing the change in population of a given state via Einstein coefficients and frequency-specific radiation intensities. E.g. the population in state i changes as

$$\begin{aligned}\frac{dp_i}{dt} = &-\sum_{j=0}^{i-1} A_{ij}p_i + \sum_{j=i+1}^{M} A_{ji}p_j \\ &-\sum_{j=0}^{i-1} W(\omega_{ij})B_{ij}p_i + \sum_{j=0}^{i-1} W(\omega_{ij})B_{ji}p_j \\ &-\sum_{j=i+1}^{M} W(\omega_{ij})B_{ij}p_i + \sum_{j=i+1}^{M} W(\omega_{ij})B_{ji}p_j \end{aligned} \tag{6.1}$$

where p_i is the population of state i, M is the total number of states, A_{ij} and B_{ij} are the Einstein coefficients describing spontanous and stimulated transitions between state i and j, and $W(\omega_{ij})$ is the radiative energy density at the resonant transition frequency $\omega = \omega_{ij}$ between states i and j.

Equations (**6.1**) can be expressed more conviniently by the matrix equation

$$\frac{d\vec{p}}{dt} = \boldsymbol{K}\vec{P} \tag{6.2}$$

where the coupling matrix is given by $\boldsymbol{K} = \boldsymbol{A} + \boldsymbol{W} \circ \boldsymbol{B}$ (the $\circ$-operator denotes the Hadamard product) and $\vec{p}$ is a vector holding the populations in each state:

$$\vec{p} = [p_0, p_1, \ldots, p_M] \tag{6.3}$$

The solution to **equation (6.2)** is simply:

$$\vec{p}(t) = \exp(\boldsymbol{K}t)\vec{p}(0) \tag{6.4}$$

The effect of the cooling laser is included by changing the two entries in the coupling matrix that hold the transition rates for $|v = 0, J = 2\rangle \rightarrow |v = 1, J = 1\rangle$ and $|v = 1, J = 1\rangle \rightarrow |v = 0, J = 2\rangle$. These rates are chosen to be large enough that the transition saturates.

The Einstein coefficients are determined theoretically in the following way. First, the electronic ground state potential and the permanent dipole moment function is evaluated with *Gaussian* [140] with a coupled cluster single, double

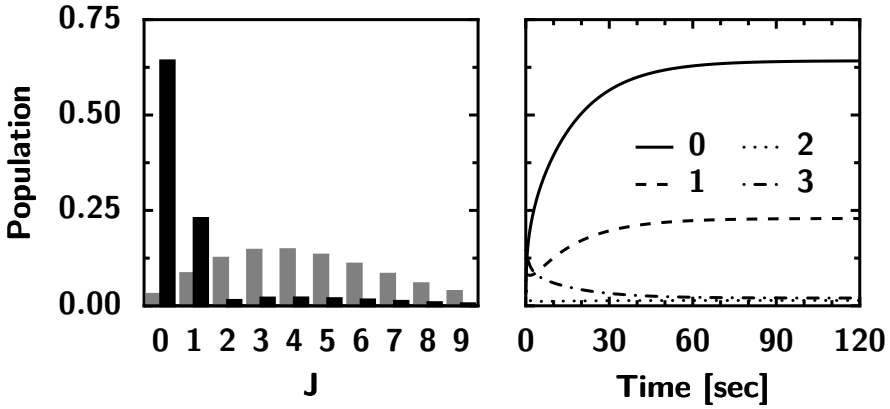

Figure 6.2 (a) Calculated steady state populations at 300 K and after cooling. (b) Temporal evolution of the lowest rotational states for the cooling scheme illustrated in **figure 6.1**.

and triple excitation (CCSDT) approach on a 6-311++G basis set. Next, rovibrational eigenfunctions are found by solving the Schrödinger equation using the Numerov method via the program *Level 8.0* [141] and finally Einstein A coefficients, A_{ij}, are found from these wavefunctions and the permanent dipole moment:

$$A_{ij} = \frac{\omega_{ij}^3 |D_{ij}|}{3 g_i c^3 \epsilon_0 \hbar \pi}, \tag{6.5}$$

where $|D_{ij}|$ is the transition dipole moment between the states and g_i is the degeneracy of state i. The corresponding Einstein B coefficients are given by

$$B_{ij} = \frac{c^3}{4h\nu_{ij}^3} A_{ij} \tag{6.6}$$

$$B_{ji} = \frac{g_i}{g_j} B_{ij}, \tag{6.7}$$

where $\nu_{ij} = \omega_{ij}/2\pi$ is the frequency difference between state i and state j, and $g_i = 2J + 1$ is the degeneracy of the state i with rotational quantum number J.

In **figure 6.2** the steady state populations and the time evolution of the lowest J states are presented. The steady state ground state population of 64% is not much lower than the $\approx$ 70% obtained by applying an additional laser source [44] or an incoherent radiation source [45]. Steady state is reached in about one minute, a period much shorter than the storage time of cold molecular ions (several hours)

and a few times shorter than the average time between collisions with residual gas which we estimate to be 200 s per ion.

6.1.1.2 Infrared diode laser system for cooling of MgH^+

To implement the above described cooling scheme we need a tunable laser source capable of saturating the $|v = 0, J = 2\rangle - |v = 1, J = 1\rangle$ transition in MgH^+ at 1608.96 ± 0.05 cm^{-1} (corresponding to a wavelength of 6.2 μm) [142]. We have chosen to use a PbSe based lead salt diode laser from Laser Components, but other alternatives exist; E.g. an optical parametric oscillator system or a quantum cascade laser could fulfill the criteria. These systems are, however, either more expensive or lack continuous coverage of the part of the infrared spectrum relevant for rotational cooling of other molecular ions than MgH^+ [45].

The lead salt diode laser setup is sketched in **figure 6.3**. The laser itself is housed inside a liquid nitrogen dewar together with a heating element, which is used to control the temperature. Right after exiting through a BaF_2 window, the laser beam is collimated by an off-axis parabolic mirror. Further beam shaping is performed by a telescope and a cylindrical lens (not shown in **figure 6.3**), such that FWHM of the beam profile measures 3.2 mm horizontally and 0.9 mm vertically in the center of the trap. Inside the ion trap the total power is 200 μW, which is sufficient to saturate the $|v = 0, J = 2\rangle - |v = 1, J = 1\rangle$ transition for all orientations of the molecule, when the polarization of the laser is scrambled on a time scale faster than the lifetime of the $|v = 1, J = 1\rangle$ level. In the experiments, the polarization of the laser is constantly rotated at a rate of 4 Hz. The linewidth of the laser is assumed to be $\approx$ 20 MHz [143]. The laser does not affect other transitions within the 0–1 band, since these are far away [142].

To guide the infrared beam, we overlap it with a HeNe laser beam, as also shown in **figure 6.3**. Besides guiding, this HeNe beam is also used to calibrate a monochromator, which can perform coarse measurements of the infrared beam with a precision of about 2 cm^{-1}. In order to obtain a more accurate absolute frequency reference, an ammonia filled cell (6 cm long filled with $\approx$ 25 mbar NH_3 and equipped with CaF_2 windows) is employed for absorption spectroscopy. Precise relative frequency measurements are achieved by a solid Germanium etalon with a free-sprectral-range of 0.048632(10) cm^{-1} for a laser frequency within 20 cm^{-1} of 1609 cm^{-1} and a temperature in the range 18–22°C. In all experiments, an ac-coupled Mercury-Cadmium-Telluride detector (Judson J15D with PA-101 pre-amplifier) is utilized.

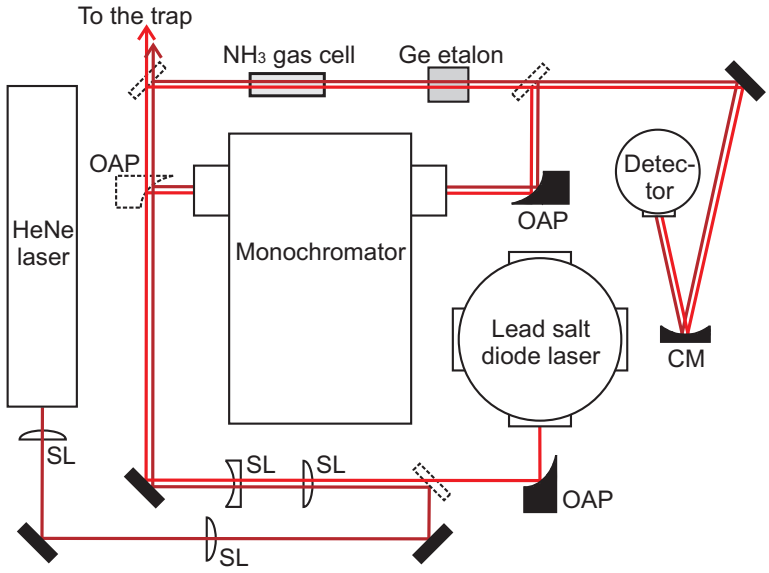

Figure 6.3 Setup of the lead salt diode laser system. Details of the various components are given in the text. The diode laser and the HeNe laser beam are overlapped but displaced here for clarity. The gas cell and the etalon (not transmitting for the HeNe laser) are removable. OAP: off-axis parabolic mirror, CM: concave spherical mirror, SL: spherical lens. Planar mirrors are indicated as rectangles, dashed lines indicate flip mounted mirrors.

In **figure 6.4** the calibration procedure is outlined via different recorded spectra. **Figure 6.4** (a) shows the transmission spectrum of the Ge etalon, when the diode laser frequency is scanned by modulation of the injection current. The same scan range is used in (b), where the detector signal is shown when the ammonia cell is inserted in the beam path (lower trace) and when it is removed (upper trace). The broad line (about 0.2 cm^{-1} wide) present in both spectra near 1609.45 cm^{-1} is due to absorption in water present in the air along the 1.9 m long beam path from the laser to the detector. In (c), the upper trace is subtracted from the lower one, which almost eliminates the water line, as well as the background slope due to the current dependent output power of the laser. The three $\approx$ 0.02 cm^{-1} wide ammonia lines are now the only features left. All linewidths are dominated by collision broadening, as the Doppler broadening is only 5×10^{-3} cm^{-1} and the laser linewidth is expected to be even smaller, about $6{\times}10^{-4}$ cm^{-1} [143]). The lines in **figure 6.4** (c) can be identified by a coarse frequency measurement with the monochromator together with an evaluation of the frequency spacing between the lines marked A, B and C, as well as the water line. The lines are due to transitions at 1609.06116 cm^{-1} (A), 1609.46570 cm^{-1} (B) and 1609.50671 cm^{-1} (C),

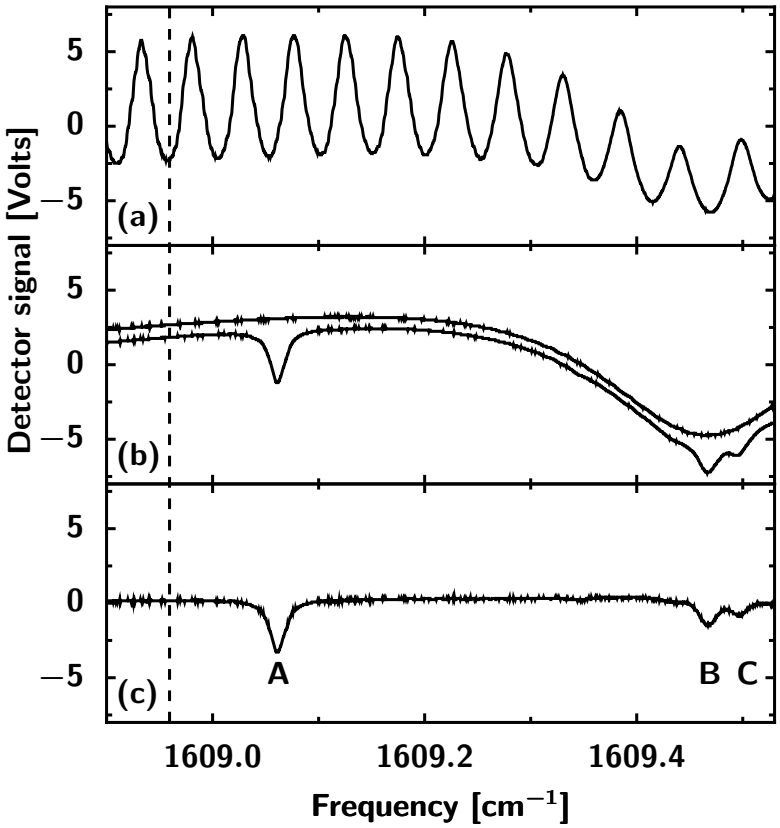

Figure 6.4 Spectra obtained with the lead salt diode laser setup shown in **figure 6.3**. (a) Transmission spectrum of the Ge etalon. (b) Transmission spectrum of the ammonia cell (lower trace) and detector signal with the cell removed from the beam path (upper trace) showing a water absorption line near 1609.45 cm^{-1}. The latter trace is displaced by 1 V for clarity. (c) Difference between the lower and upper traces in (b). The three lines marked by A, B and C are ammonia absorption lines. The vertical dashed line indicates the frequency of interest for rotational cooling of MgH^+.

respectively [144]. The absolute frequency scale is constructed by first fixing the scale to 1609.06116 cm^{-1}at the center of line A and then scaling the frequency axis according to the etalon spectrum in **figure 6.4** (a). It is now simple to scan the laser around the desired frequency of 1608.96 ± 0.05 cm^{-1} [142] to perform the cooling experiments.

6.2 Photodissociation spectroscopy of cold molecular ions

In order to determine the rotational state distribution for the vibrational ground state of the $X^1\Sigma^+$ electronic ground state of MgH^+, the molecules are state selectively dissociated with a 1+1 Resonance Enhanced Multi-Photon Dissociation (REMPD) technique. The two photons can either be the same color or different, and both methods will be presented below. In short, all such measurements consist of four steps:

1. Mg^+ ions are loaded into the trap and laser-cooled, as described in **chapter 2**.
2. H_2 is introduced to form MgH^+ molecular ions through reactions between Mg^+ and H_2 (**section 6.2.2**).
3. The MgH^+ ions are left to equilibrate with the blackbody radiation field for at least 60 s. At this point, either the laser is applied, in which case the waiting period is extended to 120 s or a control experiment is performed (**section 6.2.3**).
4. By applying one or two pulsed lasers the MgH^+ ions are dissociated in a rotational state selective two-photon dissociation process. Since the dissociation products, Mg and H^+, are both lost from the trap, the loss number of molecular ions equals the number of dissociated molecules (**section 6.2.4**).

The rest of this section is dedicated to describing the common steps of the two photodissociation methods, while the detailed description of the methods and their results will be given in individual sections later on.

6.2.1 Trapping and laser cooling of Mg^+ ions

Apart from the additional pulsed dissociation laser beam(s) and the PbSe laser beam, the setup is identical to the one used previously. In contrast, however, to the previous experiments, we have chosen to work with many ions at a time, to increase the signal. When the ions are Doppler laser cooled to a temperature of ≈ 10 mK they form an ordered structure, a so-called Coulomb crystal. The total magnification of the imaging system is $\times 4.0$ and chosen such that Coulomb crystals of several thousand ions are fully contained within the imaging region. An example of a projection image of such a cylindrically symmetric crystal is presented in **figure 6.7** (Image I). The ions are observed in real time, so the loading of $^{24}Mg^+$ ions can easily be terminated by blocking the photoionization laser beam, once the Coulomb crystal has the desired size. The sudden termination of the loading process can be seen in region 1 on the graph in **figure 6.7**. Subsequently a

rotatable mechanical shutter is turned to block the atomic beam in order to avoid impact with the trapped ions.

6.2.2 Production of translationally cold MgH^+ ions

As in **chapter 4**, MgH^+ ions are formed by leaking H_2 gas into the trap chamber (base pressure 4.0×10^{-10} mbar) through a leak-valve such that a steady-state pressure of 2.0×10^{-9} mbar is maintained. Reactions between Mg^+ ions in the ground state and thermally excited hydrogen molecules are not energetically allowed, but during the laser cooling process, Mg^+ ions are excited to the $3p\,^2P_{3/2}$ state, from which reactions can take place. Since the scattering rate depends on the detuning of the cooling laser, this provides us a knob with which the reaction rate can be controlled. As also mentioned in **section 5.2**, the formed molecular ions stay trapped, since the trap depth of about 1 eV is higher than the acquired kinetic energy. The molecular ions interact with the remaining laser cooled Mg^+ ions through the Coulomb interaction and are sympathetically cooled to a temperature below 100 mK within a fraction of a second. As seen in Image II in **figure 6.7**, the heavier molecular ions separate radially outside the lighter Mg^+ ions due to the mass-dependence of the radial trapping potential given by **equation (2.7)**. After one to two mintues the desired number of $^{24}MgH^+$ ions has been formed and the reaction process is terminated by red-detuning the cooling laser $\approx$ 200 MHz and closing the leak valve. This is clearly visible in the graph in **figure 6.7** at the transition between region 2 and 3.

6.2.3 Equilibration and manipulation of the rotational state distribution

The $^{24}MgH^+$ ions are formed in a range of rovibrational states in $X^1\Sigma^+$ or other electronic potentials. With rates of $\approx$ 20 s^{-1} the molecular ions decay towards $v = 0$, while the rotational equilibration of the $v = 0$ level is reached within one minute (see **section 6.3.3**). Thus a waiting period of one minute is introduced between the loading of the molecular ions and the probing of the population. If the cooling laser is applied we wait an additional minute, to make sure that the steady state population is reached (see **figure 6.2** and **figure 6.13**). In this period, the ion numbers remain constant as can be seen in region 3 on the graph in **figure 6.7** and the ongoing pumping of the H_2 gas leave us with a pressure of less than 4.7×10^{-10} mbar by the end of period 3. The total rate of collisions after the waiting period is consequently not much higher than at the base pressure of the vacuum chamber

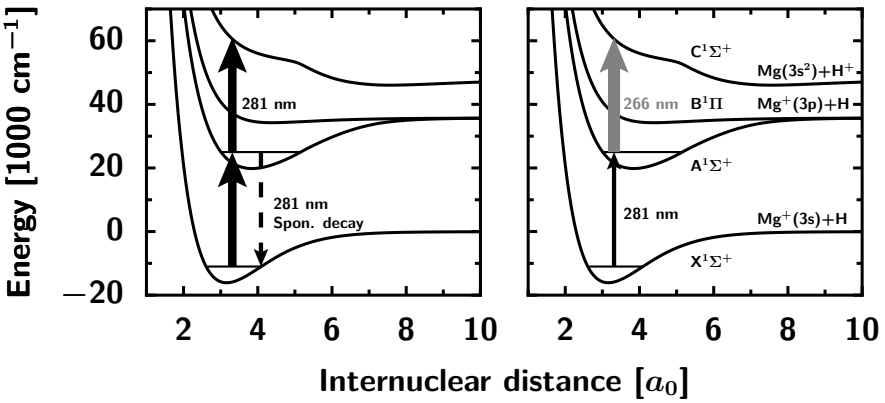

Figure 6.5 Schemes for resonance-enhanced two-photon dissociation of MgH^+. (Left) Both the first and second step is done with UV photons near 281 nm from the same pulse. Because the second step is relatively slow, a big fraction of the molecular ions spontaneously decays back into various rotational and vibrational levels of the electronic ground state. (Right) In the two color scheme, the second step is performed with a photon from an intense 266 nm pulse. The resulting high dissociation probability prevents spontaneous decay to happen before the molecule is dissociated and at the same time allow to operate with much lower 281 nm intensities, thus avoiding powerbroadening of the first transition.

6.2.4 Rotational state selective photodissociation of MgH^+ molecular ions

Finally, the population in each rotational level is probed by the following rotational state selective 1+1 REMPD technique. The scheme for photodissociating MgH^+ ions in the $X^1\Sigma^+(v = 0, J)$ state is illustrated in **figure 6.5**. In the resonant first step the molecular ion is excited by a pulsed ns-laser to the $A^1\Sigma^+$ state on a P- or R-line of the 0-0 band near 281 nm [142]. In the second step the molecular ion is excited to a continuum state of the $C^1\Sigma^+$ potential, either by a photon from the same pulse as the first step [**figure 6.5** (a)] or by a photon from a temporarily overlapping pulsed beam at 266 nm in the case of two color photodissociation [**figure 6.5** (b)]. The pros and cons of the one and two color dissociation schemes will be discussed in **section 6.2.4.1**.

From the continuum state of the $C^1\Sigma^+$ potential, the MgH^+ ion rapidly dissociates to a neutral Mg atom and a proton. Neither of these particles are bound in the trap, so the lost number of molecular ions in the trap equals the number of dissociated molecular ions. When all MgH^+ ions have been dissociated, a Mg^+ Coulomb crystal much smaller than the original one is left behind (see Image III in **figure 6.7**). A small amount of non-fluorescing ions heavier than $^{24}Mg^+$ remains. These ions are either $^{25}Mg^+$ or $^{26}Mg^+$ ions formed by charge-exchange

reactions[2] between Mg atoms and $^{24}Mg^+$, or unknown molecular ions, most likely N_2^+, formed by ionization of residual gas molecules by the pulsed laser. The rate at which such "dark" ions are loaded into the trap is lowered when the liquid nitrogen container mentioned in **section 2.1** is utilized, since particles from the residual gas "sticks" to the cold surface, resulting in a lower pressure.

6.2.4.1 One versus two color photodissociation

In the one color dissociation scheme, the laser frequency is tuned around 281 nm to address one of the rotational states in the first step. The dissociation rate for the second step is essentially independent of the laser frequency within this range and can be described by $\Gamma_{\text{diss}} = \alpha I_{\text{peak}}$, where the proportionality constant, α, is of the order of 1 $s^{-1}W^{-1}cm^2$ and I_{peak} is the peak intensity of the pulse [145]. To lower the effect of power-broadening in the first step, which compromises our spectral resolution, the intensity of the laser is kept below $\approx 2\times10^6$ W/cm^2 near the center of the pulse. This, however, cause the dissociation rate from the A state to be of the order of 10^6 s^{-1}, and thus much smaller than the rate of spontaneous decay from the A to the X state, which is about 2×10^8 s^{-1}. Consequently, the spontaneous decay back to the rovibrational states in the electronic ground state dominates the dissociation, leading to a distribution of population in the rotational states which is expected to be different from the equilibrium distribution prior to the pulsed laser. The situation is further complicated by transitions from neighbouring levels that, due to interaction with the blackbody radiation, will start to fill up the level that was already probed by the pulsed laser. Due to these redistribution processes, the dissociation rate measured when the ns-laser is tuned to be on resonance with a specific P- or R-line is not directly proportional to the steady state population of the initial $X^1\Sigma^+(v = 0, J)$ state and numerical modeling is necessary to fully account for the many processes (as in Ref. [137, 145]).

This is where we turn to two color photodissociation. If a second pulsed laser beam which drives the dissociative A–C transition while being far-off resonant with all X–A transitions is introduced, the A–C dissociation rate can be increased so much that it dominates the spontaneous decay, and the need for numerical modelling is eliminated. The cost of this manoeuvre is the experimental complication of the additional laser beam. The relative high intensity of the 266 nm light cause two potential problems. First, the rate at which residual gas is ionized and

[2] Similar reactions have previously been exploited with calcium ions [57]. See also **section 5.2**, where the charge-exchange reaction rate is shown to be low.

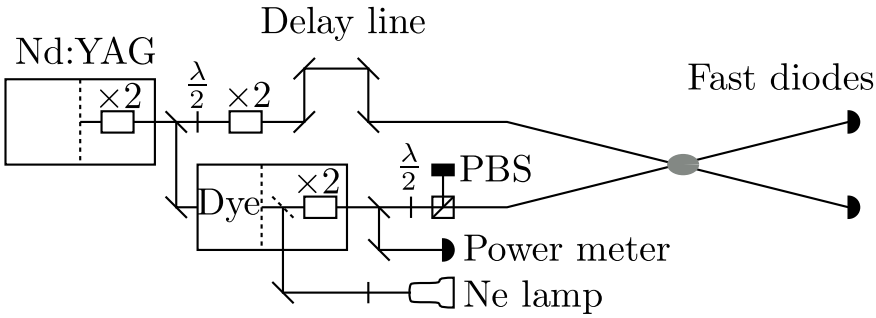

Figure 6.6 Setup of the pulsed laser system. Initially 1064 nm light from a Nd:YAG laser is frequency doubled by an internal KDP crystal. The resulting 532 nm light beam is then split into two beams by a 50-50 beam splitter. One beam is further frequency doubled before going to the trap chamber via a delay line. Control of the 266 nm intensity is provided by a $\lambda/2$ plate right before the doubling step. The other beam is used to pump a dye laser (Rhodamine 6G). This laser is calibrated to Ne lines via an opto galvanic spectroscopy setup. The output of the laser is frequency doubled in a BBO crystal resulting in a 281 nm beam. This beam is further split in two, where on is used for power monitoring and the other goes to the trap. Fine grained control of the intensity of the beam is achieved by a $\lambda/2$ plate and a polarizing beam splitter. On the other side of the chamber, two fast photodiodes is used to monitor the single pulses.

trapped is increased. This could potentially compromise the final volume determination of the remaining MgH^+ ions, but since only very few pulses are needed, the amount of ionized "dark" atoms or molecules was observed to be negligible. Furthermore, the data can easily be corrected for this effect, simply by measuring the number of unwanted ions loaded per pulse. Secondly, the intensity is high enough to dissociate MgH^+ ions off-resonantly. However, this dissociation rate can be measured, and the data corrected. In the results presented in **section 6.4** the typical two photon off-resonant dissociation of the pulsed laser was typically responsible for the dissociation of $\approx 1\%$ of the molecular ions.

6.2.4.2 Photo-dissociation lasers

The pulsed laser setup is sketched in **figure 6.6**. First we have a 10 Hz 10 ns Nd:YAG laser which is frequency doubled by an internal KDP crystal. This doubled output is split in a 50-50 beam-splitter, where one beam is used to pump a Sirah Cobra Stretch dye laser with Rhodamine 6G laser dye, while the other beam goes to a KDP crystal where it is doubled to 266 nm.

The beam from the dye laser is further frequency doubled by a built-in frequency doubling unit, which consists of a BBO crystal in an oven and a horizontal

walk-off compensation and results in pulses with a duration of 9 ns FWHM. The walk-off compensation ensures that the beam is displaced by less than 50 μm in the horizontal plane in the trap center when the fundamental wavelength is scanned over the relevant range of 560–562 nm, while the drift of the beam position is limited to 100 μm over several hours. Shortly after the output port of the dye laser, the beam is further split in two, where one beam passes to the trap, while the other is used for power monitoring. The 281 nm beam going to the trap has a peak intensity of $\approx 2 \times 10^6$ W/cm^2, which can be turned further down by a $\lambda/2$ plate and a PBS. In the trap center the dimensions of the beam are 0.7 mm FWHM horizontally and 1.5 mm FWHM vertically. The dye laser is calibrated to lines in Ne by optogalvanic spectroscopy using a hollow cathode lamp. The linewidth of the fundamental dye laser output is less than 0.08

The 266 nm beam is spatially filtered by a 5 mm pin-hole to minimize intensity fluctuations in the spatial profile of the beam. This happens at the cost of reduced intensity at the trap center, where we are currently limited to peak intensities of $\approx 2 \times 10^7$ W/cm^2 with a beam size of 1 mm FWHM both horizontally and vertically. After the filtering, the beam is lead through a delay line, such that pulses arrive 3 ns before the pulses from the 281 nm dye laser beam at the trap center. The rationale behind this is to have the 266 nm pulse present when the population in the A state is maximal which, according to simulations (see **section 6.3.3**) happens a short time before the maximum of the 281 nm pulse. For further discussion of this, see **section 6.3.4** as well as Ref. [146].

6.2.5 Crystal volume determination

To determine the number of dissociated molecular ions, the molecular ions left in the Coulomb crystal is counted in the following way. Because of the mass dependence of the radial trap frequency (see **equation (2.7)**), ions with different mass separate radially with heavier ions on the outside of the crystal. The inner component has a cylindrical structure, whereas the edge of the outer component maintains its spheroidal shape [147]. The spheroidal shape of this *prolate two-component* crystal is essentially identical to that of a one-component crystal of the *heavier* ion species [147]. Since the mass difference between the two ion species in our case is small, the aspect ratio for a one-component MgH^+ crystal is well approximated by that of a Mg^+ crystal. This implies that the aspect ratio of our two-component crystal is nearly equal to the aspect ratio of the initially pure Mg^+

crystal before H_2 gas is leaked into the trap chamber[3]. Furthermore the aspect ratio is independent on the crystal size.

The volume analysis now proceeds as follows. From the first few images of the pure Mg^+ crystal, the aspect ratio is determined as the ratio between the longest uninterrupted row and column of pixels with values above a chosen threshold. The total crystal volume can now be found at all times (that is, for both one- and two-component crystals) by measuring the half-length of the crystal and applying the equation for the volume of a spheroid

$$V = \frac{4}{3}\pi R^2 L = \frac{4}{3}\pi \alpha^2 L^3, \tag{6.8}$$

where R and L is the transverse and conjugate radii, respectively, and $\alpha = R/L$ is the aspect ratio.

The volume of the inner core of fluorescent ions, V_f, is found by dividing an image like **figure 6.7** Image II into slices with a width of one pixel. The radius, and hence the volume, of each disk is found by a threshold analysis and then summed up.

Finally, the volume of the outer component of non-fluorescent ions, V_{nf} is determined as the difference of the total crystal volume, V and the volume of fluorescent ions, V_f, that is, $V_{nf} = V - V_f$. Here we neglect the radial separation between the two components, which is a good approximation for ions of similar mass [147].

To convert the volume measurements from units of a cubic-pixel to a physical volume we calibrate the numbers with the known magnification of 4.0 of our imaging system and the pixel size of 9.9 μm $\times$ 9.9 μm. In order to determine the number of Mg^+ and MgH^+ ions, the volume occupied by each species is found from the images and multiplied by the ion density

$$n = \frac{2\varepsilon_0 M \omega_r^2}{Q^2}. \tag{6.9}$$

In all experiments in this chapter, the densities are held fixed at 10.2×10^4 mm^{-3} and 9.8×10^4 mm^{-3} for Mg^+ and MgH^+ ions respectively. Notice that the conversion from cubic-pixels to ion numbers does not influence the dissociation rates fitted in **section 6.3** or the relative drops measured in **section 6.4**. The volume

[3] In the case of ions with a larger relative mass difference the aspect ratio for a heavy (non-fluorescing) species should be calculated from the aspect ratio of a one-component crystal of the lighter fluorescing species using equation (5) in [148].

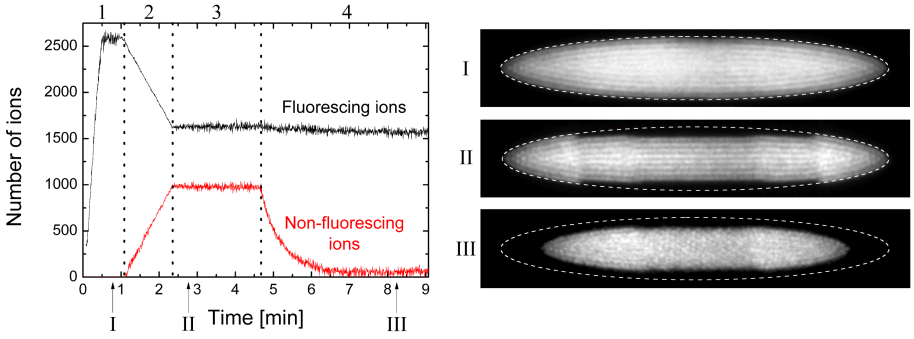

Figure 6.7 Number of Mg^+ and MgH^+ ions during the experimental procedure. The regions 1-4 correspond to the processes loading, molecule formation, equilibration and dissociation as described in **section 2.3** and **section 6.2.2 – 6.2.4**, respectively. The images I, II and III are snapshots of the Coulomb crystals at the times indicated on the graph. The horizontal direction corresponds to the z-axis of the trap.

determination is, however, compromised by other non-fluorescent ions as mentioned in **section 6.2.4**. The effect of these is accounted for in the data analysis

For a more detailed discussion of crystal volume determination methods, consult Ref. [149].

6.3 One-color photodissociation

In this section some of the results achieved with the one color dissociation scheme are presented. The experimental procedure is summarized in **figure 6.7**. First ions are loaded into the trap (region 1), then H_2 gas is leaked in and MgH^+ ions are formed (region 2). After the equilibration time (region 3), the molecular ions are dissociated by continuously applying the pulsed 281 nm laser (region 4). The rate at which molecular ions are dissociated, gives us information on the population in the probed level.

6.3.1 Determination of the dissociation rate of MgH^+ molecules

It turns out that the decay of the number of MgH^+ ions is well described by a biexponential decay. The rapidly decaying component corresponds to dissociation of MgH^+ found in the $X^1\Sigma^+(v = 0, J)$ state at the beginning of the dissociation process. The slowly decaying component is also due to dissociation from the $X^1\Sigma^+(v = 0, J)$ state, but of MgH^+ ions which are either found in other states

at the time when the dissociation laser is applied or MgH^+ ions transferred to other states, via excitation to the A state followed by spontaneous decay, and then transferred back to the $X^1\Sigma^+(v = 0, J)$ state. The rate for transfer back to the $X^1\Sigma^+(v = 0, J)$ state is effectively limited by the rate for pure rotational transitions within the $X^1\Sigma^+(v = 0)$ rotational levels. This process is responsible for the low dissociation rate, which typically leads to periods of a few minutes for the dissociation of all MgH^+ ions in a crystal as seen in **figure 6.7**, region 4. Due to ionization of residual gas molecules by the pulsed laser, we also need a linear term, that describes the loading of these unwanted ions. Thus, the molecular ion trace in region 4 is fitted with the following expression:

$$N_{\mathrm{nf}}(t) = N_{\mathrm{r}} e^{-\Gamma_{\mathrm{r}} t} + N_{\mathrm{s}} e^{-\Gamma_{\mathrm{s}} t} + \Gamma_{\mathrm{i}} t, \tag{6.10}$$

where Γ_{r} and Γ_{s} are the dissociation rates corresponding to the rapidly and slowly decaying components, respectively, N_{r} and N_{s} are constants, and Γ_{i} is the ionization rate of residual gas molecules.

Unfortunately, the intensity of the pulsed ns-laser has to be kept so low that the rapidly decaying component is hardly distinguishable; hence only Γ_{s} is considered below.

6.3.2 MgH^+ dissociation spectrum

Following the experimental procedure described in **sections 6.2.2** to **6.2.4** the dissociation rate Γ_{s} can now be determined while varying various parameters, such as the ns-laser pulse energy and frequency as well as the frequency and intensity of the PbSe diode laser. In order to determine if the PbSe diode laser cause any change in the rotational distribution, it is of interest to evaluate the dissociation rate from low lying rotational levels in the vibrational ground state of the X state. In **figure 6.8** the recorded spectrum of Γ_s with and without the lead salt diode laser is shown. Without applying the cooling laser, the R(3), R(4) and R(5) lines are clearly seen, and a slight asymmetry of the R(5) line reveal the presence of the P(1) line. The R(0) line is not visible and the R(1) line is unresolved from the R(2) line due to power broadening. When the cooling laser is applied, the spectrum clearly changes. R(5) is smaller, while the R(0) fills up the gap between R(4) and R(3). To understand the spectrum, however, numerical simulation of the entire spectrum had to be performed. This is done in the next section and enable us to give a more precise evaluation of the rotational distribution.

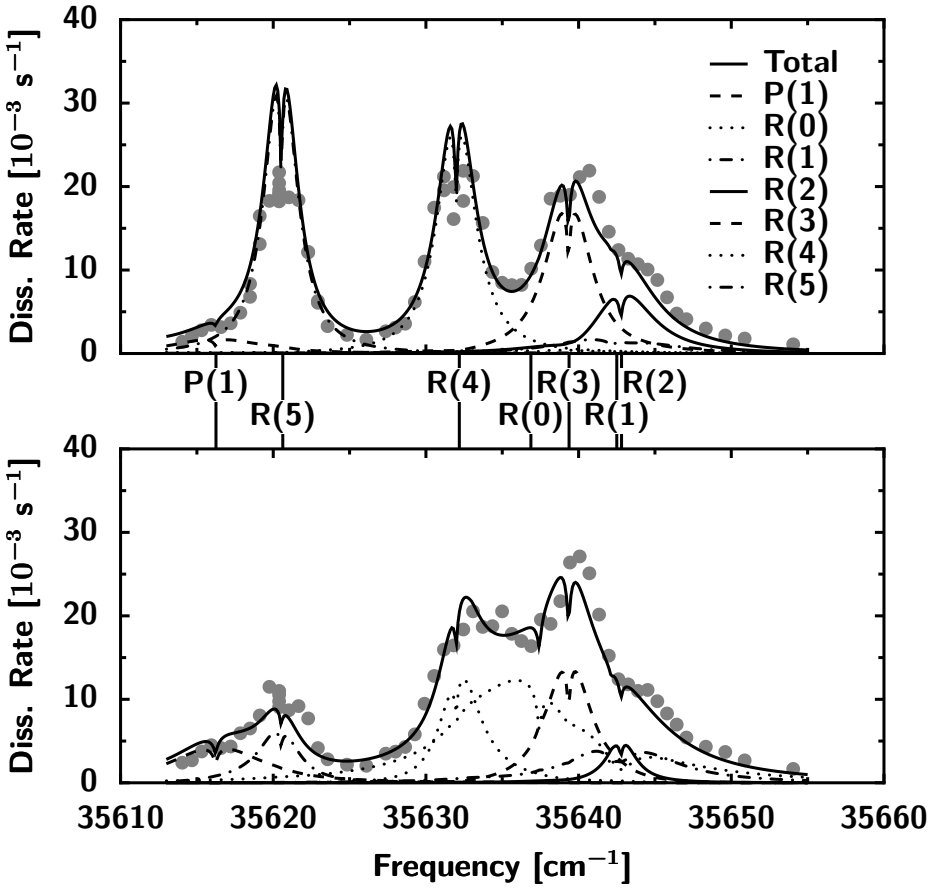

Figure 6.8 Dissociation spectrum of $^{24}MgH^+$ with (bottom) and without (top) applying the cooling laser. The grey circles is the measured rates, which have been corrected for a small variation in the dye laser power across the wavenumber range by a linear normalization to the dissociation rate at the R(4) line. The wavenumber is determined from the fundamental wavelength of the dye laser. A slight deviation between the observed and the predicted resonance frequencies due to the limited wavelength reproducibility of the dye laser and calibration precision was corrected for by shifting the axis by 1.6 cm^{-1}. The solid black line shows the spectrum according to the simulations described in **section 6.3.3**. The contribution of the different transitions to the simulated dissociation rate is indicated by dotted/dashed lines. There is a distinct difference between the two spectra, indicating that the cooling laser do have an effect of the population distribution. According to the simulations, the effect is huge on the population of the rotational ground state (dotted line), which is not immediately obvious from the measured rates, due to the broadness of the R(0) line.

6.3.3 Numerical simulation of the spectrum

In order to understand the spectrum presented in **figure 6.8**, numerical simulations including the photoexcitation via the X–A transition, photodissociation via the A–C transition induced by the pulsed laser, spontaneous decay A–X, rovibrational redistribution in the ground state potential due to the BBR field, as well as a possible coupling between rovibrational levels due to sympathetic cooling through long distance collisions with the laser cooled ions have been carried out (see **figure 6.9** (a) for an overview of the different levels and the coupling between them).

A full quantum mechanical treatment of the system, taking into account a basis set consisting of all rotational sub-states and laser light induced coherences, would give the best description, but would require impractically long computing times. As a consequence, we have chosen to simulate the dynamics of the molecules internal states by extending the model presented in **section 6.1.1.1** to include levels from both the X, A and C electronic state. The population vector now reads as $\vec{p} = [p_X(v = 0..5, J = 0..19), p_A(v = 0, J = 0..19), p_C,]$ and contains the populations of rovibrational levels $|v, J\rangle$ of the corresponding states X, A and dissociative continuum states in C. Its temporal evolution is governed by the coupling matrix $\boldsymbol{K}(t)$ through the matrix equation $\frac{d\vec{p}}{dt} = \boldsymbol{K}(t)\vec{p}(t)$. To avoid numerical integration of this system of equations, which is computationally expensive, the time line is split into intervals small enough that the rates in the entries of $\boldsymbol{K}(t)$ can be considered constant in each interval. As indicated in **figure 6.9** (b), the coupling matrix changes only during the ns-laser pulse, and the long period between pulses can be treated as a single time step. Consequently, the temporal evolution of the system can be found through the solutions of the linear ordinary differential equations for each interval:

$$\frac{d\vec{p}}{dt} = \boldsymbol{K}_i\vec{p}(t) \qquad \Rightarrow \qquad \vec{p}(t_{i+1}) = \exp(\boldsymbol{K}_i(t_{i+1} - t_i))\vec{p}(t_i), \tag{6.11}$$

with the total solution being:

$$\vec{p}(M) = \left[\prod_{i=0}^{N-1} \exp(\boldsymbol{K}_i(t_{i+1} - t_i))\right]^M \vec{p}(0), \tag{6.12}$$

where N is the number of intervals and M is the number of pulses. The various coupling rates in $\boldsymbol{K}$ are determined in the following subsections. Since the dissociation rate from C is much faster than spontaneous decay back to A or X, p_C represents the amount of dissociated MgH^+ ions.

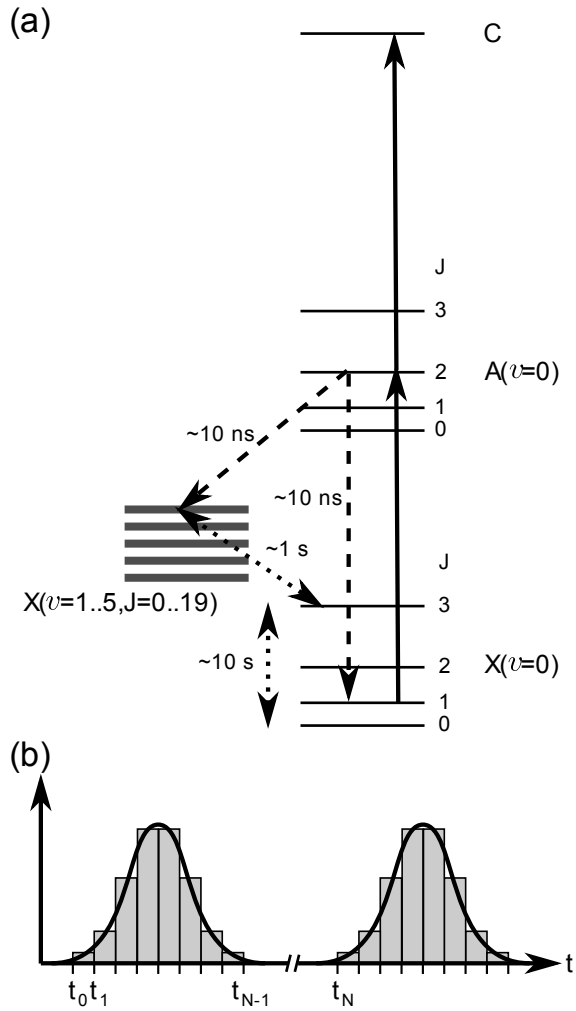

Figure 6.9 (a) Reduced level diagram of MgH^+ showing transitions and typical timescales. Full arrows: transitions induced by the pulsed laser, i.e. photoexcitation from the electronic ground state X to the excited level A and photodissociation from the excited state A to the dissociative state C. Dashed arrows: spontaneous decay from A to rovibrational levels in X. Dotted arrows: rovibrational redistribution within the electronic ground state X due to interactions with a 300 KBBR field. (b) In the simulation, the timeline is split into N intervals, each one small enough that the coupling rates can be considered constant in each interval.

6.3.3.1 Photoexcitation $X - A$

As a starting point for our approximation of the photoexcitation rate, we first con-

sider the Rabi oscillations induced between two levels $|v = 0, J\rangle_x$ and $|v = 0, J'\rangle_A$ by the pulsed laser in the dipole approximation as described in, for example, [150].

In order to calculate the Rabi frequency, we need the matrix element $\langle\phi_1|\boldsymbol{d}\cdot\boldsymbol{r}|\phi_0\rangle$, where $\boldsymbol{d}$ dipole moment operator, and phi_0 and ϕ_1 are the initial and final states. Ignoring spin-related effects, a simple diatomic molecule can be modelled as a idealized vibrating symmetric top, in which case it can be described by the quantum numbers $|evJKM\rangle$, where e is the electronic quantum number, v is the vibrational quantum number, J is the rotational quantum number, M is magnetic quantum number and K is the projection of the angular momentum along the molecular symmetry axis [129]. The matrix element in this case reduces to [151]:

$$\begin{aligned}|\langle e_2v_2J_2K_2M_2|\epsilon\cdot\boldsymbol{r}|e_1v_1J_1K_1M_1\rangle|^2 = \;& S_q^{\text{geom}}(J_2M_2;J_1M_1)\\ &\times S^{\text{HL}}(J_2K_2;J_1K_1)\\ &\times S^{\text{FC}}(e_2v_2;e_1v_1)\\ &\times|\langle e_2J_2\|d\|e_1J_1\rangle|^2 \end{aligned}\tag{6.13}$$

Here the geometric factor contains the information about molecular orientation in the laboratory frame and is expressible as the square of a Wigner 3j symbol [152]

$$S_q^{\text{geom}}(J_2M_2;J_1M_1) = \begin{pmatrix} J_2 & 1 & J_1\\ -M_2 & q & M_1\end{pmatrix}^2,\tag{6.14}$$

where q is the polarization of the light field. In our case the Hönl-London factor is simply given by $S^{\text{HL}}(J_1+1;J_1) = J_1+1$ and $S^{\text{HL}}(J_1-1;J_1) = J_1$ for R and P type transitions, respectively [153].

The Rabi frequency is now given by

$$\chi_{J,J\pm1}(t) = \frac{\mu_{XA}\sqrt{S^{\text{FC}}(A0;X0)S^{\text{HL}}(J;J\pm1)S^{\text{geom}}(JM;J\pm1M+q)}}{\hbar}E(t),$$

where μ_{XA} is the transition dipole moment between X and A, and $E(t)$ is the electric field amplitude of the pulsed laser at time t. The generalized Rabi frequency is written as

$$\Omega_{J,J\pm1}(t) = \sqrt{\chi_{J\pm1}(t)^2+\Delta^2_{J,Jo\pm1}},$$

where $\Delta_{J,J\pm1}$ is the detuning of the pulsed laser frequency with respect to the transition frequency between the two levels. Since the Rabi oscillation period is much shorter than the pulse length, the Rabi oscillations (which cannot be described by rate equations) are modelled by introducing coupling rates for absorption and

emission which give rise to a steady state population equal to the time averaged population of the Rabi oscillations. It is natural to assume coupling rates of the order of the generalized Rabi frequency, Ω, times the peak-to-peak amplitude of the Rabi oscillation, $\frac{\chi^2_{J,J\pm1}}{\Omega^2_{J,J\pm1}}$, since with this assumption population transfers take place on the same time scale as one Rabi oscillation. To reach the desired steady state population, the absorption rate is scaled with a coefficient

$$C_{J,J\pm1} = \frac{\Omega^2_{J,J\pm1}}{2(\Omega^2_{J,J\pm1} + \Delta^2_{J,J\pm1})},$$

and the emission rate by $1 - C$. The entries in the coupling matrix $\boldsymbol{K}$ are then given by

$$\Gamma^{abs}_{v,J;v',J\pm1} = \frac{\chi^2_{J,J\pm1}\Omega^2_{J,J\pm1}}{2(\Omega^2_{J,J\pm1} + \Delta^2_{J,J\pm1})},$$

and

$$\Gamma^{em}_{v,J;v',J\pm1} = \frac{\chi^2_{J,J\pm1}(\Omega^2_{J,J\pm1} + 2\Delta^2_{J,J\pm1})}{2(\Omega^2_{J,J\pm1} + \Delta^2_{J,J\pm1})},$$

for absorption and emission, respectively.

Since the laser light is linearly polarized, the selection rule $\Delta m_J = 0$ prevents the probing of the sublevels $m_J = J$ and $m_J = -J$ on $P(J)$ transitions. To account for this in the simulations, the dissociation rate on $P(j)$ transitions are scaled by the factor $\frac{2J-1}{2J+1}$.

6.3.3.2 Photodissociation $A \rightarrow C$

As mentioned in **section 6.2.4.1**, numerical calculations based on a wavepacket approach [145] show that, within the wavelength range of 560-563 nm, the dissociation rate is almost independent of both the pulsed laser frequency and the rovibrational state in A, while it depends linearly on the laser intensity. That is,

$$\Gamma_{\text{diss}} = \alpha I_{peak},$$

where I is the intensity of the pulsed laser and α is of the order of 1 s^{-1} W^{-1} cm^2. Due to the limited accuracy of the calculation, α is taken as a free parameter in the fit to the observed dissociation spectrum.

6.3.3.3 Spontaneous decay $A \rightarrow X$

From the mean lifetime, τ_A, of the excited state, the rate of spontaneous decay from $|v, J\rangle_A$ to i$|v', J \pm 1\rangle_X$ is approximated by

$$\Gamma_{v,J;v',J\pm1} = \frac{S^{\mathrm{FC}}(v, v')}{\tau_A} \frac{S^{\mathrm{HL}}(J, J \pm 1)}{S^{\mathrm{HL}}(J, J+1) + S^{\mathrm{HL}}(J, J-1)},$$

where $S^{\mathrm{FC}}(v, v')$ is the Franck-Condon overlap between the two vibrational levels and $S^{\mathrm{HL}}(J, J \pm 1)$ is the Hönl-London factor. The lifetime has been calculated to be $\tau_A = 4.4$ ns [145], while Franck-Condon factors derived from molecular spectroscopy are tabulated in [142]. Since more than 99.9 % of the population decays back into the $v = 0 \ldots 5$ levels of the X state, in the simulations the vibrational distribution has been truncated above $v = 5$.

6.3.3.4 Rovibrational redistribution in X due to BBR

The rovibrational redistribution in the electronic ground state due to blackbody radiation is modeled in the same way as the previously described cooling simulations in **section 6.1.1.1**.

From the Einstein coefficients, coupling rates are found by assuming a 300 K BBR background, $W(\omega_{ij})$, using

$$\Gamma_{v,J;v',J\pm1} = A_{v,J;v',J\pm1} + B_{v,J;v',J\pm1} W(\omega_{v,J;v',J\pm1})$$

6.3.4 Interpretation of spectrum

To match the simulated spectrum to the experimentally recorded spectrum shown in **figure 6.8** two parameters are varied. First, the pulsed laser intensity is adjusted to match the observed widths of the various transitions. Second, the dissociation proportionality constant, α, is adjusted to match the observed dissociation rate. Overall, the spectrum fits well, but there is a discrepancy on the R(5) line, that is not easily explained.

To visualize what is happening, the amount of molecules dissociating through the different transitions is indicated by the dashed and dotted lines. This reveals a much bigger difference between the two spectra than directly seen. The contribution from the R(0) is negligible in the spectra recorded with the uncooled population distribution, while it is prominent in the spectrum from the cooled population distribution. Because of the broadness of this line, however, this is not

immediately apparent from the experimentally observable result. The above spectra was simulated with full cooling, e.g. 64% of the population in the ground state. As we will see in the next section, this is actually not the case. If we modify the Einstein coefficients in the same way as we argue in **section 6.4.2**, the simulated cold spectrum still fits very well, even though this corresponds to only 37% on the population in the ground state. Unfortunately, this also implies that this probing scheme is not very sensitive to changes in the population of the $|v = 0, J = 0\rangle$ state.

An interesting feature of both the recorded and the simulated spectra is the drop in dissociation rate when the pulsed laser in on resonance with the transitions. This is observed on all R-lines from $J = 3$ to 8. With the laser on resonance, the first part of the pulse is sufficiently intense to saturate the $X \rightarrow A$ transition, but the intensity is still so low that spontaneous decay back into various vibrational levels of X greatly dominates over dissociation via the C state. If the laser is off resonant, population is not transfered efficiently to the A state until later in the pulse, where the $A \rightarrow C$ dissociation rate has also increased. Ideally, the dissociation pulse should arrive 3 ns before the excitation pulse, such that it has maximum when the population transfer in the first step is maximal. Here, the steps are however performed by the same pulse and the temporal overlap is not optimal with respect to the number of dissociated molecules. A similar effect was observed in Ref. [146], with a molecular beam crossing a cw laser beam.

6.4 Two-color photodissociation

Figure 6.10 shows the experimental procedure for the two color photodissociation scheme. As in the one color scheme, Mg^+ ions are first loaded into the trap (region 1). Then molecular ions are formed and equilibrated with the BBR field, and optionally manipulated by the cooling laser (region 2 and 3). Finally, in the two color scheme, the MgH^+ ions are state-selectively dissociated by simultaneously applying a *single* 281 nm pulse and a *single* 266 nm pulse. As shown in **figure 6.10** this results in a sudden loss of molecular ions. The height of the step is proportional to the population of the particular rotational state being addressed.

The pulse energies are 5 μJ and 1 mJ for the 281 nm and the 266 nm pulses, respectively, which is enough to dissociate more than 90% of the MgH^+ ions in the rotational state addressed by the tunable 281 nm laser. The off-resonant contribution from other levels is found to less than 2%. Only the R(1) and R(2) transitions are so closely spaced, that resolving them is problematic. The populations of the $|v = 0, J = 1\rangle$ and $|v = 0, J = 2\rangle$ states can, however, easily be probed on the P(1) and P(2) transitions, but must in this case be corrected by a factor of $\frac{2J-1}{2J+1}$ as only

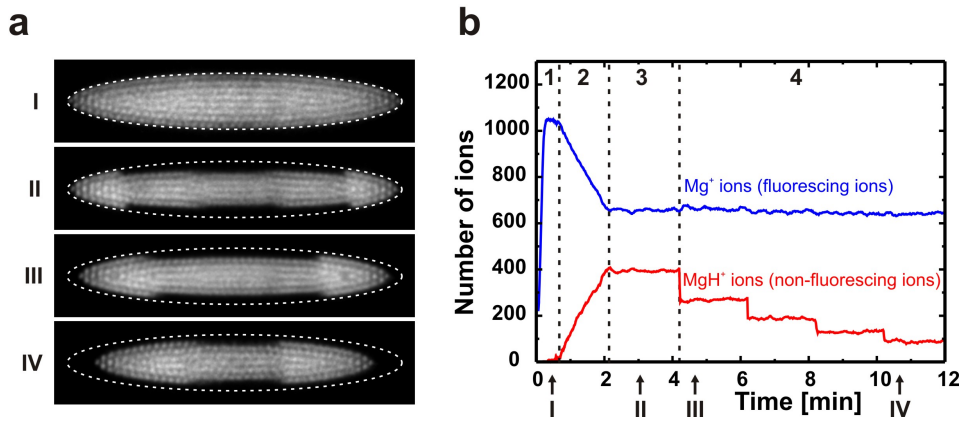

Figure 6.10 Number of Mg^+ and MgH^+ ions during the experimental procedure. The regions 1-4 correspond to the processes loading, molecule formation, equilibration and dissociation as described in **section 2.3** and **section 6.2.2** – **6.2.4**, respectively. The images I, II, III and IIII are snapshots of the Coulomb crystals at the times indicated on the graph. The horizontal direction corresponds to the z-axis of the trap.

some sublevels are probed as described in **section 6.3.3.1**. The combination of essentially perfect rotational level selectivity and close to 100% dissociation probability in a single REMPD event provides a direct measure of the rotational state distribution at any chosen instant.

To test that both the 281 nm and the 266 nm is saturated, both pulse powers have been varied individually, while probing the population of the $|v = 0, J = 0\rangle$ state when the cooling laser was applied. In both cases the variation in dissociation efficiency was almost constant around the range of the power used.

6.4.1 Rotational distribution

With the above procedure the rotational population distribution can now be probed with and without the cooling laser present. The result, which has been corrected for off-resonant dissociation by the 266 nm light, is presented in **figure 6.11**. First note the excellent agreement between the uncooled distribution and that of a thermal distribution. This demonstrates the validity of our probing scheme. A further confirmation is the fact that the total population in the different levels summed up to about 90% of the total number of the ions, with an uncertainty of only $\approx 5\%$. Some of the the 5% may in fact reside in higher non-probed states.

The cooled distribution shows a pronounced accumulation of population in the two lowest rotational states, with $37 \pm 2\%$ in the $|v = 0, J = 0\rangle$ state and $17 \pm 2\%$

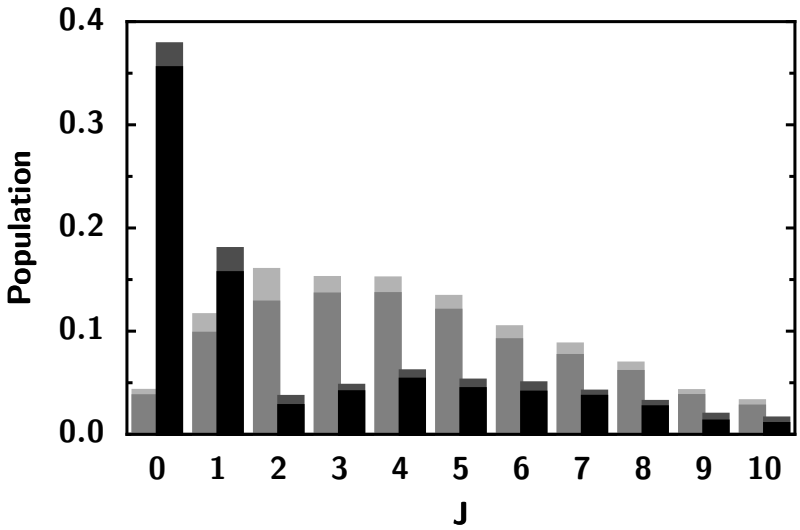

Figure 6.11 Deduced rotational state distributions obtained by the two color 1+1 REMPD scheme. The grey bars indicate the distribution without applying the cooling laser and the black bars indicates the distribution after a cooling period of 2 min. All levels except for the $|v = 0, J = 1\rangle$ and the $|v = 0, J = 2\rangle$, which are not spectroscopically resolvable, where probed on their R-transitions. Instead the $|v = 0, J = 1\rangle$ and $|v = 0, J = 2\rangle$ states were dissociated through the P-transition and multiplied by a factor of 3 and 5/3, respectively, to correct for non-probed sub-levels. All bars are averaged over typically 15 measurements and the shaded areas indicates the standard deviation.

in the $|v = 0, J = 1\rangle$ state. The rest of the population is distributed over the $|v = 0, J \geq 2\rangle$ levels, with at most 6% in a single level. The amount of population in the rotational ground state is equivalent to that of a 21 ± 2 K thermal population. The simulated value of 64% is, however, not reached. This discrepancy cannot easily be explained. Experimentally, we have tested that the cooling transition really is saturated, as seen in **figure 6.12**. By varying the pressure in the vacuum chamber, we have checked that collisions with background gas particles does not have an influence. Various possible heating sources have been turned off, e.g. ceiling light, atomic ovens, ion gauge, without any observable effect in the cooled $|v = 0, J = 0\rangle$ population, but these heating test was performed with the one color scheme and should be repeated with the two color scheme. However, any heating should also be visible in the uncooled population distribution. The good agreement in this distribution, bounds any heating rate to $0.03\ \mathrm{s}^{-1}$; a heating rate that would only reduce the $|v = 0, J = 0\rangle$ population to 57%, according to model simulations. A potential reason for the observed difference between the measurements and the modeled values is errors in the calculated values of the transition rates.

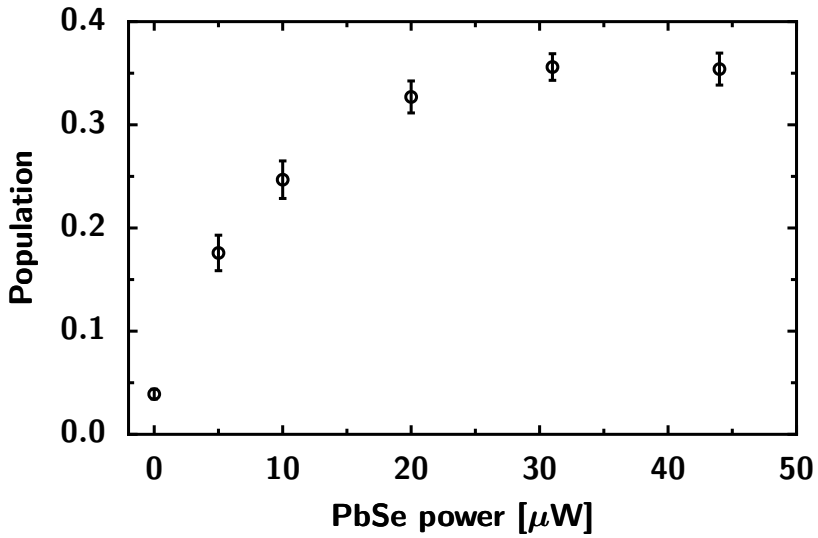

Figure 6.12 Population in the $|v = 0, J = 0\rangle$ ground state as a function of the cooling laser intensity. The $|v = 0, J = 2\rangle$ – $|v = 1, J = 1\rangle$ transition is seen to saturate, but not with big a margin. All other measurements in this chapter was made with maximum intensity.

6.4.2 Temporal evolution of the population

Not only can we probe the steady state population distributions, but also the temporal evolution of the population in different levels. In **figure 6.13** the observed population in $|v = 0, J = 0\rangle$ is plotted as a function of the cooling time. The results have the same shape as the theory presented in **figure 6.2**, however, there is a large descrepancy in the final steady state population as already seen in the previous section.

However, if we start out with the cooled distribution from **figure 6.11** and let the ions equililbrate with the BBR field again, we clearly see that the timescale for heating is not correct (solid line in **figure 6.14**). As we have already ruled out any additional heating sources, since these would alter the uncooled equilibrium distribution as well, which does not seem to be the case, this again suggest that our model, or the input parameters to the model is not correct. The correct timescale for the heating of the molecular ions can be achieved if all the Einstein coefficients in the vibrational ground state are multiplied by a factor of two. If we furthermore multiply the rates between vibrational levels with a factor of 0.22, the simulation agrees very well with the time evoultion of the population for both the heating and cooling scenario (dashed lines in **figure 6.13** and **figure 6.14**).

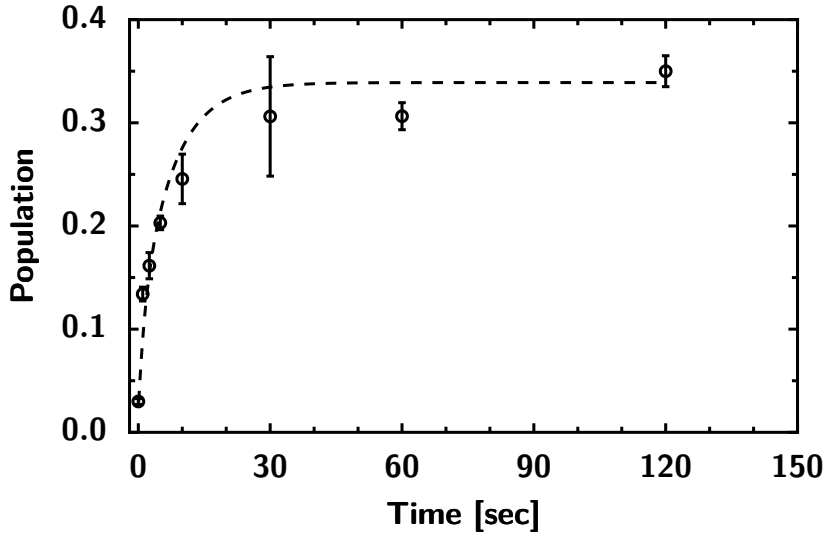

Figure 6.13 Temporal evolution of the population in the $|v = 0, J = 0\rangle$ state during laser cooling. The population saturates after ca one minute. The dashed line is a theoretical calculation, where the Einstein coefficients has been modified according to the discussion in **section 6.4.2**.

The simulated steady state distribution when we modify the Einstein coefficients is presented in **figure 6.15**. Although not a perfect fit, they are suggestive that this may be the right approach.

To test this experimentally, one could deplete a given |v=0, J ⟩ state and measure how fast the population flows back into this state. If this was done for the lowest 10 rotational state, the Einstein coefficients could be experimentally verified.

6.5 Conclusion and outlook

In conclusion, we have demonstrated a very efficient technique for determining the rotational population distribution of MgH^+ ions via a two color 1+1 REMPD scheme. We have used this technique to experimentally demonstrate significant laser cooling of the molecular ions towards their rotational ground state with only a single optical pumping field. The percentage of molecules in the ground state could be further improved, by subsequently applying some sort of filtering. We could, for example, remove all the molecules in the $|v = 0, J = 1\rangle$ state by applying a single 266 + 281 nm pulse. In this case 45% of the molecular ions left would be in

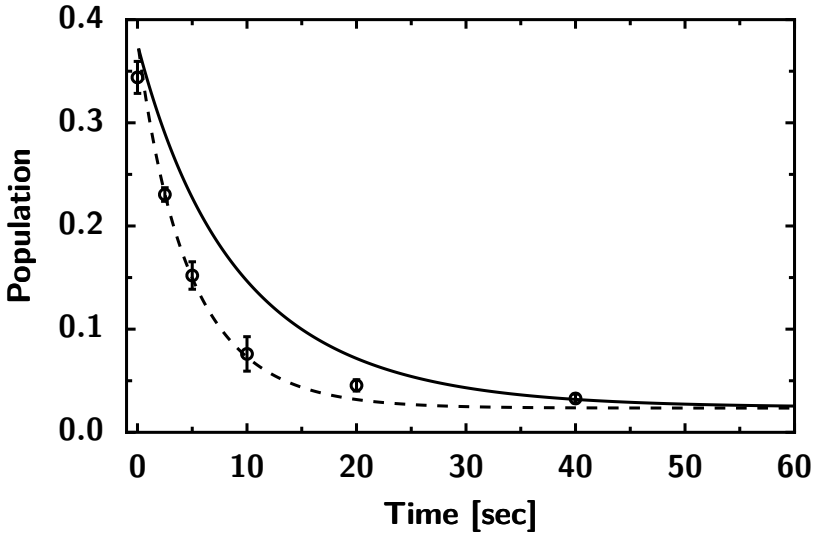

Figure 6.14 The temporal evolution of the population in the $|v = 0, J = 0\rangle$ state in the time after the cooling laser has been blocked. The solid line is the simulated behaviour with the Einstein coefficients from **section 6.1.1.1**, while the dashed line is a simulation with modified Einstein coefficients as discussed in **section 6.4.2**.

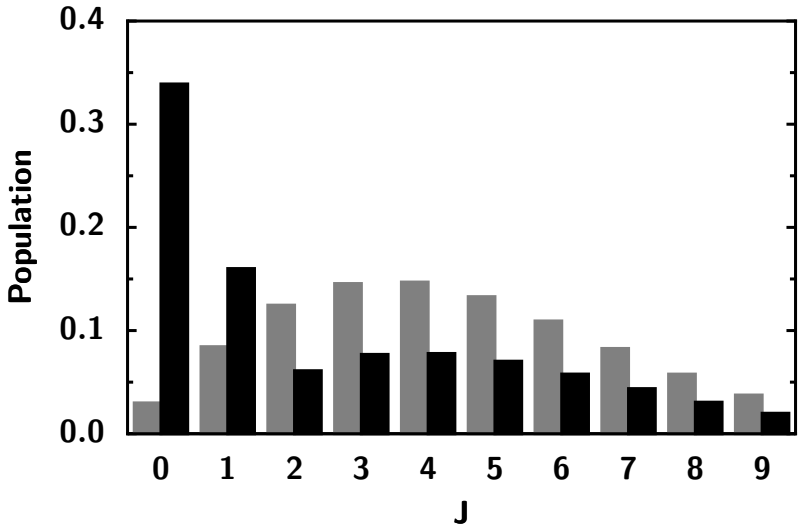

Figure 6.15 Simulation of the cooled population distribution where the Einstein coefficients in the vibrational ground state has been multiplied by 2 and the intervibrational rates have been multiplied by 0.22.

the $|v = 0, J = 0\rangle$ ground state. It should be straightforward to extend the cooling scheme by applying additional laser sources and incoherent radiation fields [46] either to speed up the cooling rate, to increase population the ground state or to prepare the molecular ions in other states [154, 155].

Both the rotational cooling schemes and the detection scheme may furthermore be applied to single molecular ions [37, 41] and possibly even to appropriately chosen complex molecular ions [39, 40]. In the latter case, since the rovibrational modes are typically coupled, relatively efficient rovibrational cooling schemes may be feasible by addressing only a single or a few rovibrational transitions.

Chapter 7

Summary

In this thesis we have presented a mass spectrometric technique, SCSI-MS, that relies on the measurement of the normal mode frequencies of strongly-coupled two-ion systems. The strongly-coupled regime is reached by sympathetic cooling of the ion of interest (the unknown ion) through the Coulomb interaction with a simultaneously-trapped and laser-cooled atomic ion. Even without optimizing the current setup for SCSI-MS, we have obtained a relative mass resolution of $\approx 10^{-4}$. The technique is inherently a single ion mass spectrometric technique, utilizing a non-destructive detection step. This latter feature was utilized in a study of the photofragmentation pathways of aniline. The single ion aspect of such studies enables one not only to obtain an ensemble-averaged result, but instead presents the opportunity for comparing individual ion *histories*. Complementary, one could imagine how the SCSI-MS technique could be used to monitor the build-up of complex molecules through consecutive reaction processes.

Other attractive features of SCSI-MS due to the single ion aspect, include a very high reaction detection efficiency of almost 100% and an extremely pure target, since ensemble averaging is avoided. Hence only about 250 reactions reactions between Mg^+ in the $3p\,^2P_{3/2}$ excited state and HD molecules at thermal energies was enough to claim a branching ratio of more than 5 in favor of forming MgD^+ to MgH^+. Potentially, chemistry studies of exotic reactions including e.g. superheavy elements, could benefit greatly from this technique.

In the last part of the thesis we turned our focus to the internal states of the molecular ions. We showed how the internal degrees of freedom of the ions are in general in equilibrium with the BBR field of 300 K. Then we went on and altered the rotational population distribution by implementing a simple optical pumping cooling scheme involving only a single cw laser. In this way a 15 fold increase of the population in the rotational ground state was achieved. The final population of 37% corresponds to that of a Boltzmann distribution at a temperature of 21 K, suggesting that cold molecular ion experiments can now be performed at cryogenic temperatures in a room temperature experimental setup. Several improvements of the cooling scheme are already proposed, including subsequent filtering (e.g. removal of the $|v = 0, J = 1\rangle$ state population) or the implementation of lamps and additional lasers to speed up the cooling process or achieve other population distributions. The cooling scheme may furthermore be applied to single molecular ions and possibly even to appropriately chosen complex molecular ions.

Appendix A

The Ca^+ ion

A.1 Abundance of Ca-isotopes

Isotope	Abundance [156]
40	96.941 %
42	0.647 %
43	0.135 %
44	2.086 %
46	0.004 %
48	0.187 %

A.2 Cooling transitions in $^{40}Ca^+$

	$^{40}Ca^+$
$\lambda^{(\text{air})}_{4s\,^2S_{1/2}\leftrightarrow 4p\,^2P_{1/2}}$ [nm] [157]	396.8469
$\lambda^{(\text{vacuum})}_{4s\,^2S_{1/2}\leftrightarrow 4p\,^2P_{1/2}}$ [nm] [157]	396.9591
$\lambda^{(\text{air})}_{4p\,^2P_{1/2}\leftrightarrow 3d\,^2D_{3/2}}$ [nm] [157]	866.214
$\lambda^{(\text{vacuum})}_{4p\,^2P_{1/2}\leftrightarrow 3d\,^2D_{3/2}}$ [nm] [157]	866.252
$4p\,^2P_{1/2}$ Radiative lifetime [ns][158]	7.07
$3d\,^2D_{3/2}$ Radiative lifetime [s] [157]	0.77
$4s\,^2S_{1/2} \leftrightarrow 4p\,^2P_{1/2}$ Line width [MHz]	$2\pi \times 22.5$

Appendix B

The Mg^+ ion

B.1 Atomic data for neutral magnesium

	^{24}Mg	^{25}Mg	^{26}Mg
Abundance [%] [156]	78.992	10.003	11.005
Atomic mass [u]	23.985042	24.985837	25.982594
Nuclear spin	0	5/2	0
$\lambda^{(\text{air})}_{3s^2\,{}^1S_0 \leftrightarrow 3s3p\,{}^1P_1}$ [nm] [157]	285.21261	-	-
$\lambda^{(\text{vacuum})}_{3s^2\,{}^1S_0 \leftrightarrow 3s3p\,{}^1P_1}$ [nm] [157]	285.29642	-	-
$3s3p\,{}^1P_1$ Radiative lifetime [ns] [159]	2.0	-	-
$3s^2\,{}^1S_0 \leftrightarrow 3s3p\,{}^1P_1$ Line width [MHz][157]	$2\pi \times 80$	-	-
$3s^2\,{}^1S_0 \leftrightarrow 3s3p\,{}^1P_1$ Isotope shift [GHz] [160]	-	0.73	1.41

B.2 Cooling transitions in $^{24}Mg^+$

	$^{24}Mg^+$
$\lambda^{(\text{air})}_{3s\,{}^2S_{1/2} \leftrightarrow 3p\,{}^2P_{3/2}}$ [nm] [157]	279.5528
$\lambda^{(\text{vacuum})}_{3s\,{}^2S_{1/2} \leftrightarrow 3p\,{}^2P_{3/2}}$ [nm] [157]	279.6352
$3p\,{}^2P_{3/2}$ Radiative lifetime [ns] [161]	3.810
$3s\,{}^2S_{1/2} \leftrightarrow 3p\,{}^2P_{3/2}$ Line width [MHz]	$2\pi \times 41.773$

Appendix C

The MgH^+ ion

C.1 Transitions in the MgH^+ ion

Transition	Wavenumber [cm^{-1}]	Wavelength [μm]	Frequency [THz]
$R_0(0)$	12.59	794.53	0.378
$R_0(1)$	25.16	397.54	0.755
$R_0(2)$	37.82	264.43	1.135
$R_0(3)$	50.19	199.23	1.506
$R_0(4)$	62.85	159.12	1.885
$R_0(5)$	75.22	132.95	2.256
$R_0(6)$	87.66	114.07	2.630
$R_0(7)$	99.95	100.05	2.999
$R_0(8)$	112.30	89.05	3.369
$R_0(9)$	124.45	80.35	3.734

Table C.1 Transitions within the vibrational ground state of the electronic ground state of MgH^+ [142].

Transition	Wavenumber [cm^{-1}]	Wavelength [μm]	Frequency [THz]
$P_1(5)$	1568.03	6377.45	47.041
$P_1(4)$	1582.06	6320.89	47.462
$P_1(3)$	1595.56	6267.41	47.867
$P_1(2)$	1608.96	6215.19	48.269
$P_1(1)$	1621.77	6166.11	48.653
$R_1(0)$	1646.70	6072.74	49.401
$R_1(1)$	1658.53	6029.44	49.756
$R_1(2)$	1670.07	5987.79	50.102
$R_1(3)$	1681.07	5948.61	50.432
$R_1(4)$	1691.86	5910.67	50.756

Table C.2 Transitions going from $v = 0$ to $v = 1$ in the electronic ground state of MgH^+ [142]. The $P_1(2)$ transition is used for the cooling scheme in **chapter 6**.

Transition	Wavenumber [cm^{-1}]	Wavelength [μm]	Frequency [THz]
$P_4(10)$	5938.82	1683.84	178.165
$P_4(9)$	5964.78	1676.51	178.943
$P_4(8)$	5989.34	1669.63	179.680
$P_4(7)$	6012.34	1663.25	180.370
$P_4(6)$	6034.08	1657.25	181.022
$P_4(5)$	6054.20	1651.75	181.626
$P_4(4)$	6073.00	1646.63	182.190
$P_4(3)$	6090.02	1642.03	182.701
$P_4(2)$	6105.73	1637.80	183.172
$P_4(1)$	6119.81	1634.04	183.594
$R_4(0)$	6143.47	1627.74	184.304
$R_4(1)$	6153.00	1625.22	184.590
$R_4(2)$	6161.01	1623.11	184.830
$R_4(3)$	6167.24	1621.47	185.017
$R_4(4)$	6172.14	1620.18	185.164

Table C.3 Transitions going from $v = 0$ to $v = 4$ in the electronic ground state of MgH^+ [142]. A InP diode laser that covers the wavelength range 1620–1675 nm is currently under construction in the laboratory. With this new laser, further manipulations of the population distribution becomes possible [155].

C.2 Einstein A coefficients

$\lvert v, J\rangle_{\text{ini}}$		$\Delta v =$	0	-1		-2		-3		-4
v	J	$\Delta J =$ -1	1	-1	1	-1	1	-1	1	-1
	0									
	1	0.002								
	2	0.022								
	3	0.078								
0	4	0.191								
	5	0.381								
	6	0.665								
	7	1.062								
	8	1.589								
	0		20.565							
	1	7.886	12.773	0.002						
	2	10.141	10.705	0.019						
	3	11.636	9.490	0.068						
1	4	12.914	8.586	0.167						
	5	14.123	7.843	0.333						
	6	15.323	7.203	0.581						
	7	16.541	6.637	0.927						
	8	17.793	6.129	1.387						
	0		2.804		46.551					
	1	0.843	1.959	17.651	29.081	0.002				
	2	0.955	1.842	22.575	24.519	0.016				
	3	0.962	1.828	25.765	21.870	0.059				
2	4	0.934	1.846	28.446	19.910	0.144				
	5	0.890	1.877	30.953	18.303	0.287				
	6	0.837	1.915	33.418	16.917	0.502				

Table C.4.a Einstein A coefficient for transitions within the electronical ground state of MgH^+ as calculated by Level [141]. See **section 6.1.1.1** for more information on the calculation details.

	7	0.780	1.956	35.902	15.690	0.801				
	8	0.720	1.997	38.439	14.585	1.197				
	0		0.679		6.296		76.854			
	1	0.217	0.461	1.860	4.430	28.871	48.240	0.001		
	2	0.255	0.423	2.087	4.191	36.758	40.866	0.014		
	3	0.267	0.410	2.079	4.181	41.766	36.628	0.050		
3	4	0.271	0.405	1.993	4.244	45.910	33.509	0.123		
	5	0.270	0.404	1.872	4.336	49.742	30.957	0.245		
	6	0.268	0.405	1.734	4.441	53.474	28.755	0.428		
	7	0.264	0.408	1.586	4.551	57.209	26.800	0.682		
	8	0.259	0.410	1.435	4.661	61.001	25.037	1.020		
	0		0.050		2.655		8.667		109.560	
	1	0.016	0.034	0.849	1.805	2.496	6.163	40.846	69.034	0.001
	2	0.019	0.031	0.996	1.656	2.757	5.887	51.807	58.706	0.012
	3	0.020	0.030	1.043	1.605	2.698	5.922	58.644	52.819	0.042
4	4	0.020	0.029	1.056	1.588	2.535	6.055	64.220	48.505	0.104
	5	0.020	0.029	1.053	1.586	2.327	6.227	69.320	44.979	0.206
	6	0.020	0.029	1.042	1.591	2.098	6.413	74.245	41.936	0.359
	7	0.020	0.029	1.025	1.600	1.861	6.604	79.138	39.231	0.573
	8	0.020	0.029	1.004	1.612	1.622	6.791	84.073	36.783	0.856

Table C.4.b Einstein A coefficient for transitions within the electronical ground state of MgH^+ as calculated by Level [141]. See **section 6.1.1.1** for more information on the calculation details.

References

[1] S. Schiller and V. Korobov. Tests of time independence of the electron and nuclear masses with ultracold molecules. *Phys. Rev. A*, 71(3):032505, 2005.

[2] M. Kajita. Prospects of detecting m_e/m_p variance using vibrational transition frequencies of $^2\Sigma$-state molecules. *Phys. Rev. A*, 77(1):012511, 2008.

[3] J. J. Hudson, B. E. Sauer, M. R. Tarbutt and E. A. Hinds. Measurement of the Electron Electric Dipole Moment Using YbF Molecules. *Phys. Rev. Lett.*, 89(2):023003, 2002.

[4] E. R. Hudson, H. J. Lewandowski, B. C. Sawyer and J. Ye. Cold Molecule Spectroscopy for Constraining the Evolution of the Fine Structure Constant. *Phys. Rev. Lett.*, 96(14):143004, 2006.

[5] D. DeMille. Quantum Computation with Trapped Polar Molecules. *Phys. Rev. Lett.*, 88(6):067901, 2002.

[6] S. A. Rice and M. Zhao. *Optical control of molecular dynamics*. John Wiley & Sons, New York, 2000.

[7] M. Shapiro and P. Brumer. *Principles of the Quantum Control of Molecular Processes*. John Wiley & Sons, New York, 2003.

[8] S. Willitsch, M.T. Bell, A.D. Gingell and T.P. Softley. Chemical applications of laser-and sympathetically-cooled ions in ion traps. *Phys. Chem. Chem. Phys.*, 10(48):7200, 2008.

[9] R. V. Krems. Cold controlled chemistry. *Phys. Chem. Chem. Phys.*, 10(28):4079, 2008.

[10] S. Jochim, M. Bartenstein, A. Altmeyer, G. Hendl and S. Riedl *et al.* Bose-Einstein Condensation of Molecules. *Science*, 302(5653):2101, 2003.

[11] M. Greiner, C.A. Regal and D.S. Jin. Emergence of a molecular Bose-Einstein condensate from a Fermi gas. *Nature*, 426(6966):537, 2003.

[12] J. T. Bahns, W. C. Stwalley and P. L. Gould. Laser cooling of molecules: A sequential scheme for rotation, translation, and vibration. *J. Chem. Phys.*, 104(24):9689, 1996.

[13] M. D. Di Rosa. Laser-cooling molecules. *Eur. Phys. J. D*, 31(2):395, 2004.

[14] P. D. Lett, K. Helmerson, W. D. Phillips, L. P. Ratliff and S. L. Rolston *et al.* Spectroscopy of Na_2 by photoassociation of laser-cooled Na. *Phys. Rev. Lett.*, 71(14):2200, 1993.

[15] J. D. Miller, R. A. Cline and D. J. Heinzen. Photoassociation spectrum of ultracold Rb atoms. *Phys. Rev. Lett.*, 71(14):2204, 1993.

[16] A. Fioretti, D. Comparat, A. Crubellier, O. Dulieu and F. Masnou-Seeuws *et al.* Formation of Cold Cs_2 Molecules through Photoassociation. *Phys. Rev. Lett.*, 80(20):4402, 1998.

[17] A. N. Nikolov, E. E. Eyler, X. T. Wang, J. Li and H. Wang *et al.* Observation of Ultracold Ground-State Potassium Molecules. *Phys. Rev. Lett.*, 82(4):703, 1999.

[18] M. Viteau, A. Chotia, M. Allegrini, N. Bouloufa and O. Dulieu *et al.* Optical Pumping and Vibrational Cooling of Molecules. *Science*, 321(5886):232, 2008.

[19] J. D. Weinstein, R. deCarvalho, T. Guillet, B. Friedrich and J. M. Doyle. Magnetic trapping of calcium monohydride molecules at millikelvin temperatures. *Nature*, 395(6698):148, 1998.

[20] H. L. Bethlem, G. Berden and G. Meijer. Decelerating Neutral Dipolar Molecules. *Phys. Rev. Lett.*, 83(8):1558, 1999.

[21] S. A. Rangwala, T. Junglen, T. Rieger, P. W. H. Pinkse and G. Rempe. Continuous source of translationally cold dipolar molecules. *Phys. Rev. A*, 67(4):043406, 2003.

[22] H. L. Bethlem, G. Berden, F. M. H. Crompvoets, R. T. Jongma and van A. J. A. Roij *et al.* Electrostatic trapping of ammonia molecules. *Nature*, 406:491, 2000.

[23] F. M. Crompvoets, H. L. Bethlem, R. T. Jongma and G. Meijer. A prototype storage ring for neutral molecules. *Nature*, 411(6834):174, 2001.

[24] T. Rieger, T. Junglen, S. A. Rangwala, P. W. H. Pinkse and G. Rempe. Continuous Loading of an Electrostatic Trap for Polar Molecules. *Phys. Rev. Lett.*, 95(17):173002, 2005.

[25] S. Hoekstra, J. J. Gilijamse, B. Sartakov, N. Vanhaecke and L. Scharfenberg *et al.* Optical Pumping of Trapped Neutral Molecules by Blackbody Radiation. *Phys. Rev. Lett.*, 98(13):133001, 2007.

[26] R. Fulton, A. I. Bishop and P. F. Barker. Optical Stark Decelerator for Molecules. *Phys. Rev. Lett.*, 93(24):243004, 2004.

[27] K. K. Ni, S. Ospelkaus, M. H. G. de Miranda, A. Pe'er and B. Neyenhuis *et al.* A High Phase-Space-Density Gas of Polar Molecules. *Science*, 322(5899):231, 2008.

[28] S. Ospelkaus, A. Pe'er, K. K. Ni, J. J. Zirbel and B. Neyenhuis *et al.* Efficient state transfer in an ultracold dense gas of heteronuclear molecules. *Nat. Phys.*, 4(8):622, 2008.

[29] F Lang, K Winkler, C Strauss, R Grimm and Denschlag J Hecker. Ultracold Triplet Molecules in the Rovibrational Ground State. *Phys. Rev. Lett.*, 101:133005, 2008.

[30] J. G. Danzl, E. Haller, M. Gustavsson, M. J. Mark and R. Hart *et al.* Quantum Gas of Deeply Bound Ground State Molecules. *Science*, 321(5892):1062, 2008.

[31] J. Deiglmayr, A. Grochola, M. Repp, K. Mörtlbauer and C. Glück *et al.* Formation of Ultracold Polar Molecules in the Rovibrational Ground State. *Phys. Rev. Lett.*, 101(13), 2008.

[32] D. Gerlich. Ion-neutral collisions in a 22-pole trap at very low energies. *Phys. Scripta*, T59:256, 1995.

[33] S. Trippel, J. Mikosch, R. Berhane, R. Otto and M. Weidemuller *et al.* Photodetachment of Cold OH^- in a Multipole Ion Trap. *Phys. Rev. Lett.*, 97(19):193003, 2006.

[34] J. Mikosch, U. Frühling, S. Trippel, R. Otto and P. Hlavenka *et al.* Evaporation of trapped anions studied with a 22-pole ion trap in tandem time-of-flight configuration. *Phys. Rev. A*, 78(2):023402, 2008.

[35] K. Mølhave. Construction of and Experiments with a Linear Paul Trap. Masters thesis, University of Aarhus, 2000.

[36] M. Drewsen, I. Jensen, J. Lindballe, N. Nissen and R. Martinussen *et al.* Ion Coulomb crystals: A tool for studying ion processes. *Int. J. Mass Spectrom.*, 229(1-2):83, 2003.

[37] M. Drewsen, A. Mortensen, R. Martinussen, P. Staanum and J. L. Sørensen. Nondestructive Identification of Cold and Extremely Localized Single Molecular Ions. *Phys. Rev. Lett.*, 93(24):243201, 2004.

[38] P. Blythe, B. Roth, U. Fröhlich, H. Wenz and S. Schiller. Production of Ultracold Trapped Molecular Hydrogen Ions. *Phys. Rev. Lett.*, 95(18):183002, 2005.

[39] A. Ostendorf, C. B. Zhang, M. A. Wilson, D. Offenberg and B. Roth *et al.* Sympathetic Cooling of Complex Molecular Ions to Millikelvin Temperatures. *Phys. Rev. Lett.*, 97(24), 2006.

[40] K. Højbjerre, D. Offenberg, C. Z. Bisgaard, H. Stapelfeldt and P. F. Staanum *et al.* Consecutive photodissociation of a single complex molecular ion. *Phys. Rev. A*, 77(3):030702, 2008.

[41] P. F. Staanum, K. Højbjerre, R. Wester and M. Drewsen. Probing Isotope Effects in Chemical Reactions Using Single Ions. *Phys. Rev. Lett.*, 100(24):243003, 2008.

[42] S. Willitsch, M. T. Bell, A. D. Gingell, S. R. Procter and T. P. Softley. Cold Reactive Collisions between Laser-Cooled Ions and Velocity-Selected Neutral Molecules. *Phys. Rev. Lett.*, 100(4):043203, 2008.

[43] A. T. Grier, M. Cetina, F. Orucevic and V. Vuletic. Observation of Cold Collisions between Trapped Ions and Trapped Atoms. *Phys. Rev. Lett.*, 102:223201, 2009.

[44] I. S. Vogelius, L. B. Madsen and M. Drewsen. Blackbody-Radiation-Assisted Laser Cooling of Molecular Ions. *Phys. Rev. Lett.*, 89(17):173003, 2002.

[45] I. S. Vogelius, L. B. Madsen and M. Drewsen. Rotational cooling of heteronuclear molecular ions with $^1\Sigma$, $^2\Sigma$, $^3\Sigma$, and $^2\Pi$ electronic ground states. *Phys. Rev. A*, 70(5):053412, 2004.

[46] I. S. Vogelius, L. B. Madsen and M. Drewsen. Probabilistic state preparation of a single molecular ion by projection measurement. *J. Phys. B - At. Mol. Opt.*, 39:1259, 2006.

[47] S. L. Anderson. Multiphoton ionization state selection: Vibrational-mode and rotational-state control. *Adv. Chem. Phys.*, 177:12, 1992.

[48] J. D. Prestage, G. J. Dick and L. Maleki. New ion trap for frequency standard applications. *J. Appl. Phys.*, 66(3):1013, 1989.

[49] M. G. Raizen, J. M. Gilligan, J. C. Bergquist, W. M. Itano and D. J. Wineland. Ionic crystals in a linear Paul trap. *Phys. Rev. A*, 45(9):6493, 1992.

[50] M. Drewsen and A. Brøner. Harmonic linear Paul trap: Stability diagram and effective potentials. *Phys. Rev. A*, 62(4):45401, 2000.

[51] P. K. Ghosh. *Ion traps.*, Oxford : Clarendon Press, 1995. edition, 1995.

[52] L. Hornekær. *Single- and Multi-Species Coulomb Ion Crystals: Structures, Dynamics and Sympathetic Cooling*. PhD thesis, 2000.

[53] M. Abramowitz and I. A. Stegun. *Handbook of Mathematical Functions with Formulas, Graphs, and Mathematical Tables*. Dover, New York, ninth Dover printing, tenth GPO printing edition, 1964.

[54] R. F. Wuerker, H. Shelton and R. V. Langmuir. Electrodynamic containment of charged particles. *J. Appl. Phys.*, 30:342, 1959.

[55] D. R. Denison. Operating Parameters of a Quadrupole in a Grounded Cylindrical Housing. *J. Vac. Sci. Technol.*, 8(1):266, 1971.

[56] N. Kjærgaard, L. Hornekær, A. M. Thommesen, Z. Videsen and M. Drewsen. Isotope selective loading of an ion trap using resonance-enhanced two-photon ionization. *Appl. Phys. B*, 71(2):207, 2000.

[57] A. Mortensen, JJT Lindballe, IS Jensen, P. Staanum and D. Voigt *et al.* Isotope shifts of the $4s^2\,{}^1S_0 \rightarrow 4s5p^1P_1$ transition and hyperfine splitting of the $4s5p^1P_1$ state in calcium. *Phys. Rev. A*, 69(4):042502, 2004.

[58] J. E. Hansen, C. Laughlin, H. W. van der Hart and G. Verbockhaven. Energy levels, wavefunction compositions, and electric dipole transitions in neutral Ca. *J. Phys. B*, 32:2099, 1999.

[59] G. Smith. Oscillator strengths for neutral calcium lines of 2. 9 eV excitation. *J. Phys. B*, 21:2827, 1988.

[60] N. Beverini, E. Maccioni, F. Sorrentino, V. Baraulia and M. Coca. Measurement of the $4s^2\,{}^1S_0 \rightarrow 4s3d\,{}^1D_2$ transition probability in calcium. *Eur. Phys. J. D*, 23(2):223, 2003.

[61] P. Herskind, J. Lindballe, C. Clausen, J.L. Sørensen and M. Drewsen. Second-harmonic generation of light at 544 and 272 nm from an ytterbium-doped distributed-feedback fiber laser. *Opt. Lett.*, 32(3):268, 2007.

[62] P. Herskind. *Cavity Quantum Electrodynamics with Ion Coulomb Crystals*. PhD thesis, 2008.

[63] T. W. Hansch and B. Couillaud. Laser frequency stabilization by polarization spectroscopy of a reflecting reference cavity. *Opt. Commun.*, 35(3):441, 1980.

[64] J. J. T. Lindballe. Eksperimenter med resonant to-foton isotop-selektiv fotoionisation af calcium ved anvendelse af en frekvensfordoblet farvestoflaser. *Speciale*, 2003.

[65] D. N. Madsen, S. Balslev, M. Drewsen, N. Kjærgaard and Z. Videsen *et al.* Measurements on photo-ionization of $3s3p\,^1P_1$ magnesium atoms. *J. Phys. B - At. Mol. Opt.*, 33:4981, 2000.

[66] H.J. Metcalf and P. Van der Straten. *Laser Cooling and Trapping*. Springer-Verlag, New York, 1999.

[67] E. D. Black. An introduction to Pound–Drever–Hall laser frequency stabilization. *Am. J. Phys.*, 69(1):79, 2001.

[68] N. Kjærgaard. *Methods in Laser Cooling of Ions in Storage Rings and Traps*. PhD thesis, 2001.

[69] K. Mølhave and M. Drewsen. Formation of translationally cold MgH^+/MgD^+ molecules in an ion trap. *Phys. Rev. A*, 62:011401(R), 2000.

[70] B. Roth, P. Blythe, H. Wenz, H. Daerr and S. Schiller. Ion-neutral chemical reactions between ultracold localized ions and neutral molecules with single-particle resolution. *Phys. Rev. A*, 73(4):042712, 2006.

[71] D. J. Larson, J. C. Bergquist, J. J. Bollinger, W. M. Itano and D. J. Wineland. Sympathetic cooling of trapped ions: A laser-cooled two-species nonneutral ion plasma. *Phys. Rev. Lett.*, 57(1):70, 1986.

[72] A. J. Dempster. A new method of positive ray analysis. *Phys. Rev.*, 11(4):316, 1918.

[73] R. E. March and J. F. J. Todd. *Practical Aspects of Ion Trap Mass Spectrometry I–III*. CRC Press, Boca Raton, 1995.

[74] E. W. Blauth. *Dynamic Mass Spectrometry*. Elsevier, 1966.

[75] R. E. March. Quadrupole ion trap mass spectrometry: A view at the turn of the century. *Int. J. Mass Spectrom.*, 200:285, 2000.

[76] H. Wollnik. Time-of-flight mass analyzers. *Mass Spectrom. Rev.*, 12:89, 1993.

[77] M. B. Comisarow and A. G. Marshall. Fourier transform ion cyclotron resonance spectroscopy. *Chem. Phys. Lett.*, 25:282, 1974.

[78] S. Rainville, J. K. Thompson and D. E. Pritchard. An ion balance for ultra-high-precision atomic mass measurements. *Science*, 303(5656):334, 2004.

[79] D. F. V. James. Quantum dynamics of cold trapped ions with application to quantum computation. *Appl. Phys. B*, 66(2):181, 1998.

[80] G. Morigi and H. Walther. Two-species Coulomb chains for quantum information. *The European Physical Journal D-Atomic, Molecular and Optical Physics*, 13(2):261, 2001.

[81] D. Stick, W. K. Hensinger, S. Olmschenk, M. J. Madsen and K. Schwab *et al.* Ion trap in a semiconductor chip. *Nat. Phys.*, 2(1):36, 2006.

[82] H. F. Powell, D. M. Segal and R. C. Thompson. Axialization of laser cooled magnesium ions in a Penning trap. *Phys. Rev. Lett.*, 89(9):93003, 2002.

[83] P. Staanum, I. S. Jensen, R. G. Martinussen, D. Voigt and M. Drewsen. Lifetime measurement of the metastable $3d\,^2D_{5/2}$ state in the $^{40}Ca^+$ ion using the shelving technique in a few-ion string.. *Phys. Rev. A.*, 69:032503, 2004.

[84] P. Staanum. *Quantum Optics with Trapped Calcium Ions*. PhD thesis, University of Aarhus, Denmark, 2004.

[85] M. C. Cross, A. Zumdieck, R. Lifshitz and J. L. Rogers. Synchronization by nonlinear frequency pulling. *Phys. Rev. Lett.*, 93:224101, 2004.

[86] S. Evoy, D. W. Carr, L. Sekaric, A. Olkhovets and J. M. Parpia *et al.* Nanofabrication and electrostatic operation of single-crystal silicon paddle oscillators. *J. Appl. Phys.*, 86:6072, 1999.

[87] G. Audi and A. H. Wapstra. The 1993 atomic mass evaluation (I) atomic mass table. *Nucl. Phys. A*, 565(1):1, 1993.

[88] N. Schlosser, G. Reymond, I. Protsenko and P. Grangier. Sub-poissonian loading of single atoms in a microscopic dipole trap. *Nature*, 411(6841):1024, 2001.

[89] N. W. Ashcroft and N. D. Mermin. *Solid Sate Physics*. Saunders College, Philadelphia, 1976.

[90] H. Rohde, S. T. Gulde, C. F. Roos, P. A. Barton and D. Leibfried *et al.* Sympathetic ground-state cooling and coherent manipulation with two-ion crystals. *J. Opt. B*, 3(1):34, 2001.

[91] S. Gulde, D. Rotter, P. Barton, F. Schmidt-Kaler and R. Blatt *et al.* Simple and efficient photo-ionization loading of ions for precision ion-trapping experiments. *Appl. Phys. B*, 73(8):861, 2001.

[92] G. R. Guthöhrlein, M. Keller, K. Hayasaka, W. Lange and H. Walther. A single ion as a nanoscopic probe of an optical field. *Nature*, 414(6859):49, 2001.

[93] M. Drewsen. Cooling, identification and spectroscopy of super-heavy element ions. *Eur. Phys. J. D*, 45(1):125, 2007.

[94] M. Schädel. Superheavy element chemistry at GSI–status and perspectives. *Eur. Phys. J. D*, 45(1):67, 2007.

[95] H. Haba, T. Akiyama, D. Kaji, H. Kikunaga and T. Kuribayashi *et al.* Startup of superheavy element chemistry at RIKEN. *Eur. Phys. J. D*, 45(1):81, 2007.

[96] M. Drewsen, L. Hornekær, N. Kjærgaard, K. Molhave and A. M. Tommesenet al.. Ion coulumb crystals and some applications. In *AIP Conference Proceedings*, pages 135-144, 2002. Non-Neutral Plasma Physics Conference IV.

[97] Y. L. Yung and W B. DeMore. *Photochemistry of Planetary Atmospheres*. Oxford University Press, 1998.

[98] T. W. Hartquist and D. A. Williams. *The Chemically Controlled Cosmos*. Cambridge University Press, 1995.

[99] R. Schinke. *Photodissociation dynamics*. Cambridge University Press, 1993.

[100] A. A. Turnipseed, G. L. Vaghjiani, J. E. Thompson and A. R. Ravishankara. Photodissociation of HNO_3 at 193, 222, and 248 nm - Products and quantum yields. *J. Chem. Phys.*, 96:5887, 1992.

[101] A. Furlan, H. A. Scheld and J. Robert Huber. Production of OCCN radicals by photodissociation of carbonyl cyanide $CO(CN)_2$ at 193 nm. *Chem. Phys. Lett.*, 282:1, 1998.

[102] A. G. Suits and J. W. Hepburn. Ion pair dissociation: Spectroscopy and dynamics. *Ann. Rev. Phys. Chem.*, 57:431, 2006.

[103] Y. Hirosaka and J. H. D. Eland. New results on photoion pair formation from application of the velocity imaging photoionisation coincidence technique. *Rapid Commun. Mass Spectrom.*, 14:2305, 2000.

[104] A. G. Marshall, C. L. Hendrickson and G. S. Jackson. Fourier transform ion cyclotron resonance mass spectrometry: A primer. *Mass Spectrom. Rev.*, 17:1, 1998.

[105] J. Lemaire, P. Boissel, M. Heninger, G. Mauclaire and G. Bellec *et al.* Gas Phase Infrared Spectroscopy of Selectively Prepared Ions. *Phys. Rev. Lett.*, 89(27):273002, 2002.

[106] K. Kato and K. Yamanouchi. Photodecomposition reaction of trapped aniline cation by photofragment excitation spectroscopy. *Chem. Phys. Lett.*, 397:237, 2004.

[107] M. A. Smith, J. W. Hager and S. C. Wallace. Two color photoionization spectroscopy of jet cooled aniline: Vibrational frequencies of the aniline $\tilde{X}\ ^2B_1$ radical cation. *J. Chem. Phys.*, 80:3097, 1984.

[108] A. Marshall, A. Clark, R. Jennings, K. W. D. Ledingham and R. P. Singhal. Resonant two-photon ionization for detection of aromatic molecules. *Meas. Sci. Technol.*, 2(11):1078, 1991.

[109] O. K. Yoon, W. G. Hwang, J. C. Choe and M. S. Kim. Internal energy content of *n*-butylbenzene, bromobenzene, iodobenzene and aniline molecular ions generated by two-photon ionization at 266 nm. A photodissociation study. *Rapid Commun. Mass Spectrom.*, 13(14):1515, 1999.

[110] M. L. Quiniou, A. J. Yates and P. R. Langridge-Smith. Laser photo-induced dissociation using tandem time-of-flight mass spectrometry. *Rapid Commun. Mass Spectrom.*, 14(5):361, 2000.

[111] H. Kühlewind, H. J. Neusser and E. W. Schlag. Multiphoton metastable ion spectra and ion dissociation kinetics: Analysis of the decay channels of the aniline cation with a reflectron time-of-flight instrument. *J. Chem. Phys.*, 82(12):5452, 1985.

[112] C. Z. Bisgaard. *Laser induced alignment: Towards fixed-in-space molecules*. PhD thesis, University of Aarhus, 2006.

[113] J. R. Eyler, J. Oddershede, J. R. Sabin, G. H. F. Diercksen and N. E. Gruener. Excitation energy of linear propargylium ($C_3H_3^+$). Can this ion be detected by laser-induced fluorescence in flames?. *J. Phys. Chem.*, 88(14):3121, 1984.

[114] F. Ozturk, G. Baykut, M. Moini and J. R. Eyler. Reactions of the propynylium isomer manifold with acetylene and diacetylene in the gas phase. *J. Phys. Chem.*, 91(16):4360, 1987.

[115] I. Savic and D. Gerlich. Temperature variable ion trap studies of $C_3H_n^+$ with H_2 and HD. *Phys. Chem. Chem. Phys.*, 7:1026, 2005.

[116] I. Savić, S. Schlemmer and D. Gerlich. Low-Temperature Experiments on the Formation of Deuterated $C_3H_3^+$. *Astrophys. J.*, 621:1163, 2005.

[117] H. F. Calcote and D. G. Keil. The role of ions in soot formation. *Pure Appl. Chem*, 62:815, 1990.

[118] R. J. Hendricks, J. L. Sørensen, C. Champenois, M. Knoop and M. Drewsen. Doppler cooling of calcium ions using a dipole-forbidden transition. *Phys. Rev. A*, 77:021401(R), 2008.

[119] T. J. Millar. Deuterium fractionation in interstellar clouds. *Space Sci. Rev*, 106(1):73, 2003.

[120] P. H. Corneil and G. C. Pimentel. Hydrogen–Chlorine Explosion Laser. II. DCl. *J. Chem. Phys.*, 49:1379, 1968.

[121] M. J. Berry. F + H_2, D_2, HD reactions: Chemical laser determination of the product vibrational state populations and the F + HD intramolecular kinetic isotope effect. *J. Chem. Phys.*, 59:6229, 1973.

[122] W. Hu and G. C. Schatz. Theories of reactive scattering. *J. Chem. Phys.*, 125:132301, 2006.

[123] D. M. Neumark, A. M. Wodtke, G. N. Robinson, C. C. Hayden and Y. T. Lee. Experimental Investigation of Resonances in Reactive Scattering: The F + H_2 Reaction. *Phys. Rev. Lett.*, 53(3):226, 1984.

[124] M. Qiu, Z. Ren, L. Che, D. Dai and S. A. Harich *et al.* Observation of feshbach resonances in the F + H_2 → HF + H reaction. *Science*, 311(5766):1440, 2006.

[125] N. F. Dalleska, K. C. Crellin and P. B. Armentrout. Reactions of alkaline earth ions with hydrogen, deuterium, and hydrogen deuteride. *J. Phys. Chem.*, 97(13):3123, 1993.

[126] R. Georgiadis and P. B. Armentrout. Translational and electronic energy dependence of chromium ion reactions with methane. *J. Phys. Chem.*, 92(25):7067, 1988.

[127] R. D. Levine. *Molecular reaction dynamics*. Cambridge University Press, 2005.

[128] W. Kołos and L. Wolniewicz. Polarizability of the hydrogen molecule. *J. Chem. Phys.*, 46:1426, 1967.

[129] G. Herzberg. *Molecular Spectra and Molecular Structure - Vol I*. Krieger Publishing Company, Malabar, Florida, 1989.

[130] P. D. Kleiber and J. Chen. Spectroscopy and chemical dynamics of weakly bound alkaline-earth metal ion-H and alkaline-earth metal ion-hydrocarbon complexes 2. *Int. Rev. Phys. Chem.*, 17(1):1, 1998.

[131] C. W. Bauschlicher. The ground and low-lying excited states of MgH_2^+. *Chem. Phys. Lett.*, 201:11, 1993.

[132] L. N. Ding, M. A. Young, P. D. Kleiber, W. C. Stwalley and A. M. Lyyra. Photofragmentation spectroscopy of MgD_2^+. *J. Phys. Chem.*, 97(10):2181, 1993.

[133] W. H. Breckenridge and J. H. Wang. Dynamics of the reactions of Mg ($3s3p\,^1P_1$) with H_2, HD and D_2: rotational quantum state distributions of MgH(MgD) products. *Chem. Phys. Lett.*, 137(3), 1987.

[134] W. H. Breckenridge and H. Umemoto. Nascent internal energy distributions of MgH (MgD) produced in the reaction of Mg ($3s3p\,^1P_1$) with $H_2(D_2)$. *J. Chem. Phys.*, 80:4168, 1984.

[135] S. Bililign and P. D. Kleiber. Nascent rotational quantum state distribution of NaH (NaD) from the reaction of $Na^*(4\,^2P)$ with H_2, D_2, and HD. *J. Chem. Phys.*, 96:213, 1992.

[136] D. Gerlich, E. Herbst and E. Roueff. $H_3^+ + HD \rightarrow H_2D^+ + H_2$: Low-temperature laboratory measurements and interstellar implications. *Planet. Space Sci.*, 50:1275, 2002.

[137] A. Bertelsen, S. Jørgensen and M. Drewsen. The rotational temperature of polar molecular ions in Coulomb crystals. *J. Phys. B - At. Mol. Opt.*, 39:L83, 2006.

[138] M. Tacconi and F. A. Gianturco. Molecular ions in ultracold atomic gases: Computed electronic interactions for $MgH^+(X^1\Sigma^+)$ with Rb. *Eur. Phys. J. D*, 46(3):443, 2008.

[139] B. Roth, D. Offenberg, C. B. Zhang and S. Schiller. Chemical reactions between cold trapped Ba^+ ions and neutral molecules in the gas phase. *Phys. Rev. A*, 78(4):042709, 2008.

[140] M. J. Frisch, G. W. Trucks, H. B. Schlegel, P. M. W. Gill and B. G. Johnson *et al.* Gaussian 95. *Gaussian Inc., Pittsburgh*, 1995.

[141] R. J. Le Roy. LEVEL 7.5: A computer program for solving the radial Schrödinger equation for bound and quasibound levels. *University of Waterloo Chemical Physics Research Rep. CP-655 (University of Waterloo, Waterloo, Ontario, Canada, 2002)..*

[142] W. J. Balfour. Rotational analysis of the $A^1\Sigma^+ \rightarrow X^1\Sigma^+$ and $B^1\Pi \rightarrow X^1\Sigma^+$ systems of $^{24}MgH^+$, $^{25}MgH^+$, and $^{26}MgH^+$. *Can. J. Phys.*, 50, 1972.

[143] F. Tittel, D. Richter and A. Fried. Mid-Infrared Laser Applications in Spectroscopy. In *Solid-State Mid-Infrared Laser Sources*, number 89 in Topics in Applied Physics, pages 458–529. , 2003.

[144] Hitran database. http://www.cfa.harvard.edu/hitran.

[145] S. Jørgensen, A. Bertelsen and M. Drewsen. 2006. Unpublished.

[146] Effect of optical pumping in two-step photoionization of Na_2 in molecular beams. *Chem. Phys. Lett.*, 78:515, 1981.

[147] L. Hornekær, N. Kjærgaard, A. M. Thommesen and M. Drewsen. Structural Properties of Two-Component Coulomb Crystals in Linear Paul Traps. *Phys. Rev. Lett.*, 86:1994, 2001.

[148] L. Hornekær and M. Drewsen. Formation process of large ion Coulomb crystals in linear Paul traps. *Phys. Rev. A*, 66(1):013412, 2002.

[149] A. Bertelsen. The rotational temperature of translational sympathetically cooled $^{24}MgH^+$ investigated by photodissociation. , 2005.

[150] P. W. Milonni and J. H. Eberly. *Lasers*. Wiley, 1988.

[151] K. Bergmann and B. W. Shore. *Molecular dynamics and spectroscopy by stimulated emission pumping*, chapter 9, Coherent Population Transfer. World Scientific, 1995.

[152] R. N. Zare. *Angular momentum: understanding spatial aspects in chemistry and physics*. John Wiley, New York, 1988.

[153] A. Hansson and J.K.G. Watson. A comment on Hönl-London factors. *J. Mol. Spec.*, 233(2):169, 2005.

[154] I. S. Vogelius, L. B. Madsen and M. Drewsen. Rotational cooling of molecules using lamps. *J. Phys. B - At. Mol. Opt.*, 37(22):4571, 2004.

[155] S. B. Kristensen. Rotationel laserkøling af MgH^+ molekylet. *Bachelor thesis*, 2009.

[156] K. J. R. Rosman and P. D. P. Taylor. Isotopic Compositions of Elements 1997. *J. Phys. Chem. Ref. Data*, 27:1275, 1998.

[157] NIST Atomic Spectra Database. http://www.nist.gov.

[158] R. N. Gosselin, E. H. Pinnington and W. Ansbacher. Measurement of the lifetimes of the 4*p* levels in Ca II using laser excitation of a fast beam. *Physical Review A*, 38(9):4887, 1988.

[159] L. Liljeby, A. Lindgard, S. Mannervik, E. Veje and B. Jelenkovic. Lifetimes in MgI and MgII; Beam-Foil measurements and Numerical Coulomb Approximation wavefunctions. *Phys. Scr*, 21:805, 1980.

[160] L. Hallstadius. Extended measurements of isotope shifts in Mg I. *Zeitschrift für Physik A*, 291(3):203, 1979.

[161] W. Ansbacher, Y. Li and E. H. Pinnington. Precision lifetime measurement for the 3*p* levels of MgII using frequency-doubled laser radiation to excite a fast ion beam. *Phys. Lett. A*, 139(3-4), 1989.